



KIT SCIENTIFIC REPORTS 7661

The quantification of the key physics parameters for the DEMO fusion power reactor and analysis of the reactor relevant physics issues

Yu. Igitkhanov, B. Bazylev, R. Fetzer

Yu. Igitkhanov, B. Bazylev, R. Fetzer

The quantification of the key physics parameters for the DEMO fusion power reactor and analysis of the reactor relevant physics issues

Karlsruhe Institute of Technology
KIT SCIENTIFIC REPORTS 7661

The quantification of the key physics parameters for the DEMO fusion power reactor and analysis of the reactor relevant physics issues

by

Yu. Igitkhanov, B. Bazylev, R. Fetzer

Impressum



Karlsruher Institut für Technologie (KIT)
KIT Scientific Publishing
Straße am Forum 2
D-76131 Karlsruhe

KIT Scientific Publishing is a registered trademark of Karlsruhe
Institute of Technology. Reprint using the book cover is not allowed.

www.ksp.kit.edu



*This document – excluding the cover – is licensed under the
Creative Commons Attribution-Share Alike 3.0 DE License*

(CC BY-SA 3.0 DE): <http://creativecommons.org/licenses/by-sa/3.0/de/>



*The cover page is licensed under the Creative Commons
Attribution-No Derivatives 3.0 DE License (CC BY-ND 3.0 DE):*

<http://creativecommons.org/licenses/by-nd/3.0/de/>

Print on Demand 2014

ISSN 1869-9669

DOI: 10.5445/KSP/1000038935

Objectives and short summary

Our activity was mainly devoted to the preparation of physics issues, needed for DEMO design. Since the design of the reactor FW blanket for DEMO is still under discussion, we have considered in our calculations the most promising designs of the FW and divertor PF components made from different materials. Thermal analyses have been provided to justify the applicability of these models. The characteristics of repetitive Type I ELMs in DEMO derived based on scaling arguments, predictions for ITER and data from experiments. Our calculation show:

Thermal energy release during ELMs is assessed as 80-100MJ, the ELM frequency of 1-0.8Hz and the deposition time about 1.2ms. For existing DEMO designs this corresponds about 15-20MJ/m² of deposition energy to the inboard divertor (spatially average value).

Thermo-hydraulic analyses of W/EUROFER castellated sandwich type module for divertor and the FW and the entirely made from W divertor module shows that:

In the case of uncontrolled ELMs (80-100MJ energy impact and the ELM frequency of 1-0.8Hz) the W divertor plate melts and evaporates. The vapor pressure gradient causes intensive motion of tungsten molten layer with the velocity of 0.5 m/s and the surface roughness of 0.1 μm per ELM. However, the melt splashing does not develop at that velocity and, therefore, all metallic mass losses are mainly due to target evaporation.

The separatrix strike point random “motion” on the tungsten divertor plate during the repetitive uncontrolled ELMs does not prevent from melting but the total surface erosion becomes essentially smaller.

Power load of uncontrolled ELMs on the FW W armor is tolerable. The tungsten armor temperature of the sandwich type FW module during the operation saturates at the value much less than the melting point (~950K).

The controlled ELMs with ~33 times reduced amplitude (as it is in ITER) are still causing the W surface melting in a sandwich type of divertor module with water cooling due to low heat removal capability. However, the monoblock W divertor module tolerates heat loads of controlled ELMs even for large steady state heat load of 8.9MW/m² envisaged for advanced DEMO version.

Thermo-hydraulic analyses of Cu OHFC/EUROFER bound module under expected in DEMO conditions show the following.

During the steady state operation without ELMs the maximum temperatures of the FW and divertor modules stay below upper allowable limits for all materials. The W surface does not melt and the cracking at heat loads ≤ 5MW/m² seems to be unexpected. Unfortunately, the operating temperatures of the FW materials are below the allowable low limits and, for example, a severe embrittlement of W and EUROFER under neutron irradiation can be expected. This situation can be approved by operating at lower cooling efficiency.

For the FW, the unmitigated ELMs are tolerable for both DEMOI and DEMOII design operations. In the divertor, the maximum allowable W temperature between the ELMs is within the limits, but at the ELM peaks it considerably exceeds the melting temperature. Therefore, the W surface melts and evaporates during the ELM peaks and between the ELMs W recrystallization occurs. The maximum EUROFER and Cu alloy temperatures remain within the operation limits. However, the minimum EUROFER (tube) temperature remains below the low limit and could in time experience embrittlement failure. Evaporation of W and vapor shielding keeps the material temperatures saturated during the repetitive ELMs impact. The water cooling remains within the PWR range.

Mitigation of ELMs results in reduced W peak temperatures and melting does not occur even in the divertor of DEMO II operation. However, because of the absence of evaporation, the vapor screening effect does not occur. Therefore, the power flux to the module effectively is increased, although the amplitude of individual ELMs is reduced. As a consequence, the temperatures of all materials are above the allowable ranges. To improve the situation, a more efficient cooling is required, which cannot be achieved within the PWR cooling conditions.

In the case of 6 mm inner pipe diameter and the PWR conditions the EUROFER temperature remains within the allowable limits. For the FW under these conditions overcooling of the module occurs, whereas for the divertor in the case of mitigated ELMs heat flux to the water reaches the critical value of 24 MW/m² corresponding to supercritical water.

Thermo-hydraulic analyses W mono-block module with DCC/ EUROFER water pipe in DEMO steady state operation with the ELMs power loads is analyzed. Calculations show that

For the PFC W module with reinforced DCC/EUROFER tube, steady state DEMO I and advanced DEMO II operation without ELMs results in maximum temperatures of the FW and divertor modules below the upper allowable limits for all materials with layer thicknesses $\Delta_W=3.0$ mm, $\Delta_{DCC}=1.0$ mm, and $\Delta_{EUROFER}=0.4$ mm.

For DEMO operation with unmitigated ELMs, for the divertor modules, the maximum allowable W temperature between the ELMs is within the allowable limits, but at the ELM peaks considerably exceeds the melting temperature. Therefore, the W surface melts and evaporates during the ELM peaks and between the ELMs W recrystallization occurs. Nevertheless, the maximum of EUROFER, DCC and Cu alloy temperatures remain within the operation limits.

In the case of unmitigated ELMs, evaporation of W and consequent vapor shielding keeps the heat flux to the PFC materials and coolant tube limited. This heat flux reduction does not occur in the case of mitigated ELMs. Due to the reduced ELM amplitude, no melting and no evaporation occur. This beneficial effect of mitigation, however, is accompanied by a large heat flux at the coolant tube, which for DEMO II divertor operation exceeds the critical heat flux for PWR cooling range.

The lithium surfaces divertor concept has been investigated. We calculate the impact of Type I ELM heat loads expected in ITER or in DEMO on erosion of Li divertor target. It was shown, that under reactor conditions erosion, splashing and stability of liquid flow remains an issue and requires further investigation.

Content

Objectives and short summary	i
Content	v
List of abbreviations.....	viii
Synopsis	9
1 Modelling of DEMO PFC Erosion due to ELM impact	1
1.2 Introduction	1
1.3 Specification of Type I ELMs in DEMO	2
1.4 The model for melt-motion simulation.....	5
1.5 Erosion due to unmitigated ELMs	8
1.6 Unmitigated ELMs load on the DEMO FW	10
1.7 Effect of mitigated ELMs on DEMO divertor.....	12
1.8 Conclusions	14
Acknowledgments.....	14
1.9 References	15
2 Design Strategy for the PFC in DEMO Reactor	17
2.1 Introduction	17
2.2 Power loading on the FW and divertor	19
2.3 Steady state operation without ELMs.....	20
2.4 Effect of unmitigated ELMs.....	21
2.5 Effect of controlled ELMs	24
2.6 Conclusions	27
Acknowledgments.....	28
2.7 References	28
3 Effect of Thermal Loads on Different Modules of DEMO PFC.....	29
3.1 Introduction	29
3.2 Power loading on the FW and divertor	30
3.3 W monoblock module with CuOFHC / EUROFER water coolant tube	31
3.4 W monoblock module with DCC/EUROFER water coolant tube.....	32
3.5 Conclusion.....	32
Acknowledgment	33
3.6 References	34
Figure Caption	35
4 Conversion of magnetic energy of runaway electrons during disruption termination.....	41
4.1 Introduction	41
4.2 Kinetic and magnetic energy stored in the RE	42
4.3 Heat load onto the first wall due to the RE impact.....	43
4.4 Collisional stopping power and the density effect correction	44
4.5 The results of ENDEP calculations for RE in ITER	46
4.6 Conclusions	47

	Acknowledgments.....	48
4.7	References.....	48
5	Towards a physics-integrated view of the inner fusion fuel cycle.....	49
5.1	Introduction.....	49
5.2	Fuel cycle sub-systems	50
5.3	Contributions to machine throughput	51
5.4	Physics-integrated approach for the torus exhaust vacuum pumps.....	54
5.5	Physics-integrated approach for the pellet injectors	58
5.6	Conclusion	58
	Acknowledgments.....	59
5.7	References.....	59
6	Extend physics assessment of novel divertor configuration	61
6.1	Effect of flux expansion, connection length on stability of radiation.....	61
6.2	Coupling of ballooning instability with thermal instability.....	64
6.3	Conclusion	67
	Acknowledgements	68
6.4	References	68
7	Plasma Boundary Modelling: Model of the SOL and Divertor transport.....	69
7.1	Introduction.....	69
7.2	2D fluid equations for SOL and divertor plasma in TOKES	69
7.3	Boundary conditions	72
7.4	Kinetic effects in the SOL plasma	74
7.5	Model for H-Mode Pedestal formation.....	77
7.6	Conclusions.....	78
	Acknowledgements	79
7.7	Reference	79
8	Modeling of Li layer behavior under ITER like ELM loads.....	81
8.1	Introduction.....	81
8.2	Modelling of Li layer behaviour under ITER like ELM loads	82
8.3	Results of MEMOS calculation of Li melting under DEMO like ELM impact	85
8.4	Conclusions.....	88
8.5	References.....	89
	Appendix I	91
I.1	Introduction.....	91
I.2	Balance equations	92
I.3	A 2-Point Model for simulation of attach to detach (A/D) transition	98
	Appendix II	101
	A MARFE-type thermal instability on closed magnetic field lines	101
II.1	Introduction.....	101
II.2	Equations and topology for the standard divertor configuration	102
II.3	Topology of the 2nd order null point configuration in the SF divertor	106
II.4	Conclusions.....	107

II.5	References	108
Appendix III	113
Sputtering erosion of PFC in a long pulse DEMO operation.....		113
III.1	Introduction	113
III.2	Non-Maxwellian distribution function of incident ions	113
III.3	Conclusion.....	117
III.4	References	118
Appendix IV	119
Damage factor and characteristics of reactor materials		119
IV.1	Damage factor.....	119
IV.2	The operating temperature windows for fusion reactor materials (not radiated by neutrons).....	121
IV.3	Range of the allowable temperatures.....	122
IV.4	Properties of un-irradiated TUNGSTEN.....	122
IV.5	Properties of irradiated TUNGSTEN	122
IV.6	Characteristics of materials: W & diamond/copper composite DCC	123
IV.7	Tungsten specific heat $C_p(T)$: J/kg K.....	124
IV.8	Tungsten diffusivity $D_w(T)$:	125
IV.9	Thermal diffusivity time (sec) vs. temperature (K) for different W thickness (cm)	125
IV.10	Oxygen-free high thermal conductivity (OFHC) copper CuOFHC/Cu-c1/C10200	126
IV.11	Thermal conductivity of Cu OFHC , W/(m·°C)	127
IV.12	Reinforced Diamond/Copper Composite (DCC).....	127
IV.13	Thermal properties of diamond/copper composite material DCC	127
IV.14	Water coolant parameters.....	128
IV.15	Parameters of discharges in different tokamaks	129

List of abbreviations

SF	Snow flake magnetic configuration in the vicinity to x-point
MARFE	Multifaceted asymmetric radiation from the edges (thermal-radiative instability)
DEMO	Demonstration Power Plant project;
PFC	Plasma facing component;
SOL	Scrape-off layer,
FLF	Flux Limit Factor accounting for the kinetic effects
TOKES	Integrated code, describing the steady state and transient processes in tokamak
L / H-mode	Low (L) and High (H) confinement modes of operations in tokamak
ITER	International Thermonuclear Tokamak Reactor
JET	The Joint European Torus
MEMOS	Monte Carlo code for calculation of power loads on PFC and erosion

Synopsis

Objectives and status quo of fusion reactor power exhaust problem.

One of the challenging issues of the DEMO project is the exhaust of power and particles. At present remains unclear how to identify the gaps that exist in the physics understanding and technological solutions of the power exhaust problem and in the development of reliable heat exhaust scenarios for ITER, JT60-SA and DEMO. The primary work should be address to conventional as well as to 'advanced' divertor solutions and materials. In addition, it remains unclear how to identify the capabilities of existing devices to tackle the problems and their capabilities to reduce the identified gaps.

In general, the exhaust problem concerns the removal of heat and particles from magnetically confined fusion plasmas. The first wall neutron loads in DEMO reactor will be of the order of 1 MW/m^2 , but this power is mainly dissipated in the bulk of the first wall. Instead, the power leaving the plasma in charged particles, charge-exchange (CX) flux and electromagnetic radiation will deposit in the first few nm of the armour material. The flux in charged particles will reach the divertor target in a very localized area and even for (partially) detached plasmas, the power flux in photons, charge exchange and other neutrals will be substantial. The maximum allowable heat flux to the target is determined by technology, combining the requirements of stationary heat removal and acceptable erosion and tolerance to slow and fast variations.

In DEMO, the fusion power will be about 4-5 times of that in ITER while its linear dimension will be bigger by only about 50 %, substantially increasing the severity of the problem. Assuming that the divertor constraints are similar to ITER, the allowable power flux across the separatrix will be comparable and hence a large part of the power (60-70%) will have to be radiated from the core plasma, in addition to radiation from the plasma edge as foreseen for ITER. This will require specific use of seed impurities from the core. On the technology side, given the high neutron fluency with concomitant He production, leading to a deterioration of the thermo-mechanical properties, the technology of the divertor target will have to be modified and the tolerable heat flux may be even lower. In addition, the near-target divertor plasma temperature must not exceed a value of $\sim 5 \text{ eV}$ such that the target erosion by sputtering becomes compatible with the envisaged life time of the target components in DEMO or a reactor. The constraints on plasma control described for ITER will become more severe for DEMO, where diagnostic access will be restricted. Finally, for the reactor, additional constrains on the divertor design will come from the optimization of the balance of plant (minimizing divertor volume to maximize space available for tritium breeding for instance).

The heat loads on the first wall due to power in charged particles and by CX neutrals are generally smaller than in the divertor, but for highly radiative scenarios, the load due to electromagnetic radiation has to be taken into account as well. This is important since the technology used there will be different from that in the divertor and has to be chosen to be compatible with the heat and particle loads. In addition, for DEMO and a reactor, first wall technology must be compatible with requirements for efficient T breeding (e.g. thin plasma facing armour). The exceptions are limiters if these are needed in

the main chamber for the plasma start-up and off normal events since they may receive high power loads. However, it is assumed that ITER will close the gap w.r.t. limiter design.

Concerning the removal of particles, adequate neutral pressure for pumping both the working gas as well as the He ash and other gaseous impurities has to be provided, at the same time keeping the pressure in the main chamber low enough such to not degrade plasma operation seriously. Also, the entrainment of sputtered first wall material in the divertor has to be optimised. Given above challenges can be structured as follows:

The conventional poloidal divertor in lower quadruple single null using a solid target relatively close to the plasma is the solution to be applied in ITER and JT-60SA, but it is at present not clear if its potential is sufficient to also serve as solution for the exhaust problem in DEMO. Hence, an analysis of the status of the conventional poloidal divertor must be given, concerning both physics and technology. This leads to the identification of gaps from which a strategy to close these gaps can be derived. The aim of this programme will be to support the ITER and JT-60SA solution and at the same time, to explore the ultimate limit of the conventional divertor for application in DEMO.

As risk mitigation strategy, 'advanced' solutions are analysed. In physics, it means alternative divertor geometries that promise to increase substantially the wetted area beyond the conventional divertor value and potentially provide larger divertor volume, easing additional radiation and divertor detachment. In particular, the 'snowflake' geometry is examined. We analyse potential showstoppers and existing gaps that have to be filled to assess if these solutions present superior alternatives to the conventional solution.

The main requirements for the DEMO divertor are currently based on four different material classes that could be used which are already available today: copper (pure or precipitation hardened like CuCrZr) for heat sink, tungsten (pure, solid solution, two-phase) for armour, EUROFER (9Cr1WVTa steels and ODS steels) or stainless steels (typically 304, 316, 1.4970) for structure. Copper alloys have to be considered as medium-high activation materials (due to the element Cu). The commercially available austenitic steels are high activation materials. But in principle, they could be changed into reduced activating variants, following the EUROFER development route. Tungsten materials and EUROFER are low activating.

For DEMO reactor more conservative divertor specifications will be necessary to ensure a broader range of plasma operation scenarios (also as a risk mitigation strategy). For this case, which could be considered as upper limit, likely parameters would be a heat flux capability of minimum 10 MW/m² (temporal average), tolerant to short peaks up to 15-20 MW/m² (or as high as possible). The maximum number of cyclic loads would be 20000 within a lifetime of two full power years. Further, the divertor heat does not necessarily have to be used for electrical power production. Divertor lifetime will be a major factor in the operational costs availability of DEMO or a power plant so it is likely to emerge as a key area for continued improvement.

The neutron irradiation damage of tungsten armour parts at locations with highest heat load, the neutron damage varies between 1 and 5 dpa/fpy [M.R. Gilbert (2013), private communication]. At divertor positions further away from the strike point (upper dome and outer targets), the neutron damage rates can be twice as high although the heat fluxes are significant lower.

In an ITER-like divertor design, the most critical parts are the vertical targets. At present there are two main cooling concepts, which would more or less fulfil the requirements: one is the ITER design (water cooled CuCrZr pipes with attached tungsten mono-blocks), the other is the Helium Multi JET (HEMJ) design, based on small helium jet cooled vertically arranged tungsten fingers (structural parts) with attached tungsten tiles (armour parts) [P. Norajitra et al., Progress of He-cooled Divertor Development for DEMO, Fusion Eng. Des. 86 (2011) 1656–1659]. All possible variations of these two cooling concepts have to be based on structural materials with a very high thermal conductivity. The minimum requirements are estimated to be in the range of 50-100 W/(m K) under operating conditions, depending on the particular design.

Concerning the possible DEMO divertor cooling the state of the art can be summarized as follows.

Efficient He cooling operation requires W as a structural material, allowing sufficiently high temperatures. To deal with heat fluxes in the order of 10 MW/m² is only possible by jet impingement cooling, demonstrated so far only for non-nuclear applications. There is still no structural material which meets all design requirements. All possible tungsten alloys are even more brittle than pure tungsten [M. Rieth, et al., Recent progress in research on tungsten materials for nuclear fusion applications in Europe, J. Nucl. Mat. (2012), doi: 10.1016 / j.jnucmat2012.08.018]. So far, only tungsten composite materials (tungsten foil laminates or fibre reinforced tungsten) have the potential to solve the problem [J. Reiser, M. Rieth, B. Dafferner, A. Hoffmann, Tungsten foil laminate for structural divertor applications – Basics and outlook, Journal of Nuclear Materials 423, 1–8 (2012). J. Reiser, M. Rieth, B. Dafferner, A. Hoffmann, X. Yi, D. E.J. Armstrong, Tungsten foil laminate, for structural divertor applications – Analyses and characterization of tungsten foil, Journal of Nuclear Materials 424, 197–203 (2012).]. It is known that all tungsten based materials will suffer from additional embrittlement under neutron irradiation. To what extent and under which conditions (irradiation temperature, dose, neutron spectrum) is not known yet.

Based on present knowledge on neutron-induced embrittlement of tungsten, an operating temperature of at least 800 °C is strongly recommended to mitigate the risk of embrittlement. For such high temperatures, divertor designs (also different from HEMJ) solely based on structural tungsten materials could be developed. However, in this case, the focus had also to be laid on the technology of the whole cooling loop (also outside the vacuum vessel).

Efficient water cooling operation requires temperature and pressure in the cooling loop which are unfortunately restricted to certain limits. Pressurized water reactor (PWR) technology is the proven state-of-the-art cooling system for nuclear environments. Light water is used as the primary coolant. It enters the reactor core at about 275 °C and is heated up in the reactor core to about 315 °C. The water remains liquid despite the high temperature due to the high pressure (around 15.5 MPa) in the coolant loop. In water, the critical point occurs at 374 °C and 22.1 MPa. So-called supercritical water cooling for

nuclear applications is under investigation but it is far from being mature yet. To safely suppress the formation of a steam phase, the pressure in the primary circuit is maintained by a pressurizer. This is a separate vessel, connected to the primary circuit and partially filled with water which is heated to the saturation temperature. To achieve a pressure of 15.5 MPa, the pressurizer temperature is maintained at 345 °C, which gives a sub-cooling margin (the difference between the pressurizer temperature and the highest temperature in the reactor core) of 30 °C. Thermal transients in the reactor coolant system result in large swings in pressurizer liquid volume. Pressure transients in the primary coolant system manifest as temperature transients in the pressurizer and are controlled through the use of automatic heaters and water spray, which raise and lower the pressurizer temperature, respectively.

The issues in connection with water cooling are tritium barriers which would have to be integrated between the armour and cooling structure to avoid or reduce water tritiation. Therefore, alternatively or in addition, water detritiation and possible control of water chemistry is a topic which has to be addressed, but that will hold for other water-cooled components, e.g. in heating and current drive systems, as well. The ITER divertor is designed for a very low irradiation dose ($\ll 2$ dpa). Therefore, CuCrZr pipes with mounted tungsten monoblocks can be used to dump the divertor heat by water cooling at about 120 °C with a low pressure (4 MPa). Unfortunately, the same design would not work for DEMO because of the neutron embrittlement. Nevertheless, it could be taken as a basis for further modifications. The ITER divertor fulfils the requirements for the heat load given in the upper limit (10 MW/m² average plus short periods up to 20 MW/m²). However, neutron irradiation at such low operating temperatures would cause severe embrittlement of the CuCrZr pipes. On the other hand, at higher temperatures (like at PWR conditions) the irradiation damage would be on a lower level which might be tolerable, but then CuCrZr loses strength. In terms of the heat load, the obvious top-down approach is to copy the ITER divertor design and to replace CuCrZr by a suitable structural material. For this application, reinforced copper composite materials seem to be the most promising choice.

A viable starting point could be to use the fact that a heat load of 5 MW/m² can be removed by a water cooled austenitic steel pipe. The detailed ITER analysis (i.e. the ITER Interim Structural Design Criteria, ISDC, and its data compilation) as well as the on-going analysis for GEN-IV reactors show that 316 L(N) austenitic steel can be operated up to about 7 dpa due to the fact that its total elongation and fracture toughness remain relatively high. In these analyses the drop in uniform elongation limit to 0.4 % after irradiation at temperatures below about 300°C has been taken into account [A-A. F. Tavassoli, "Present limits and improvements of structural materials for fusion reactors – a review", *Journal of Nuclear Materials* 302 (2002) 73–88.]. However, 316 steels have a chemical composition that leads to highly activated isotopes. Therefore, in this approach, a reduced activation stainless steel (RASS) would have to be developed. The operating temperature limit is then given by the performance of this RASS under neutron irradiation. A significant increase of the heat load should be possible by design variation and optimization.

This report presents the achievements in investigations of the DEMO reactor power and particle exhaust physic during of 2013 working year. The results have been reported

- 1) on the 25th Symposium on Fusion Engineering - SOFT-11, San Francisco, June 10-14, 2013 and is accepted for publication in the SOFT proceedings and in the IEEE Transactions on Plasma Science, 2014
- 2) on the 16th International Conference on Fusion Reactor Materials ICFRM-16, in October 20-26, 2013 Beijing, China (paper number FST13-732), and is submitted to the Fusion Engineering and Design.
- 3) on the 11th Symposium on Fusion Nuclear Technology 16 – 20 September 2013, ICFRM-11, Barcelona, Spain and is submitted to the Fusion Engineering and Design.
- 4) on the 14th International Workshop on Plasma Edge Theory in Fusion Devices, PET, 23-25 September, 2013 Cracow, Poland; the paper is submitted to the journal "Contributions to Plasma Physics" and will be published in 2014.

It also contains the final reports of the EFDA tasks:

- 5) on predictive studies of transition from attached to detached states in DEMO divertor; EFDA Task WP13-PEX-01-T01;
- 6) on extended physics assessment of advanced Snow-Flake divertor configuration; EFDA Task WP13-PEX-02-T02 and
- 7) on the novel PFC material solutions for DEMO – Liquid Metals (Lithium). EC ref. number FU07-CT-2013-00054; Deliverable ref. WP13-PEX-03B-T05-01/KIT/PS

In Chapter 1 the modelling of DEMO PFC erosion due to ELM is discussed. We analyse the impact of edge localized modes (ELMs) on the divertor target and the first wall surface. The expected ELMs characteristics in DEMO are derived by extrapolating predictions made for ITER and by using the scaling arguments found from existing experiments. The tungsten armour damage and effect of melt layer motion due to the repetitive ELM loads is numerically investigated by using the MEMOS code. It is shown that due to unmitigated repetitive ELM impact, the divertor plate melts whereas the first wall does not. The divertor surface of mono-block W divertor module with water coolant tolerates the mitigated ELMs with ~33 times higher frequency, as in ITER, and does not melt even in the case of advanced version of DEMO loads.

In Chapter 2 we analyse thermal performance of the DEMO plasma facing component (PFC) of W alloy mono-block design with Cu OFHC / EUROFER water coolant tube under steady-state and the transient edge localized modes (ELMs) loads during DEMO I and DEMO II operations. The W surface melting and evaporation due to the repetitive ELMs impact and effect of vapour shielding is numerically investigated by using the MEMOS code (Bazylev, 2002). The maximum temperatures in the interfaces between the materials as well as heat flux into the water coolant are calculated and compared with allowable temperature limitations of materials under neutron irradiation and the power water reactor (PWR) constrains. The feasibility of the PFC module design under DEMO heat loads is assessed.

In Chapter 3 the thermal performance of different modules of plasma facing components (PFC) is analysed for the DEMO reactor conditions in steady-state operation with the inclusion of the transient edge localized modes (ELMs) for mitigated and un-mitigated cases. As an example the effect of these loads is considered for the W alloy mono-block design with Cu OFHC/EUROFER water coolant tube first

proposed in the framework of the PPP&T divertor study. A variant of this design with EUROFER tube connected to the W block with a diamond/copper composite (DCC) used in the diagnostic windows, is also analysed. A design goal is to find the optimal thicknesses of material layers, which allow one to keep the maximum temperatures within the allowable design limits under ITER water cooling conditions. Heat transfer and armour erosion due to the plasma impact has been modelled by using the MEMOS code.

In chapter 4 the conversion of magnetic energy of runaway electrons into thermal energy is considered during the massive gas injection.

In Chapter 5 the sizing of the inner fuel cycle of a fusion machine is defined by the machine gas throughput and composition, and the sub-divertor neutral pressure at which the exhaust gas has to be pumped. Realisation of detachment conditions, improved understanding of the sub-divertor flow patterns and aspects of core fuelling are discussed as examples. The detachment onset conditions in conventional DEMO divertor is derived by using one-dimensional transport numerical model. Based on the derived detachment criterion the requirements on the gas throughput and the requirements for the gas exhaust vacuum system are formulated. The analysis aims at the obtaining of number of cryopumps required for steady-state operation under detached divertor conditions.

In Chapter 6 we assess some important physics issues related to the snowflake (SF) divertor configuration, namely effect of flux expansion/connection length/poloidal length on stability of impurity radiation in SF configuration and the coupling of MARFE with the ballooning type MHD instability.

In Chapter 7 we discussed an analytical transport model of the edge tokamak plasma, suitable for implementation into the integrated code TOKES and in perspectives for implementation into System integrated Code for predictive modelling of the fusion reactor DEMO. The transport model provides plasma density, temperature and velocity distribution along and across the magnetic field lines in bulk and the edge plasma region. It describes the dependence of temperature and density at the separatrix on the plasma conditions at the plate and the efficiency of the divertor operation, depending on power and particle sources. The calculation gives eventually the power and particle loads on the divertor plates and side walls.

In Chapter 8 the modelling of Li surface erosion under ITER and DEMO Type I ELM high power loading, which includes melting and evaporation, molten layer flow and deformation caused by the magnetic fields and thermo emission current and effect of shielding owing to the Li evaporation is described. The 3D version of the predictive code MEMOS has been employed. The behaviour of liquid metal both in a Capillary Porous System (CPS) structure and as free flowing films are considered.

In Attachments some additional results and data, required for calculations are presented.

1 Modelling of DEMO PFC Erosion due to ELM impact

Abstract.-The transient events could pose a severe threat causing melting and erosion of plasma facing components in the fusion power plant DEMO. Here we analyze the impact of edge localized modes (ELMs) on the divertor target and the first wall surface. The expected ELMs characteristics in DEMO are derived by extrapolating predictions made for ITER and by using the scaling arguments found from existing experiments. The tungsten armor damage and effect of melt layer motion due to the repetitive ELM loads is numerically investigated by using the MEMOS code. It is shown that due to unmitigated repetitive ELM impact, the divertor plate melts whereas the first wall does not. The divertor surface of monoblock W divertor module with water coolant tolerates the mitigated ELMs with ~ 33 time higher frequency, as in ITER, and does not melt even in the case of advanced version of DEMO loads.

1.2 Introduction

High pedestal pressure, required for good core confinement in DEMO plasma, may lead to disadvantages of the increased edge localized modes (ELMs) energy loss to the plasma facing components (PFC) [1]. We consider here the PPCS model C DEMO design with the major radius $R=7.5\text{m}$, the aspect ratio $A=3$, the toroidal magnetic field $B=6\text{T}$ and the safety factor $q_a=4.5$ [2]. We also do some estimation for recently suggested two versions of DEMO, which are based on a near future technology DEMO1 and on steady-state technologically advanced DEMO2 [3]. A sandwich type module made of W-clad EUROFER steel (Fig. 1a) and a pure tungsten divertor module (Fig. 1b) are examined here against heat loads impact due to the ELMs as the first wall (FW) and divertor target for DEMO. The modules consist of a water coolant tube of rectangular cross-section within the EUROFER (a) or W (b) matrix that are used as a heat diffuser [4,5]. Although W/EUROFER bond is of "low-activation" type, it has relatively low creep temperature (823°K) and EUROFER has limited heat diffusivity, which could be the drawback of EUROFER as a heat diffuser. Water is used as a coolant both in the FW blanket module and in the W divertor. In this paper we first derive the characteristics of ELMs in DEMO based on scaling arguments. Then the effect of ELMs on the tungsten armor melting and roughness formation. The magnitude of roughness after many ELMs is simulated applying the quasi-one-dimensional fluid dynamics model, which describes the motion of melted material along the surface in the 'shallow water' approximation of the Navier-Stokes equations with the surface tension, viscosity of molten metal and the radiative losses from the hot surface taken into account. Details of this model used in MEMOS code are presented. Then, the effect of mitigated ELMs is calculated. Finally we discuss the viability of W/EUROFER sandwich type module and W mono-block module under DEMO ELM conditions.

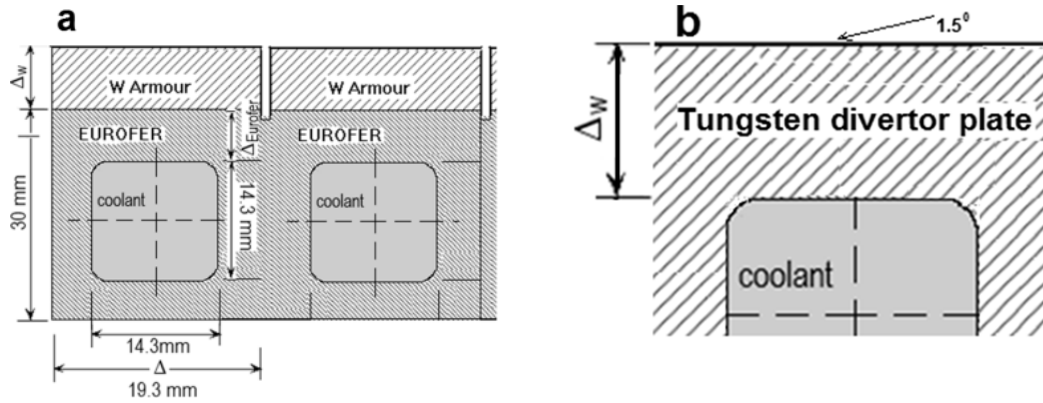


Fig. 1 (a) Mock-up of W/EUROFER sandwich type castellated module (two segments are shown) $\Delta w = 3\text{mm}$, $\Delta_{\text{EUROFER}} = 4\text{mm}$ with cooling channel imbedded into EUROFER, (b) W monoblock divertor module with embedded cooling channel; $\Delta w = 8\text{mm}$. PFC. Models are used for the ENDEP computation of the ELMs impact [6].

1.3 Specification of Type I ELMs in DEMO

In ITER the thermal energy ΔW_{ELM} released during unmitigated ELM is expected to be $\sim 20\text{MJ}$. The deposition time on the divertor plates is about 0.25ms (rising phase) and 0.5ms (decay phase). The peak energy on inboard divertor is $\sim 0.5\text{--}4\text{MJ/m}^2$ [3,7,8]. In DEMO the ELM characteristics can be derived based on scaling arguments by extrapolating data envisaged for ITER and the data from the large-scale tokamaks.

The ELM energy deposition to the divertor. The ELM plasma energy loss ΔW_{ELM} to the divertor is proportional to pedestal energy W_{ped} and correlated with the pedestal collisionality ν^* (Fig.2) and with the ion losses time $\tau_{//}$ along the magnetic field lines to the divertor target (Fig.3) [9]. For DEMO1/DEMO2 design parameters ($R \sim 8.5/9\text{m}$, $q_{95} \sim 3/4.5$, $n_{\text{ped}} \sim 0.8/1.25 \cdot 10^{20}\text{m}^{-3}$, $T_{\text{ped}} \sim 7.0/7.8\text{keV}$ and plasma volume $V_{\text{ped}} \sim 1527/2275\text{m}^3$ [3]) the pedestal energy can be estimated as $W_{\text{ped}} \approx 3n_{\text{ped}}T_{\text{ped}}V_{\text{ped}} \sim 410/610\text{ MJ}$. The normalized pedestal collisionality $\nu^* = \nu_{\text{ped}} \cdot q_{95}R/Cs \approx 0.46 \cdot q_{95}R(m)/T^2(\text{keV}) \sim 0.015/0.021$ is smaller than for ITER (~ 0.036), mainly because of higher DEMO pedestal temperature. As it seen from Fig.2 at that collisionality Δw ELM is about 25-30% of the edge pedestal energy W_{ped} . The correction due to the finite ion loss time [7] $\sim (1 + \tau_{//}/\tau_{\text{ELM}})^{-1}$ is estimated as ≈ 0.7 (see below). Therefore, in DEMO1/2 the thermal energy ΔW_{ELM} for unmitigated ELM must be expected in the range of $\sim 80/160\text{MJ}$. Maximum of the ELM energy loads due to in/out asymmetry [10] should be in inboard divertor about 50/110MJ and in outboard divertor $\sim 40/80\text{MJ}$. We further assume that the shape of ELM power loading at the mid-plane is the same as in ITER and the ELM decay phase is twice of that of rising phase. The full width at half maximum Δ varies and for the case of poloidally tilted plate on angle $\sim 20^\circ$ the ELMs deposited area on the plate is assumed to be about $\sim 2\pi R \Delta / \cos 20^\circ \approx (2.5\text{--}3)\text{m}^2$. Here Δ depends on the magnetic connection length in the SOL and can be estimated based on the ELM model [11] as $\sim 0.05\text{--}0.07\text{m}$ (similar to ITER). Therefore, one can expect that for DEMO1 energy density load to the out-inboard divertor plates could vary in the range of $15\text{--}20\text{MJ/m}^2$ for with energy

deposition time (see below) about 0.6ms (rising phase) and 1.2ms (decay phase). Maximum energy density parallel to B on inboard diverter is estimated as $Q// \sim 20 \text{MJ/m}^2 \cdot q_{95} R / a \approx 400 \text{MJ/m}^2$.

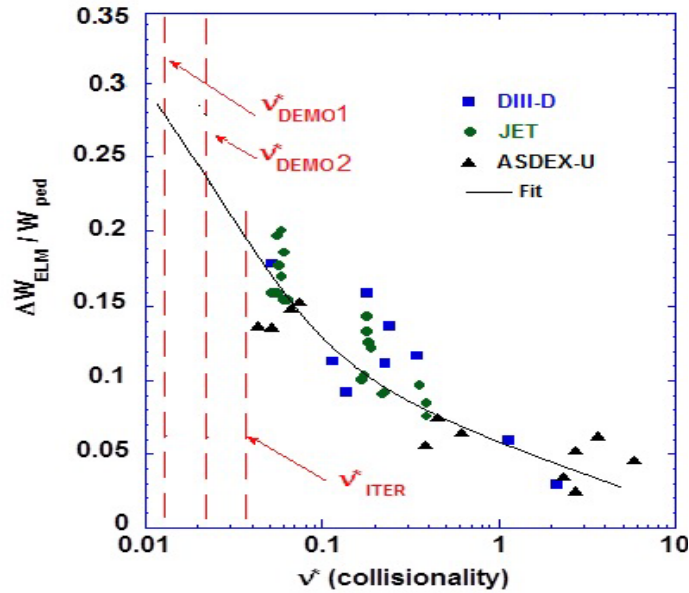


Fig. 2 Normalized ELM energy loss fraction as a function of collisionality v^* at the pedestal for various machines [8] and for DEMO versions (intersections between dashed lines with the fit curve); W_{ped} is the energy stored in pedestal before an ELM crash.

The ELM energy deposition time can be assessed as $\tau_{ELM}(\mu\text{s}) = 0.29 \cdot (\tau // (\mu\text{s}))^{1.38} \approx 580 \mu\text{s}$ [12]. This time corresponds to the ELM rising phase and according to experiments (see Fig.4) is well correlated with the characteristic time for ion transport from the pedestal to the divertor, $\tau_{//} = 2\pi R q_{95} \cdot (1 + (3/2)0.5 \cdot v^*) / C_{s,ped} \sim 250 \mu\text{s}$, where $C_{s,ped} \sim 7 \cdot 10^5 \text{m/s}$ is the ion sonic speed calculated from plasma pedestal temperature $\sim 7.8 \text{keV}$, $R = 8.5 \text{m}$ and $q_{95} \sim 4.5$. The good correlation of τ_{ELM} suggests that convective transport is important for ELM heat deposition to the divertor at low collisionality in the SOL, expected for DEMO [13] (see Fig.2). If conduction dominates the ELM energy transport in DEMO then (1-2)ms will likely be the timescale range. The fraction of ELM energy transported as particles would likely arrive at the target with a time duration $\sim 0.2 \text{ms}$.

The Type I ELM frequency. For extrapolation to DEMO one can use the fact that the Type I ELM frequency scales as $f_{ELM} \sim (\tau_E)^{-1/7}$ [13], where τ_E is the energy confinement time. The confinement time for the H-mode ELMy discharges in DEMO is $\tau_{IPB98(y,2)} \sim 6.47 \text{sec}$ [2], which exceeds ~ 1.8 times the confinement time for ITER. Consequently, the ELM frequency in DEMO is about 0.8 Hz which is slightly lower than in ITER ($\sim 1-2 \text{Hz}$) [7].

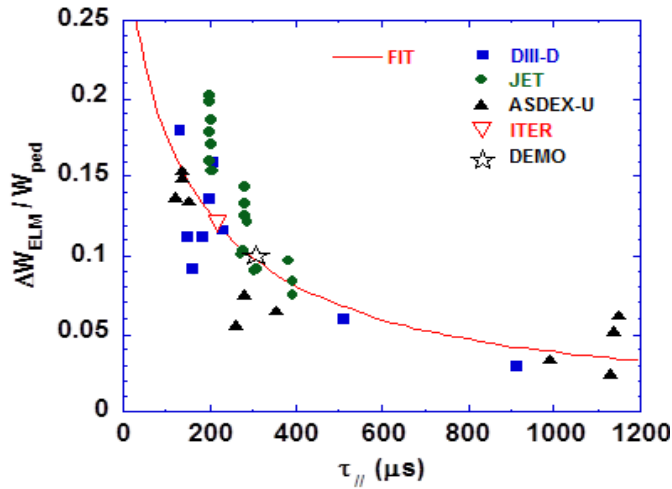


Fig 3. Normalized ELM energy loss fraction as a function of characteristic time for ion flux to divertor for various machines and ITER [7,8]; the ELM loss fraction for DEMO is indicated; W_{ped} is the energy stored in pedestal before an ELM crash.

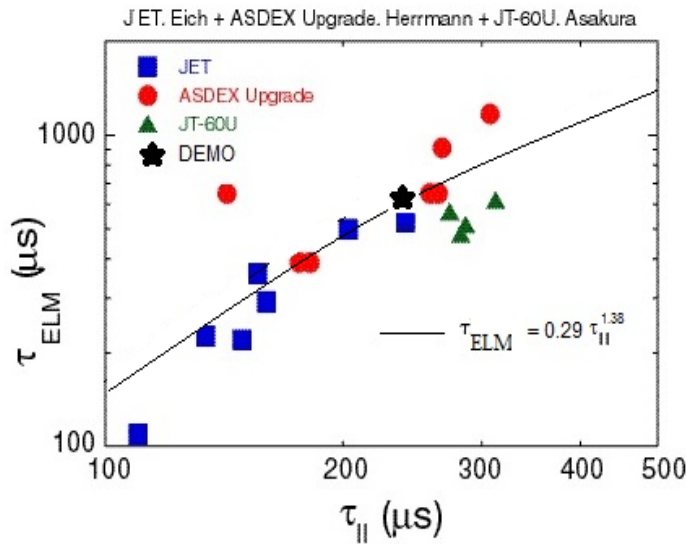


Fig.4 The ELM energy deposition time (rising phase) as a function of characteristic time for ion flux to divertor [12]. The DEMO point is indicated.

ELM deposition on the DEMO first wall. The ELM deposition on the DEMO first wall (FW) is assumed in agreement with experiments to be 5-20% of the ELM energy lost from the main plasma [14] and is derived for unmitigated ELMs as $Q_{\perp} \approx Q // \bullet \Delta / \pi q_95 R \sim 0.1 \div 0.2 MJ/m^2$. As it seen from experiments [15] the ELM deposition time on to the FW is about half of that on outer divertor and is 0.6ms.

The mitigated ELMs in DEMO. The controlled ELMs in DEMO can be assumed as a pace making by pellet injection or by control coils. Similar to ITER we suggest that the amplitude can be reduced ~ 33 times, so that the energy loss over 1.2ms is reduced down to $0.6 MJ/m^2$ and, since the product of amplitude and

frequency remains unchanged for the Type I ELMs, the frequency increases up to ~ 26 Hz. Table I summarized the characteristics of DEMO1 ELMs for the inboard divertor case discussed above.

Table I

	JET [1]	ITER [2]	DEMO1 [3] divertor/FW unmitigated ELMs	DEMO1 divertor mitigated ELMs
Energy loss per ELM, MJ	0.0045	20	80-100/10-15	3
ELM frequency, Hz	10	2	0.8/0.8	26
ELM deposition time, ms	0.1	1	1.2/0.6	1.2
ELM deposited area, m ²	0.43	0.68	2.75/90	2.75/90
Peak deposition energy, MJ/m ²	0.01 inboard	0.5 inboard	15-20/ ~ 0.2 inboard	0.6 inboard

A strong erosion is expected due to the impact of unmitigated ELMs on tungsten armor, resulting in surface melting and melt splashing [4,5]. In DEMO the unmitigated ELM energy will exceed melting threshold. The heat loads typical of single giant ELMs result in melting and evaporation, and in a vapor shield formed in front of the target [6]. Melt motion produces surface roughness that usually significantly exceeds the vaporization erosion per one ELM. In assumption of rather high melt splashing the dependences of the number of ELMs to erode 1 cm of W armor on the ELM energy WELM were calculated in [3] with the conclusion that ELMs with $WELM > 1.25 \text{ MJ/m}^2$ and the duration $\tau_{ELM} = 0.3 \text{ ms}$ are unacceptable.

I.4 The model for melt-motion simulation

The magnitude of roughness after many ELMs with the heat loads over the divertor surface is simulated applying the quasi-one-dimensional fluid dynamics code named MEMOS (Melt Motion at Surfaces). The motion of melted material along the surface is described in the 'shallow water' approximation of the Navier-Stokes equations, with the surface tension, viscosity of molten metal, and the radiative losses from the hot surface taken into account. The plasma pressure gradients along the divertor plate, as well as the gradient of surface tension and the JxB force of the currents crossing the melt layer immersed in a strong magnetic field, produce the melt acceleration.

For a derivation of the mathematical model for melt motion the following assumptions are used here: the thickness of the melt layer is much smaller than the width of the molten layer and pressure gradients across the melt layer are absent. Therefore there exists only a velocity component parallel to the surface and a melt velocity averaged over the molten layer can be used for description of the melt motion. In this case the “shallow water” approximation can be applied for the mathematical description of the melt motion [16]. The fluid is assumed to be incompressible. Temperature dependent thermo-physical data are used. The physical processes taken into account in the numerical model are: heating, melting, evaporation from the surface and resolidification, heat transport in the liquid and the solid, viscosity and melt motion by the following forces: surface tension, total external pressure, Lorentz force due to external and Eddy currents.

The base system of Navier-Stocks equations [17] together with the heat conductivity equation describe the parameters of molten W layer and heat diffusion towards cooling channel (see Fig. 1a,b):

$$\operatorname{div} \mathbf{v} = 0 \quad (1)$$

$$\rho \left(\frac{\partial \mathbf{v}}{\partial t} + \mathbf{v} \nabla \mathbf{v} \right) = -\operatorname{grad} p + \mu \Delta \mathbf{v} + F_{Lorentz} \quad (2)$$

$$\rho C \frac{\partial T}{\partial t} + \mathbf{v} \operatorname{grad} T = \nabla (\kappa \nabla T) + Q \quad (3)$$

with $\mathbf{v}, T, \rho, C, \kappa$ are the velocity, the temperature, the density, specific heat and heat conductivity, viscosity of the melt, p is pressure, Q is the sum of volumetric energy deposition and Joule heating. The following boundary conditions are applied at the liquid vapor boundary:

$$-\kappa \frac{\partial T}{\partial n} \Big|_{surf} = W(t) - \rho V_{ev} \Delta H_{ev} \quad (4)$$

$$\mu \frac{\partial u_y}{\partial n} = \frac{\partial \alpha}{\partial y}, \quad \mu \frac{\partial u_z}{\partial n} = \frac{\partial \alpha}{\partial z}, \quad (5)$$

here in (4) temperature gradient is calculated at the surface along the normal coordinate to the surface (x -coordinate), $W(t)$ is surface heat load, ΔH_{ev} is enthalpy of evaporation. In (5) u_y, u_z is velocity component along the surface, α is surface tension coefficient. The classic Stefan boundary condition is applied to the solid liquid boundary. At the melting front ($n=N_m$) the velocity of the melt motion assumed to be zero here n is normal to the melt front.

$$\kappa_s \frac{\partial T_s}{\partial n} \Big|_{n=N_m} - \kappa_l \frac{\partial T_l}{\partial n} \Big|_{n=N_m} = \rho V_m \Delta H_m \quad (6)$$

here index s refers to the solid and index l to the liquid phase, V_m is velocity of melting front propagation, ΔH_m is ^{enthalpy} of melting.

The shallow water approximation allows simplifying the system of Eqs. (1)–(3) with the boundary conditions (4)–(6) to a system of quasi 2-D equations. The fluid velocity is averaged over the melt layer thickness assuming a parabolic dependence. After averaging Eqs. (1) and (2) with the boundary condition (Eq. (5)) the system of equation of the St. Venant type [18] is derived:

$$\frac{\partial h}{\partial t} + \frac{\partial(u_y h)}{\partial y} + \frac{\partial(u_z h)}{\partial z} = V_{ev} + V_m \quad (7)$$

$$\begin{aligned} \frac{\partial u_y}{\partial t} + u_y \frac{\partial u_y}{\partial y} = & -\frac{1}{\rho} \frac{\partial p}{\partial y} - \frac{u_y}{h} V_m + \nu \frac{\partial^2 u_y}{\partial y^2} - \\ & 3\nu \frac{u_y}{h^2} + \frac{3k_\alpha}{2\rho h} \frac{\partial T}{\partial y} + \frac{J_z B_y}{\rho c} \end{aligned} \quad (8)$$

$$\begin{aligned} \frac{\partial u_z}{\partial t} + u_z \frac{\partial u_z}{\partial z} = & -\frac{1}{\rho} \frac{\partial p}{\partial z} - \frac{u_z}{h} V_m + \nu \frac{\partial^2 u_z}{\partial z^2} - \\ & 3\nu \frac{u_z}{h^2} + \frac{3k_\alpha}{2\rho h} \frac{\partial T}{\partial z} + \frac{J_y B_z}{\rho c} \end{aligned} \quad (9)$$

Here ν is the kinematic viscosity, J_z, J_y component of the current, B_y, B_z the toroidal magnetic field components, T melt temperature, and instead of α the negative coefficient given by $k_\alpha = d\alpha/dT$ is used, V_{ev} velocity of the surface caused by the evaporation. h is the thickness of the melt layer. The equations describing the evolution of the normal velocity at the surface V_{fs} and the heat transport along the surface remain also intact:

$$V_{sf} = V_{ev} - \frac{\partial(u_y h)}{\partial y} - \frac{\partial(u_z h)}{\partial z} \quad (10)$$

$$\frac{\partial T}{\partial t} + u_y \frac{\partial T}{\partial y} + u_z \frac{\partial T}{\partial z} = \frac{3\nu}{C} \frac{u_y^2}{h^2} + \frac{3\nu}{C} \frac{u_z^2}{h^2} \quad (11)$$

The 3D Stefan problem Eq. (3) for moving boundaries attached to re-solidification, melting and vaporization fronts is solved using the splitting method.

As it was mentioned, the melt motion is generated by the thermo-emission current in the TEXTOR experiments. For a good agreement with the experiment the model of space-charge limited thermo-emission current based on the modified Child-Langmuir expressions [19] is implemented into the code MEMOS instead of Richardson-Dushman formula. Free parameters entering into the expressions are fitted so that calculated current is in a correlation with the experimental values. A 3D heat transport equation with two boundary conditions at the moving vapor-liquid- and liquid-solid interfaces describes

the temperature inside the target. Temperature dependent thermo-physical data are used [20]. The model of the plasma shielding well developed, validated against experiments at plasma gun facilities, and described in details in [21] have been implemented into the code MEMOS to take into account influence of the evaporated material on the surface heat loads.

The ELMs heat load varies in time due to a vapor shielding in front of the target (~5-10 ms). Evolution in time of the surface heat load and pressure are calculated by FOREF code [22] and shown in Fig. 5 and 6. Several scenarios for single and repetitive ELMs are modeled with the target width of 0.2m. For many ELMs the case with fixed separatrix strike point (SSP) position is compared with that of the SSP Gaussian distribution of $f = 0.1$ m. The directions of magnetic field and the current are chosen to result in the Lorentz force generating the downstream melt motion (see Figs.5 and 6).

1.5 Erosion due to unmitigated ELMs

Calculation have been perform by assuming, that the ELM power deposition profile varies in time as $q(t)=q_m \cdot (1+(\tau_m/t)^2) \cdot (\tau_m/t)^2 \cdot \exp(-(\tau_m/t)^2)$, where $\tau_m \approx 0.8\tau$ and τ is the duration of ELM fast rise phase [26]. It is expected that in DEMO unmitigated ELMs could produce unacceptable levels of erosion. Melting of divertor target occurs when the surface temperature becomes equal or exceeds the W melting point. Because of a large number of ELMs ≥ 10000 is expected during 2h steady-state DEMO2 operation it is important that the surface temperature rise due to an individual ELM remain well below the melting threshold. Experiments have shown that melting of the W target due to Type I ELM impact occurs for energies $\geq 1MJ/m^2$ depositing over 0.5ms [27], which corresponds to a so called damaging parameter for tungsten $\sim 45MJ/m^2/vs$. In the case of DEMO the unmitigated ELM energy load to the divertor plate (up to $20MJ/m^2$ over 1.2ms) exceeds several times the damaging parameter and an unacceptable level of erosion may occur. Even heat load of a single ELM could result in surface melting. The simulation of the melt motion layer in the case of DEMO W armour is similar to calculations done previously for ITER in [28]. For multiple events the total erosion is evaluated by direct simulation of each ELM impact on the eroded surface produced by previous ELM. Several scenarios for single and repetitive ELMs are modelled with the target width of 0.06m. The profiles of heat load on the plate and plasma pressure are calculated as described in [28].

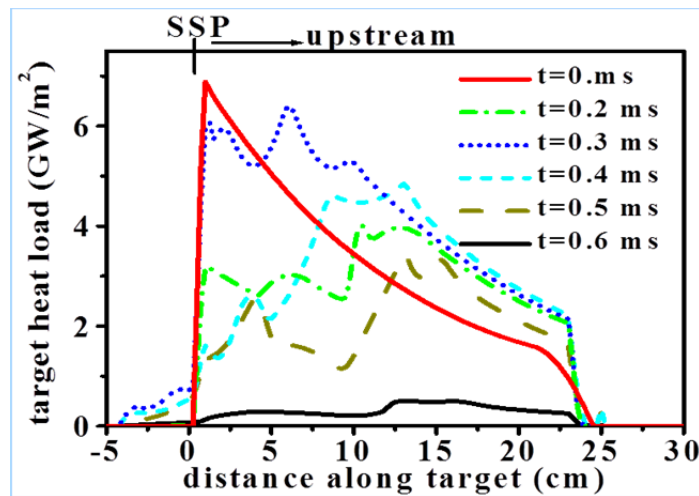


Fig.5 Effects of vapor cloud screening calculated by FOREF-2 code (see details in [22]). Evolution of plasma heat load along the tungsten divertor plate surface for ELM energy 3.5MJ/m^2 and deposition time 0.5ms . Heat load to the surface drops due to radiation and erosion energy losses.

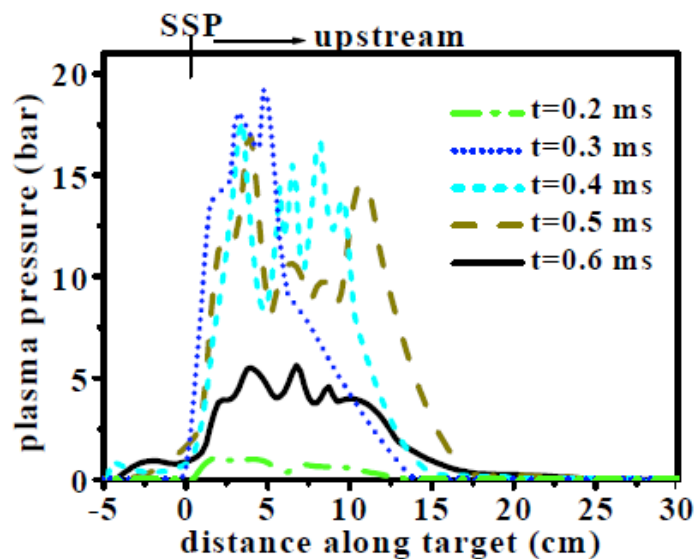


Fig.6 Effects of vapor cloud screening calculated by FOREF-2 code (see details in [22]). Evolution of plasma pressure profiles along the divertor plate for ELM energy 3.5MJ/m^2 and deposition time 0.5ms . Plasma pressure to the surface drops due to vapor expansion along the magnetic field lines and due to radiation and erosion energy loss.

Calculations demonstrate that for reference scenario ($\sim 12\text{MJ/m}^2$ and $\tau_{\text{ELM}} \sim 0.5\text{ms}$) the depth of melt pool is always below $80\ \mu\text{m}$ and the re-solidification between ELMs $\sim 1/f_{\text{ELM}} \approx 1.25\text{s}$ occurs within 2-2.5 ms due to mainly radiative losses. The magnitude of surface roughness is of $0.1\text{-}0.3\ \mu\text{m}$ ($\sim 60\ \mu\text{m}/660$), V of $0.5\ \text{m/s}$, and the evaporation thickness of $0.015\ \mu\text{m}$ ($\sim 10\ \mu\text{m}/660$) as follows from Fig 7. The reduced single ELM energy load of $1\text{-}2\ \text{MJ/m}^2$ could produce melting without evaporation and surface roughness after re-solidification is of small fractions of micron, due to the melt motion with melt velocity V less than 0.1

m/s. Tungsten molten layer moves along the surface and the formation of “hills” and “wells” occurs due to a plasma pressure gradient force, which acts oblique to the divertor plate. The resulting surface roughness usually significantly exceeds the vaporization erosion per one ELM.

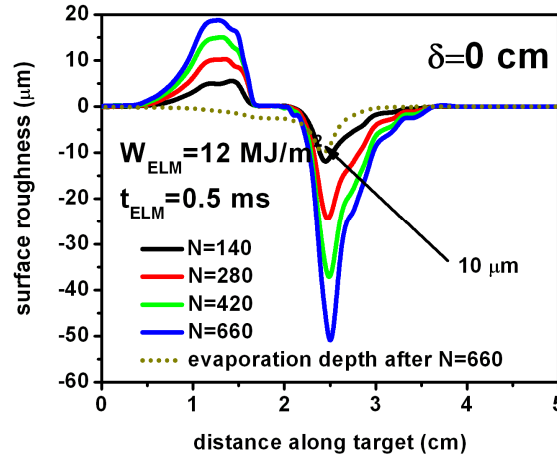


Fig. 7. Effect of multiple ELMs with a fixed strike point position ($\delta=0$), pressure gradient acts along the plate surface. N is the number of repetitive ELMs.

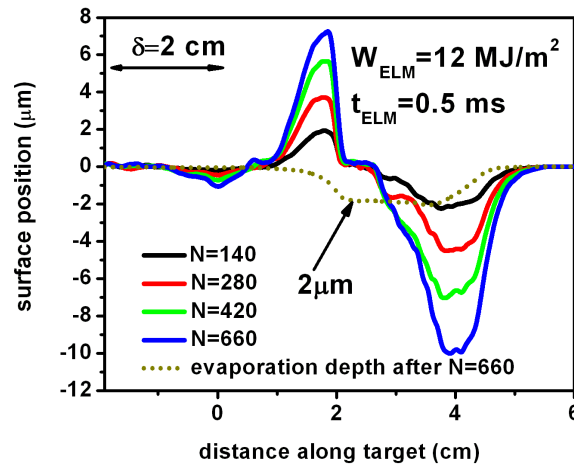


Fig.8. Surface roughness after N ELMs for the SSP Gaussian distribution with $\delta = 2$ cm. N is the number of repetitive ELMs. Clear reduction of surface roughness is seen.

The roughness on tungsten surface caused by molten layer motion due to the ELM heat loads after N repetitive ELMs is shown in Figs.7, 8. Due to the ELM repetition the total roughness may accumulate and become $\geq 20\mu\text{m}$ (see Fig. 7). Profiles of surface roughness after N series of ELMs are shown in Fig. 7 for the fixed strike point position (SSP). At fixed SSP, the crater depth reaches $50 \mu\text{m}$ after 660 ELMs ($\sim 10\mu\text{m}$ due to the evaporation).The heat flux profiles of Type I ELMs in experiments show a clear peak near the separatrix strike point (SSP) with random spatial variations of SSP position of heat flux for sequential ELMs [29].

We assume that the position of SSP at the divertor plate stochastically moves obeying the Gaussian distribution, with the dispersion δ up to 0.02 m. Calculations show (Fig.8) that the Gaussian distribution of SSP with $\delta=0.02$ m results in significant decrease of the crater depth: down to 10 μm and the evaporation results up to 2 μm .

1.6 Unmitigated ELMs load on the DEMO FW

For the FW the expected energy deposition for one ELM $\sim 0.2\text{-}0.5\text{MJ/m}^2$ over 0.6ms corresponds to the damaging factor $\sim 8\text{-}20\text{MJ/m}^2\text{Vs}$, which is below the critical value $45\text{ MJm}^{-2}\text{ s}^{-1/2}$ for tungsten armor. The calculation shows that under multiple impacts of mitigated ELMs the FW temperature saturates at a level well below the W melting temperature (Fig. 9). This is true both for versions of DEMO with 5 MW/m^2 and 8.9 MW/m^2 of stationary plasma power loads.

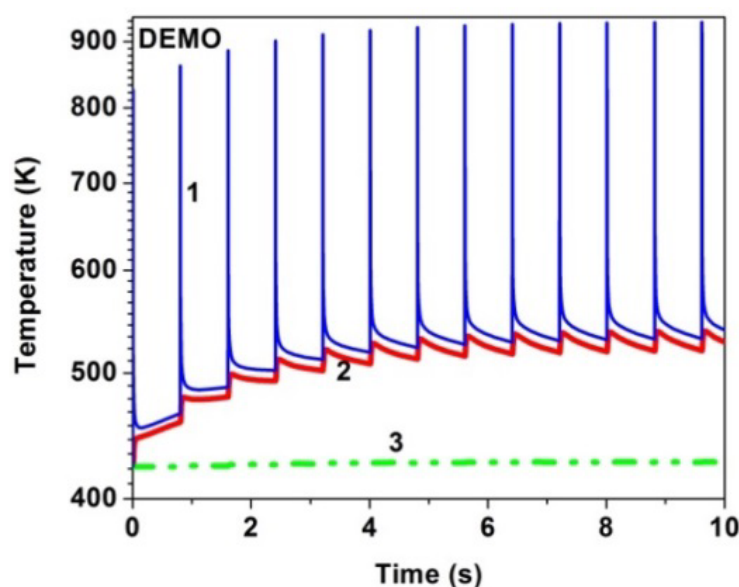


Fig.9 The temperatures of the FW tungsten armor (1), the interface between the W armor and the EUROFER (2) and the water channel (3). Unmitigated ELM power loads on the FW (0.2MJ/m^2 , 1.2sec, 0.8Hz). Steady state heat load 0.5MW/m^2 .

1.7 Effect of mitigated ELMs on DEMO divertor

Effect of unmitigated ELMs heat loads in DEMO1 is shown in Fig. 10 for two different types of divertor modules. In the case of sandwich type W/EUROFER module with imbedded into EUROFER water cooling tube, the W armor surface melts after about 3sec of operation. This happens due to insufficient heat diffusivity of EUROFER. In the case of W monoblock divertor module (as it seen in Fig.11) surface temperature of divertor plate saturates after repetitive ELMs impact and remains below the melting point at the temperature about 2800 K. Note, that stationary power load in this case is 5MW/m^2 which exceeds the mitigated ELM load ($\sim 0.5\text{MW/m}^2$) almost in order of magnitude. Even in the case of DEMO2 with stationary power load of about 8.9MW/m^2 the W surface temperature saturates at values less than the melting point.

Water considered here as a coolant is expected to be in supercritical stage ($>647\text{K}$) at the pressures $\geq 22\text{MPa}$. Bearing in mind that supercritical water as a coolant has disadvantages-could enhance corrosion with EUROFER and react with W causing hydrogen release, we, nevertheless, employing water due to its high heat transfer coefficient [30]. In Fig. 12 the temperatures of the cooling channel embedded into W (upper curve) and the cooling channel embedded into EUROFER (lower curve) are shown in the case of mitigated ELMs. One can see that the temperature saturates readily in W case than in the case of EUROFER because of relatively small heat diffusivity of the stainless steel.

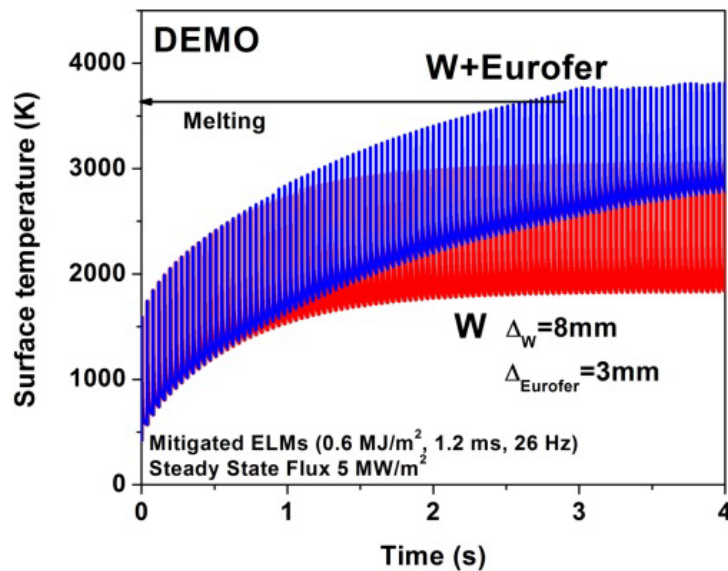


Fig.10 The tungsten temperature increase in time due to the mitigated multiple ELM impact for sandwich type divertor (blue). After about 3s the melting of W armor occurs. A pure W divertor module (the surface temperature shown in red remains below the melting point 3695K) withstands ELMs; the stationary heat load of 5MW/m^2 .

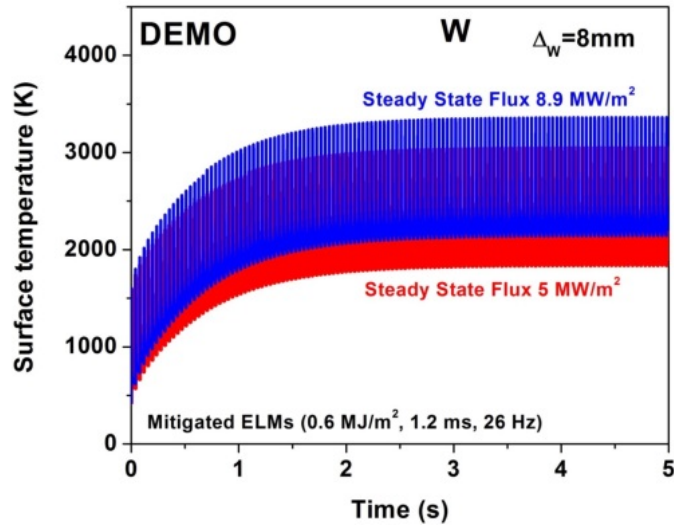


Fig.11 The temperature increase of the W monoblock divertor module surface under mitigated ELMs impact in the case of stationary heat load of 8.9MJ/m² (blue) (for DEMO2) and in the case of 5MW/m² (red) (for DEMO1). In both cases W divertor withstands mitigated ELMs.

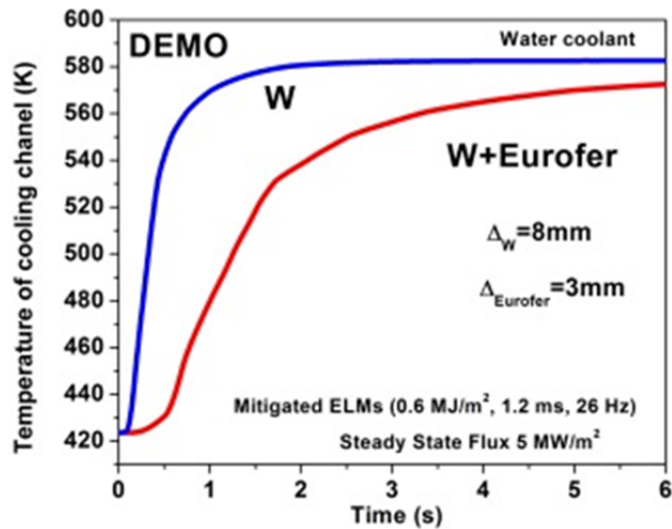


Fig. 12 The temperature rise of the cooling channel embedded into W (upper curve) and into EUROFER (lower curve) in the case of mitigated ELMs impact (0.6MJ/m², 1.2ms, 26Hz); stationary heat load 5MW/m²; Δ_w=8mm; Δ_{EUROFER}=3mm; water coolant.

1.8 Conclusions

The main signatures of the Type I ELMs in DEMO are derived based on scaling arguments, predictions for ITER and data from experiments. Thermal energy release during ELMs is assessed as 80-100MJ, the ELM frequency of 1-0.8Hz and the deposition time about 1.2ms. For existing DEMO designs this corresponds about 15-20MJ/m² of deposition energy to the inboard divertor (spatially average value).

Two types of PFC modules with water coolant are examined against the multiple ELMs impact in DEMO: a W/EUROFER castellated sandwich type module for divertor and the FW and the entirely made from W divertor module.

Calculations show, that under uncontrolled ELMs the W divertor plate melts and evaporates. The vapor pressure gradient causes intensive motion of tungsten molten layer with the velocity of 0.5 m/s and the surface roughness of 0.1 μm per ELM. However, the melt splashing does not develop at that velocity and, therefore, all metallic mass losses are mainly due to target evaporation.

The separatrix strike point random “motion” on the tungsten divertor plate during the repetitive uncontrolled ELMs does not prevent from melting but the total surface erosion becomes essentially smaller.

Power load of uncontrolled ELMs on the FW W armor is tolerable. The tungsten armor temperature of the sandwich type FW module during the operation saturates at the value much less than the melting point (~950K).

The controlled ELMs with ~33 times reduced amplitude (as it is in ITER) are still causing the W surface melting in a sandwich type of divertor module with water cooling due to low heat removal capability. However, the monoblock W divertor module tolerates heat loads of controlled ELMs even for large steady state heat load of 8.9MW/m² envisaged for advanced DEMO version.lectus.

Acknowledgments

This work, supported by the European Communities under the contract of Association between EURATOM and Karlsruhe Institute of Technology, EURATOM and CCFE, was carried out within the framework of the European Fusion Development Agreement. The views and opinions expressed herein do not necessarily reflect those of the European Commission).

One of the authors (Yu. I.) acknowledged L. Boccaccini for using the model of the DEMO FW blanket module and truthful discussion.

1.9 References

- [1] ITER Physics Basis, Chapter 9: ITER contributions for Demo plasma development.
- [2] D. Maisonnier, D. Campbell, I. Cook, L. Di Pace, L. Giancarli, J. Hayward., "Power plant conceptual studies in Europe", Nucl.Fusion 47 (2007) 1524
- [3] DEMO Design Summary, EFDA_D_2L2F7V v1.0
- [4] Yu. Igitkhanov, B. Bazylev, Fusion Science and Technology, 60 (1) (2011), 349.
- [5] Yu.Igitkhanov. B. Bazylev, "Evaluation of energy and particle impact on the plasma facing components in DEMO", Fusion Engineering and Design, 87, Issues 5–6, 2012, 520
- [6] B. Bazylev, H. Wuerz, J. Nucl. Mater. 307-311 (2002) 69
- [7] A. Loarte et al., 2003 Plasma Phys. Control. Fusion 45 1549; A. LOARTE, et al., "Predicted ELM energy loss and power loading in ITER-FEAT", Fusion. Energy 2000 (Proc. 18 th. Int. Conf. Sorrento, 2000), IAEA, Vienna
- [8] A Loarte, G Saibene, R Sartori, V Riccardo, P Andrew, J Paley, "Transient heat loads in current fusion experiments, extrapolation to ITER and consequences for its operation", Phys. Scr. T128 (2007) 222–228
- [9] G. Janeschitz, ITER JCT and HTs, J. Nucl. Mat. 290-293 (2001) 1-11
- [10] A. Leonard, A. Herrmann, K. Itami, J. Lingertat, A. Loarte, T. Osborne, W. Suttrop, J. Nucl. Mater. 266–269, 109 (1999).
- [11] Yu. Igitkhanov, O. Pogutse, H. Wilson, J. Connor, H. Wobig, P. Grigull, M. Hirsch, G. Janeschitz, Contributions to Plasma Physics, 42, Issue 2-4, p.272, 2002
- [12] N. Azakura, A. Loarte, G. Porter, V. Philipps, B. Lipschultz, A.Kallenbach, G. Matthews , "Studies of ELM Heat Load, SOL Flow and Carbon Erosion from Existing Tokamak Experiments and their Predictions to ITER", paper CT/P-01, IAEA-CN-1994
- [13] A.Loarte, G Saibene, R Sartori, D Campbell, M Becoulet, Plasma Phys. Control. Fusion 45 (2003) 1549–1569
- [14] R.A. Pitts, G. Arnoux, M. Beurskens, J. Nucl. Mat., 390-391, (2009), 755-759.
- [15] T. Eich, A. Herrmann, J. Neuhauser, R. Dux, J. C. Fuchs, S. Guenter, "Type-I ELM substructure on the divertor target plates in ASDEX Upgrade" Plasma Phys. Control. Fusion 47 (2005) 815–842
- [16] B. Bazylev, H.Wuerz// J. Nucl. Mater. 2002, v. 307-311, p. 69.
- [17] B. Bazylev et al// J. Nucl. Mater. 2005, v. 337-339, p. 766-770.
- [18] B. Bazylev. et al// Fusion Eng. Des. 2009, v. 84 Iss 2, p. 441.
- [19] B. Bazylev et al// J. Nucl. Mater. 2007, v. 363-365, p. 1011-1015.
- [20] B. Bazylev et al// J. Nucl. Mater. 2009, v. 386-388, p. 919-921
- [21] B. Bazylev et al// J. Nucl. Mater. 2011, v. 417, p. 655–658
- [22] B. Bazylev1, et al., 30th EPS Conference on Contr. Fusion and Plasma Phys., St. Petersburg, 7-11 July 2003 ECA Vol. 27A, P-2.44

- [23] J.W. Coenen et al// Nuclear Fusion 2011, v. 51, p. 083008
- [24] B. Bazylev et al// Physica Scripta 2011, v. T145, p. 014054
- [25] I.E. Garkusha et al// J. Nucl. Mater. 2007, v. 363-365, p. 1021
- [26] G. Sergienko et al// J. Nucl. Mater. 2007, v. 363-365, p. 96
- [27] S. Takamura et al// Contrib. Plasma Phys. 2004, v. 44, Nb. 1-3, p. 126
- [28] L.D. Landau, E.N. Lifshits/. Fluid Mechanics, Pergamon, New York, 1959.
- [29] H. Wuerz et al// Fusion Science and Technology 2001, v. 40, p. 191
- [30] W. Fundamenski, R. Pitts, Plas.Phys.Cont.Fus.48 (2006)109

2 Design Strategy for the PFC in DEMO Reactor

Yu. Igitkhanov, B. Bazylev and R. Fetzner

This work was presented on the 11th International Symposium on Fusion Nuclear Technology, Barcelona, September 16 2013, ICFRM-11, the paper N: FUSENGDES-D-13-00340 is submitted to the Fusion Engineering and Design.

Abstract. In this paper we analyze thermal performance of the DEMO plasma facing component (PFC) of W alloy mono-block design with Cu OFHC / EUROFER water coolant tube under steady-state and the transient edge localized modes (ELMs) loads during DEMO I and DEMO II operations. The expected ELMs characteristics in DEMO are estimated by extrapolating predictions found for ITER and by using the scaling arguments made from existing experiments (Igitkhanov, 2013). The W surface melting and evaporation due to the repetitive ELMs impact and effect of vapor shielding is numerically investigated by using the MEMOS code (Bazylev, 2002). The maximum temperatures in the interfaces between the materials as well as heat flux into the water coolant are calculated and compared with allowable temperature limitations of materials under neutron irradiation and the power water reactor (PWR) constrains. The feasibility of the PFC module design under DEMO heat loads is assessed.

2.1 Introduction

The performance of the plasma facing components (PFC) and materials in fusion reactor DEMO are fundamental issues affecting the ultimate technological and economic feasibility of fusion power. Many factors like excessive heat loads, transient plasma events and consequent erosion are limiting factors for the component lifetime. Our design strategy is to determine the structure of PFC module block, which maximize component lifetime against the life limitations.

In this paper we check the thermal performance of a W alloy mono-block module with water coolant tube suggested recently in [2] (Fig. 1) under steady-state and transient edge localized modes (ELMs) heat loads, expected in DEMOI and DEMOII operations. The coolant tube, imbedded into W, consists of the outer tube made from oxygen-free high thermal conductivity copper alloy (Cu OFHC) and EUROFER, as an inner tube of 6mm diameter. Geometrical parameters were optimized in [2] against thermo mechanical stresses for plasma power up to $10\text{MW}/\text{m}^2$. Here we analyze the applicability of this module under DEMO relevant transient loads within the temperature windows, allowable for the materials under neutron irradiation.

For DEMO, where several tens of dpa are expected on the PFCs, the selection and qualification of suitable materials is an issue. At present, W alloys (W-2%Re) are the primary refractory materials for the PFC in DEMO and is considered as an efficient heat diffuser due to a high thermal conductivity.

However, W features a very narrow operational temperature window which is limited by DBTT from below and by recrystallization and creep strength from above. In our study we assumed that the maximum W temperature must be between 500°C and 1300°C.

The oxide dispersion strengthened (ODS) stainless steel EUROFER ODS (9%Cr) is chosen as structural material with the high temperature creep resistance, particularly in the 'hot wall' operation. With regard to EUROFER, the minimum allowable temperature boundary is limited by high ductile to brittle transition temperature (DBTT) variation under irradiation ($\geq 300-350^\circ\text{C}$). The upper temperature boundary is suggested as $\sim 550^\circ\text{C}$ and is limited by creep strength.. The upper allowable temperature boundary for OFHC Cu is limited by the low thermal creep at temperatures above $\sim 0.5T_m$, where $T_m \sim 1356\text{K}$ is the melting point. Since the pipe is reinforced by the EUROFER inner tube, the Cu alloys could sustain the slightly higher temperatures. We suggest the operation window within 300°C and 650°C [2, 3].

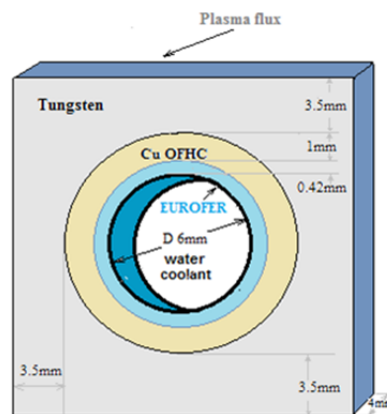


Fig. 1 DEMO PFC tungsten monoblock module with cooling channel made of the oxygen-free high thermal conductivity copper alloy Cu OFHC and EUROFER as a structural element. Geometrical parameters were optimized in [2] against thermo mechanical stresses for plasma power of 10MW/m^2 .

Since there is no reliable data of thermo mechanical properties under irradiation expected in DEMO, we, follow [2], assume 20% of degradation of thermal conductivity in Cu OFHC and 10% in EUROFER and W, which corresponds to irradiation of $\sim 5\text{dpa}$.

In this paper we use power loads data for the steady state DEMO operations found in the PROCESS code calculations [4] and the ELMs specifications and power loads to the FW and divertor found in [4] for the DEMO I and DEMO II designs. Then, the thermal and material response against the heat loads of repetitive ELMs is analyzed by considering the heat deposition and the material erosion by including the temperature dependent thermo-physical properties under neutron irradiation. The thermal analysis is performed with the code MEMOS [1] which has also the capability to account for tungsten evaporation with consequent screening effect and sub-cooled boiling at the coolant side. Finally, we discuss the effect of mitigated (like in ITER) ELMs and the efficiency of vapor shielding.

2.2 Power loading on the FW and divertor

In our calculation we use specification of power loads on the DEMO FW and divertor during a steady state operation without ELMs obtained in [4]. The heat loads to the FW include power in charged particles, CX neutrals and the electromagnetic radiation and are generally smaller than in divertor. Results for DEMO I and DEMO II designs are summarized in the Table I.

Table I

Steady state operation without ELMs	DEMO I divertor/FW	DEMO II divertor/FW
Power load, MW/m ²	5 / 0.5-1	8.9 / 1-5

Additional heat power loads due to the ELMs both to the FW and divertor have also be taken into account. In DEMO the Type I ELM characteristics were assessed based on ITER predictions and by using the scaling arguments derived from large-scale tokamaks data [5]. The ELM power fraction going to the FW was taken similar to that in ITER [6]. We assume that mitigated ELMs in DEMO will have like in ITER about 33 times reduced amplitude. Peak deposition energy to the FW and divertor plate as well as ELM frequency and ELM deposition time are summarized for DEMO I and DEMO II designs in the Table II.

Table II

ELM Type I characteristics	Uncontrolled ELM Divertor Divertor (DEMOI-DEMOII) / FW (DEMOI-DEMOII)	Controlled ELM Divertor (DEMOI-DEMOII) / FW (DEMOI-DEMOII)
ELM frequency, Hz	0.8-0.8/0.8-0.8	26-26/26-26
ELM deposition time, ms	1.2-1.2/0.6-0.6	1.2-1.2/0.6-0.6
Peak deposition energy, MJ/m ²	10-20/0.1-0.5	0.3-0.6/0.003-0.015

2.3 Steady state operation without ELMs

The maximum temperature of materials and the coolant tube temperature as a function of input power Q for the un-irradiated and irradiated cases are shown in Fig. 2 for the FW and in Fig. 3. for diveror. The horizontal lines indicate the low temperature limits for irradiated materials. The tube temperature corresponds to the minimum EUROFER temperature in interface with water coolant. Calculations show, that the W surface temperature remains well below the melting point both for the FW and divertor in DEMO I and DEMO II steady state operations without ELMs. The maximum material temperatures stay below upper allowable limits (not shown in graphs) for expected heat loads on the FW and divertor for both designs. For the DEMO I case the maximum temperatures of the FW materials are below the low limits, which indicates the overcooling under the PWR cooling conditions used here. The maximum temperatures can be shifted above the low boundaries by decreasing pressure drop and water velocity. For the DEMO II case the maximum temperatures of the FW materials remain below the low temperature boundaries up to a power load of about 4 MW/m^2 for EUROFER and 5 MW/m^2 for W.

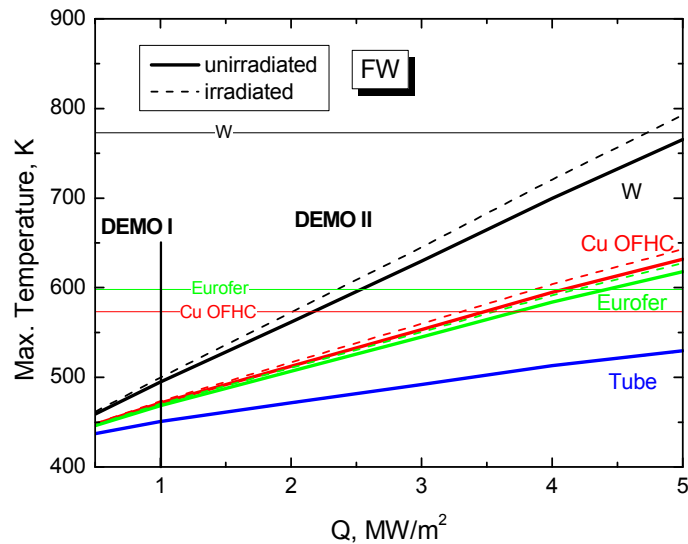


Fig. 2 Maximum temperature of materials vs. input power Q to the FW for un-irradiated and irradiated cases (dashed lines). Low boundaries are indicated by the horizontal lines. The upper limits are not shown.

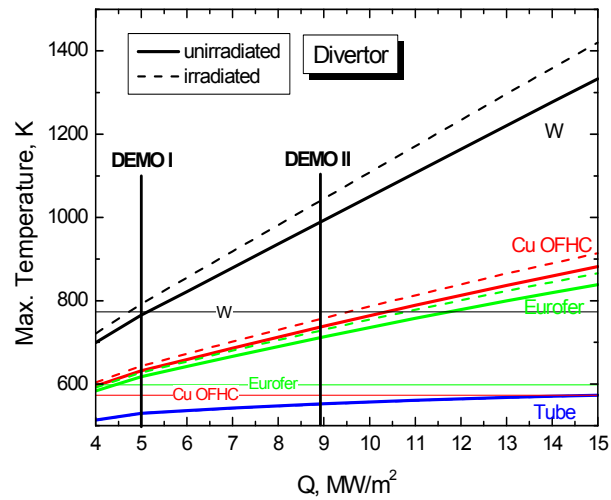


Fig. 3 Maximum temperature of materials vs. input power to the divertor for the un-irradiated and irradiated cases (dashed lines). Low boundaries are indicated by the horizontal lines. The upper limits are not shown.

For the divertor materials under DEMO I and DEMO II operation the maximum temperatures are above the low temperature limits. The PWR cooling conditions seems to be appropriate for these power loads. The critical heat flux (CHF) of 24MW/m^2 of PWR cooling is not exceeded [7].

2.4 Effect of unmitigated ELMs

Effect of uncontrolled ELMs on the FW is calculated for DEMO parameters under irradiation (see Table II). The evolution of maximum temperatures in the FW module materials is shown in Fig.4 for the advance DEMO II case, when the maximum heat loads to the wall are expected. Calculation show that under unmitigated repetitive ELMs heats loads and the PWR water cooling conditions the temperatures of the FW irradiated materials quickly saturate and remain within the operation temperature limits (for W between ELMs). The W surface does not melt. Therefore in both designs operations there will be no problems for the FW materials..

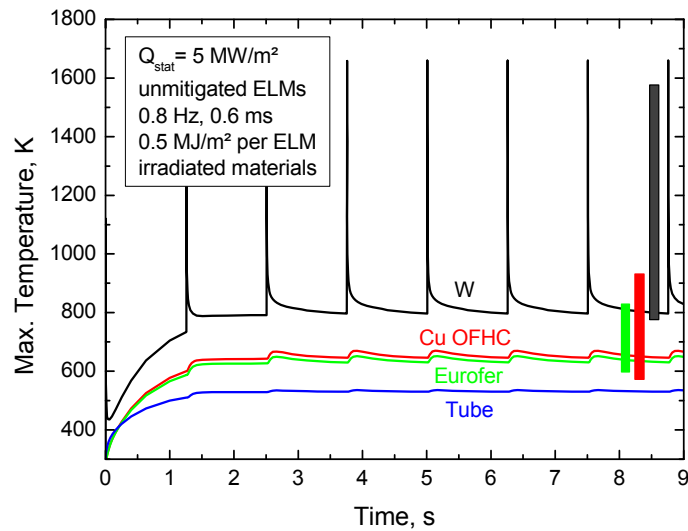


Fig 4. Evolution of maximum temperatures of the FW irradiated materials for DEMO II design heat power load $\sim 5 \text{ MW/m}^2$ and uncontrolled ELMs impact on the FW is shown. Color bars indicate allowable temperature ranges. Water coolant is in the PWR range.

The DEMO I divertor heat load of $5 \text{ MW/m}^2 + 0.8 \text{ Hz} \cdot 10 \text{ MJ/m}^2$ with unmitigated ELMs is considered and the evolution of maximum temperatures of irradiated materials and corresponding heat fluxes are shown in Fig.5 and 6. Fig. 7 and 8 show the same for DEMO II operation. Calculations show that the maximum temperature reaches $\sim 6000 \text{ K}$ at the ELM peaks (Fig. 5 and 7). In both cases W surface melts at the ELMs peaks and between ELMs the temperature is well below the melting point and W recrystallizes. The temperatures are also close to the low allowable limits. The melt depth is $\sim 50 \mu\text{m}$ and the melt lifetime $\sim 1 \text{ ms}$. Calculation shows that the W temperature between ELMs is only about 30K higher than for the un-irradiated case.

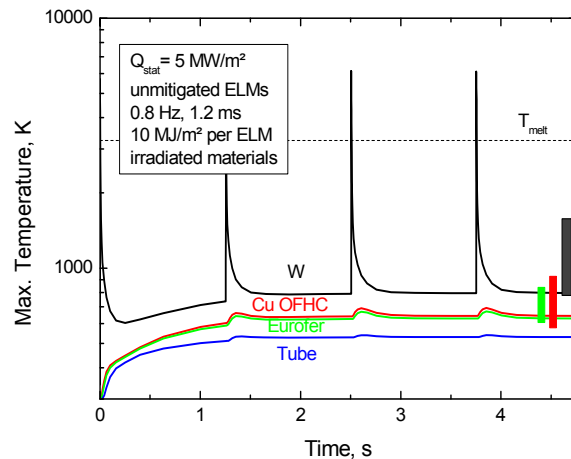


Fig 5. Evolution of maximum temperature of materials for uncontrolled ELMs impact on the divertor plate for the irradiated case is shown. The DEMO I divertor heat load is $\sim 5 \text{ MW/m}^2 + 0.8 \text{ Hz} \cdot 10 \text{ MJ/m}^2$.

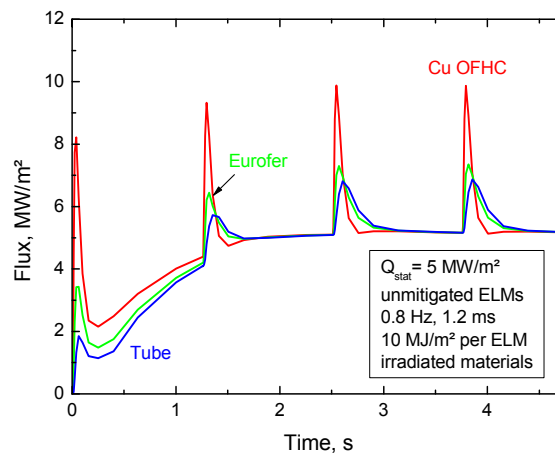


Fig 6. Evolution of heat fluxes for uncontrolled ELMs impact on the divertor plate for the irradiated case is shown. The DEMO I divertor heat load is $\sim 5 \text{ MW/m}^2 + 0.8 \text{ Hz} \cdot 10 \text{ MJ/m}^2$.

The evaporation of W reaches $\sim 0.6 \mu\text{m}$ per ELM, which could lead to W vapor cloud formation and to consequent shielding. The cloud could sweep radially off the point above the W surface due to diffusion. The time scale of the vapor removal, τ_{vap} , can be estimated from [8] and here is taken as 70 ms. This time is short enough to remove the vapor prior to the arrival of the next unmitigated ELM (1.2s), but long enough for the vapor to stay during each ELM (1.2 ms). Calculations for various τ_{vap} show that the result is almost independent of τ_{vap} in the range of 10-100ms. However, for $\tau_{\text{vap}} \sim 1\text{ms}$ and below (which corresponds to negligible screening) the lifetime of the W melt is longer and evaporation is enhanced.

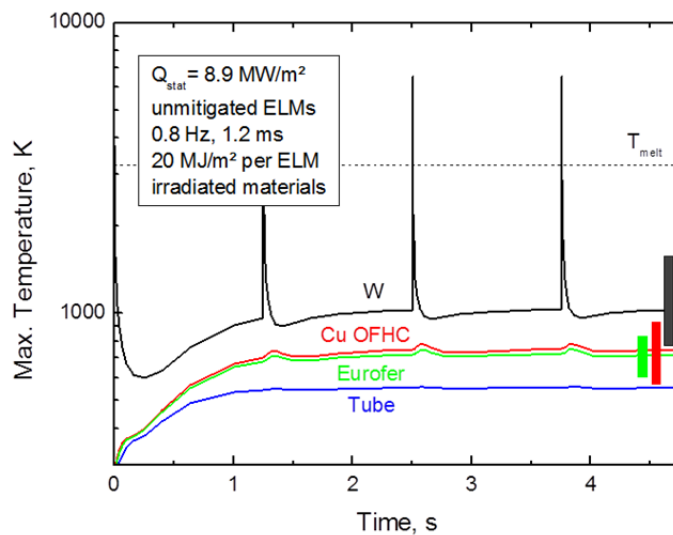


Fig 7. Evolution of maximum temperature of materials for unmitigated ELMs impact on the divertor plate for the irradiated case is shown. The DEMO II typical divertor heat load $8.9 \text{ MW/m}^2 + 0.8 \text{ Hz} \cdot 20 \text{ MJ/m}^2$ is considered.

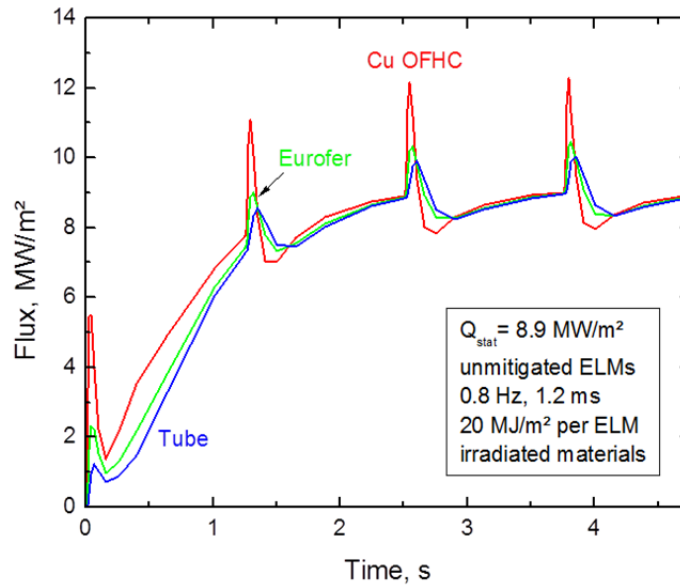


Fig 8. Evolution of heat fluxes for unmitigated ELMs impact on the divertor plate for the irradiated case is shown. The DEMO II typical divertor heat load $8.9\text{MW/m}^2 + 0.8\text{Hz} \cdot 20\text{MJ/m}^2$ is considered.

2.5 Effect of controlled ELMs

The Type I ELMs in DEMO probably can be mitigated by using a pace making pellet injection or by using a control coils like in ITER. Here we suggest that the reduced ELMs in DEMO will have like in ITER a thermal energy about ~ 33 times less than the uncontrolled ELMs (see Table II) [6]. First, the effect of mitigated ELMs on divertor plates for the DEMO I case is considered. Figs. 9 and 10 show evolution of the maximum temperatures and heat fluxes for irradiated materials, respectively. One can see that the W surface temperature quickly saturates and remains below the melting point, whereas the maximum EUROFER temperature is at the upper allowable limit. Heat flux to the water tube is less than critical (Fig. 10), so that water coolant remains within PWR range. In the case of advanced DEMO II operation the maximum temperatures of irradiated materials and corresponding heat fluxes are shown in Figs. 11 and 12. Compared to unmitigated ELMs, in the case of mitigated ELMs there is no melting and no evaporation of W. Therefore, there is also no vapor screening, which results in higher heat fluxes. After about 1.5s the heat flux at the tube exceeds the critical flux of 24MW/m^2 and water cooling fails both for the un-irradiated and irradiated cases [7]. Another consequence is higher material temperatures, which now exceed the allowable upper limits. This is particularly important for EUROFER, which as structural material can undergo creep deformation for long operating times.

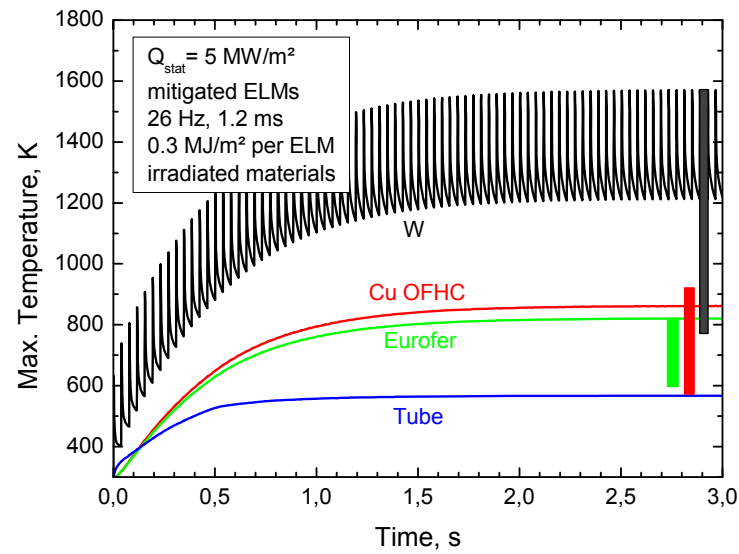


Fig 9. Evolution of maximum temperature of materials is shown for controlled ELMs impact. The DEMO I divertor heat load is $5\text{MW/m}^2 + 26\text{ Hz} \cdot 0.3\text{ MJ/m}$. Color bars show the allowable temperature limits.

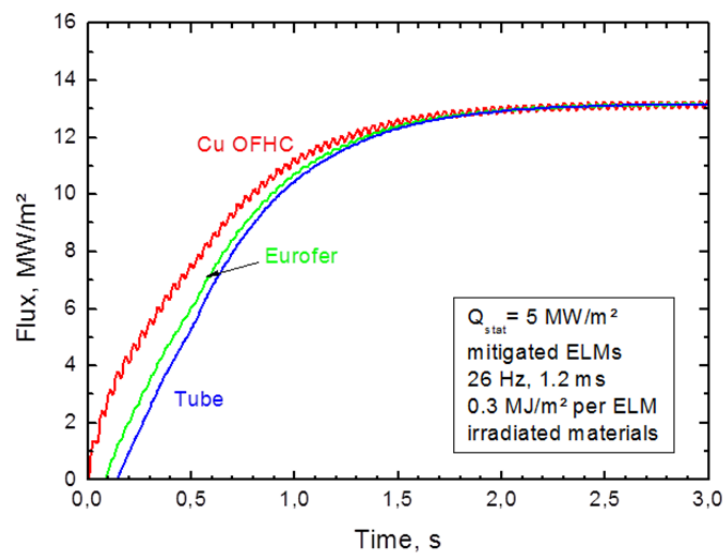


Fig 10. Evolution of heat flux to the materials is shown for the mitigated ELMs impact. The DEMO I divertor heat loads are $5\text{MW/m}^2 + 26\text{ Hz} \cdot 0.3\text{ MJ/m}^2$.

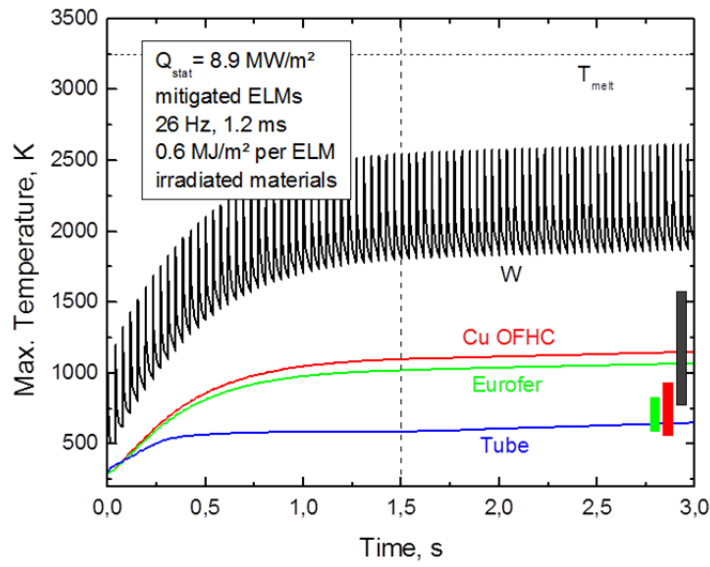


Fig 11. Evolution of maximum temperature of irradiated materials shown for mitigated ELMs The DEMO II divertor heat load is $8.9 \text{ MW/m}^2 + 26 \text{ Hz} \cdot 0.6 \text{ MJ/m}^2$. Critical flux to the coolant of 24 MW/m^2 is exceeded for operation time above 1.5s.

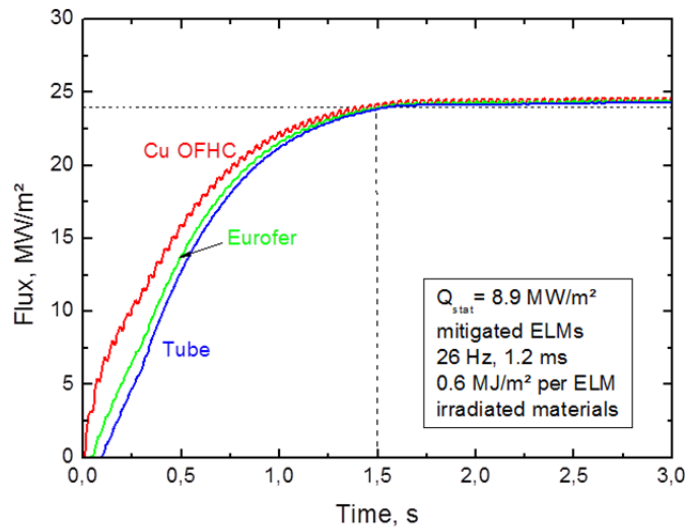


Fig 12. Evolution of heat flux to the materials is shown for controlled ELMs impact. The DEMO II divertor heat load is $8.9 \text{ MW/m}^2 + 26 \text{ Hz} \cdot 0.6 \text{ MJ/m}^2$. Critical flux to the coolant of 24 MW/m^2 is exceeded for operation time above 1.5s (dotted line)

2.6 Conclusions

We have performed thermo-hydraulic analyses of design concept of monoblock type water cooled DEMO PFC with Cu OHFC/EUROFER bound and the EUROFER as a structural material with 6 mm inner tube diameter, suggested in [2], where it was found suitable for incident heat fluxes up to 10MWm^{-2} . Detailed analyzes of the module for DEMO I and DEMO II steady state and the ELMs power loads show that:

1) During the steady state operation without ELMs the maximum temperatures of the FW and divertor modules stay below upper allowable limits for all materials. The W surface does not melt and the cracking at heat loads $\leq 5\text{MW/m}^2$ seems to be unexpected [8]. Unfortunately, the operating temperatures of the FW materials are below the allowable low limits and, for example, a severe embrittlement of W and EUROFER under neutron irradiation can be expected. This situation can be approved by operating at lower cooling efficiency.

2) For the FW, the unmitigated ELMs are tolerable for both DEMO I and DEMO II design operations. In the divertor, the maximum allowable W temperature between the ELMs is within the limits, but at the ELM peaks it considerably exceeds the melting temperature. Therefore, the W surface melts and evaporates during the ELM peaks and between the ELMs W recrystallization occurs. The maximum EUROFER and Cu alloy temperatures remain within the operation limits. However, the minimum EUROFER (tube) temperature remains below the low limit and could in time experience embrittlement failure. Evaporation of W and vapor shielding keeps the material temperatures saturated during the repetitive ELMs impact. The water cooling remains within the PWR range.

3) Mitigation of ELMs results in reduced W peak temperatures as expected. Melting does not occur, not even in the divertor of DEMO II operation. However, because of the absence of evaporation, the vapor screening effect is lost. Therefore, the power flux to the module effectively is increased, although the amplitude of individual ELMs is reduced. As a consequence, the temperatures of all materials are above the allowable ranges. To improve the situation, a more efficient cooling is required, which cannot be achieved within the PWR cooling conditions.

4) We considered the case when the water cooling temperature and pressure remains within the pressurized water reactor (PWR) range. For 6 mm inner pipe diameter, considered here, input temperature and pressure were chosen to meet the EUROFER temperature limits. Input hydraulic parameters as, $T_{in}=325^{\circ}\text{C}$ and $P_{in}=15.5\text{MPa}$ have been chosen. To guarantee a reasonable margin to the critical heat flux and maximum pressure drop the water velocity of 20m/s is required. In the case of the FW, these conditions lead to overcooling of the module, whereas for the divertor in case of mitigated ELMs the heat flux reaches the critical value of 24MW/m^2 and the so-called supercritical water stage could occur.

5) The geometry of the module, considered here is not optimized for expected in DEMO transient heat loads. One way of having the temperatures within the recommended operating windows could be an

adjustment of material thickness. The change in geometry will, however require of performing a self-consistent thermo-mechanical analysis.

Acknowledgments

This work, supported by the European Communities under the EFDA Task Agreement WP10-PWI between EURATOM and Karlsruhe Institute of Technology, was carried out within the framework of the European Fusion Development Agreement. The views and opinions expressed herein do not necessarily reflect those of the European Commission. The authors thank Dr. J. Aktaa for pointing our attention to the PFC module, considered above.

2.7 References

- [1] B. Bazylev et.al, J. Nucl. Mat. 307-311, 69, 2002
- [2] A.Li Puma, M. Richou EFDA_D_2LARJJ, v.1.1, Report for TA WP12-DAS-02
- [3] S.Zinkle, N.Ghoniem, Fus.Eng. and Des.,51-52, 2000, 55
- [4] DEMO Design Summary, EFDA_D_2L2F7V v1.0, 2012S.
- [5] Yu. Igitkhanov and B. Bazylev, SOFT 2012, paper submitted to the IEEE Transactions on Plasma Science
- [6] M.Shimada, M. Loughlin, M. Shute, Heat and Nuclear Load Specifications for ITER, ITER_D_2LULDH v2.3, 2009
- [7] G. Federichi,,R. Raffray, J. Nucl. Mat.,244,1997 101
- [8] S. Pestchanyi, I. Garkush, I. Landman, Fusion Engineering and Design 86 (2011) 1681-1684.
- [9] S. Pestchanyi, I. Landman, Simplified model for carbon plasma production by ELM in ITER, EPS 2008, Cret

3 Effect of Thermal Loads on Different Modules of DEMO PFC

Yu. Igitkhanov, R. Fetzner, B. Bazylev and L. Boccaccini (INR Karlsruhe)

This work was presented on the 16th International Conference on Fusion Reactor Materials ICFRM-16, in October 20-26, 2013 Beijing, China (paper number FST13-732), and is submitted to the Fusion Engineering and Design

Abstract. The thermal performance of different modules of plasma facing components (PFC) is analyzed for the DEMO reactor conditions in steady-state operation with the inclusion of the transient edge localized modes (ELMs) for mitigated and un-mitigated cases. As an example the effect of these loads is considered for the W alloy mono-block design with Cu OFHC/EUROFER water coolant tube first proposed in the framework of the PPP&T divertor study. A variant of this design with EUROFER tube connected to the W block with a diamond/copper composite (DCC) used in the diagnostic windows, is also analysed. A design goal is to find the optimal thicknesses of material layers, which allow one to keep the maximum temperatures within the allowable design limits under ITER water cooling conditions. Heat transfer and armor erosion due to the plasma impact has been modeled by using the MEMOS code.

3.1 Introduction

In this paper we investigate the effect of ELMs thermal loading on existing design of water cooled divertors that have been first proposed in the frame of the EU PPP&T studies. In particular two designs are analyzed: they are monoblock concepts with W blocks and EUROFER coolant tubes. One of this use oxygen-free high thermal conductivity copper alloy (Cu OFHC) as interlayer between W and EUROFER [2] (see Fig. 1), the second use instead a one made from reinforced diamond/copper composite (DCC) and EUROFER as a structural material (see Fig. 2) as proposed in some diagnostic windows designs. Also the proposed in [2] designs refer to divertor, we considered the applicability of both modules also for the first wall (FW) blanket conditions. We analyze the behavior of these modules under DEMO relevant ELMs thermal loading and estimate the optimal thicknesses of material components which allow operation within the temperature range acceptable for the materials under neutron irradiation and under the pressurized water reactor (PWR) cooling conditions adopted in both concepts.

For DEMO, where several tens of dpa under neutron irradiation are expected on the PFCs, the selection and qualification of suitable materials is an issue. At present, W alloys are the primary refractory materials for the PFC in DEMO and are considered as an efficient heat diffuser due to a high thermal conductivity. However, W features a very narrow operational temperature window which is limited by the ductile to brittle transition temperature (DBTT) from below and by recrystallization and creep

strength from above. In our study we assumed that W temperature operating window is between 500°C and 1300°C [2].

With regard to EUROFER, the minimum allowable temperature is limited by the DBTT under irradiation (≥ 300 -350°C). The upper temperature boundary is suggested as ~ 550 °C and is limited by creep strength. The operation window for EUROFER temperature is assumed between 300°C and 550°C [2].

The upper allowable temperature boundary for Cu OFHC is limited by the low thermal creep at temperatures above $\sim 0.5T_m$, where $T_m \sim 1356$ K is the melting point. Since the coolant pressure withstands by the EUROFER pipe, the Cu alloy is a compliant layer and could sustain slightly higher temperatures. We assume the operation window for Cu OFHC between 300°C and 650°C as reported in [2, 3]. Since there is no reliable data of thermo mechanical properties under irradiation expected in DEMO, we, following [2], assume 20% of degradation of thermal conductivity in Cu OFHC and 10% in EUROFER and W, which corresponds to irradiation of ~ 5 dpa. Unfortunately, for DCC under irradiation there are no reliable data in literature.

As far as the power loads in DEMO operations concerns, we use the data found in the PROCESS code calculations [4] and the ELMs specifications and power loads to the FW blanket and divertor found in [5] for the DEMO I and DEMO II configuration designs. Then, the thermal and material response against the power loads of repetitive ELMs is analyzed by considering the heat deposition and the material erosion. The temperature dependent thermo-physical properties under neutron irradiation are included. The thermal analysis is performed with the code MEMOS [1] which has also the capability to account for tungsten evaporation with consequent screening effect and sub-cooled boiling at the coolant side. Finally, we discuss the relative performance of these modules and importance of material screening due to W vaporization.

3.2 Power loading on the FW and divertor

In our calculation we use the specifications of power loads on the DEMO FW and divertor during a steady state operation with and without ELMs obtained in [4]. The power load on the FW in the DEMO I case is 0.5-1MW MW/m² and for DEMO II is estimated as 1-5MW/m². For divertor, heat loads are about 3MW/m² and about 8.9MW/m² for the DEMO I and the DEMO II cases, respectively [4]. The expected characteristics of Type I ELMs in DEMO are estimated in [5, 6]. The ELM power fraction going to the FW was taken similar to that in ITER [7] and the mitigated ELMs have like in ITER about 33 times reduced amplitude. In the case of DEMO I the uncontrolled ELM frequency is estimated as 0.8Hz, peak deposition energy/deposition time to the FW and divertor plate are 0.1MJ/m²/0.6ms and 10MJ/m²/1.2ms, respectively. In the case of DEMO II peak deposition energy/deposition time to the FW and divertor plate are 0.5MJ/m²/0.6ms and 20MJ/m²/1.2ms, respectively [5,6]. The full power deposition consists of the sum of the steady state and the ELMs power loads.

Pressurized water reactor (PWR) cooling conditions with about 150°C inlet water temperatures and pressure about 15,5MPa are used for the calculations. These conditions are similar to ITER and that for

6mm inner diameter concept discussed in [2], where a swirl of 0.8mm thickness and twist ratio of 2 are assumed to increase the heat removal capabilities. The water velocity about 20 m/s guarantees a reasonable margin to the critical heat flux without excessive pressure drops. The water temperature increase and pressure drop along the pipe has been calculated in MEMOS depending on deposited into coolant power. Heat exchange coefficient is calculated using Sieder-Tate correlation for forced convection regime and Thom correlation for sub-cooled boiling regime (see references in [2]). The tube temperature profile almost linearly increases with power deposited into coolant and slightly “bends” at 5MW/m^2 , where the transition from convective to sub-boiling regime occurs. The maximum value of calculated critical heat flux (CHF) is about 18MW/m^2 .

3.3 W monoblock module with CuOFHC / EUROFER water coolant tube

The W/Cu OFHC monoblock and its geometrical parameters suggested in [2] are optimized against thermo mechanical stresses for steady state plasma thermal power up to 10MW/m^2 . The behavior of this module under DEMO relevant transient loads within the temperature windows allowable for the materials under neutron irradiation has been considered in [6] and the further optimization accounting for the ELMs loading is suggested. In this paper it is shown that even for the advanced DEMO II operation with repetitive ELMs the temperatures of the FW irradiated materials quickly saturate and remain within the operation temperature limits. Therefore the ELMs pose no threat to the FW of the DEMO I and DEMO II cases [6]. As far as the divertor concerns, in both cases the W surface melts at the ELMs peaks positions, remaining well below the melting point between the ELMs. However, under the PWR cooling conditions the maximum temperatures are close to the low allowable limits. Calculation shows that for irradiated ($\sim 5\text{dpa}$) materials the W temperature between ELMs is about of 30K higher than for un-irradiated materials. The evaporation of W at the ELMs peak impact reaches $\sim 0.6\ \mu\text{m}$ per ELM and the melt depth is about $50\ \mu\text{m}$ during the melt lifetime $\sim 1\text{ms}$. This could lead to W vapor cloud formation and to consequent power shielding effect, protecting the wall from erosion. However, the cloud could be swept radially away due to the radial diffusion. The time scale of the vapor removal, τ_{vap} , can be estimated from [8] and here is assumed as 70 ms. This time is short enough to remove the vapor prior to the arrival of the next unmitigated ELM (1.2s), but long enough for the vapor to stay during each ELM (1.2 ms). Calculations for various τ_{vap} show that the result is almost independent of τ_{vap} in the range of 10-100ms. However, for $\tau_{\text{vap}} \sim 1\text{ms}$ and below, which is comparable with the ELM deposition time, the vapor cloud remains rare and cannot screen efficiently. This results in a longer lifetime of the W melt and in enhanced evaporation.

It is shown that for mitigated ELMs in DEMO I divertor the maximum temperatures for irradiated materials remain below the melting point, whereas the maximum EUROFER temperature is slightly above the upper allowable limit [6]. Heat flux at the water tube is less than critical and the water coolant remains within the PWR range. In the case of advanced DEMO II operation the maximum temperatures of irradiated divertor materials are shown in Fig. 3. In this case water cooling within the

PWR cooling range fails. After about 1s, the heat flux at the tube exceeds 18MW/m^2 , which is critical for PWR operation [9], both for the un-irradiated and irradiated cases. After cooling failure, the temperatures of all materials increase continuously. Water cooling failure is observed only in the case of mitigated ELMs in advanced DEMO II divertor operation, but not for unmitigated ELMs. The reason is the effect of vapour screening, which is negligible in the case of mitigated ELMs. The importance of vapour shielding is further explored using the example of transient DEMO II divertor heat loads. A substantial difference in W erosion occurs with and without vapour screening, see Fig. 4, where the evaporation of the W surface is compared for two cases: with and without vapour cloud effect. The case without vapour screening corresponds to the situation where vapour is removed from the space above the PFC module on a time scale much faster than the ELM deposition time, and no dense vapour cloud is formed.

The temperature evolution during the repetitive ELMs impact is shown in Fig. 5. A considerable effect on the temperature is seen with and without screening with higher temperatures obtained when screening is not effective. In the case of mitigated ELMs even higher temperatures are achieved because neither W evaporation (evaporation cooling) nor vapour screening occur.

Fig. 6 summarizes the heat flux to the coolant tube. For unmitigated ELMs, the average heat flux of about 15MW/m^2 in the case without vapour shielding is reduced by the screening effect to values below 10MW/m^2 . For mitigated ELMs, where no evaporation occurs, practically the entire heat delivered to the PFC module surface is finally removed via the coolant. Thus, only in the case of mitigated ELMs, the critical heat flux of the PWR cooling range is reached.

3.4 W monoblock module with DCC/EUROFER water coolant tube

The second design with diamond and copper (DCC) is for the first time considered in this paper. This material is characterized by higher thermal conductivity and by thermal expansion coefficient which can be tailored accordingly to minimize thermal stresses with adjacent materials [8]. The thermal conductivity of unirradiated DCC is a function of the thermal conductivities of the diamond particles and the copper matrix, the volume fraction of each component, and also of the diamond particle sizes. The thermal conductivities of composites are about 600W/m K for $90\text{-}110\mu\text{m}$ diamond particle size and for $\sim 65\%$ of volume fraction of diamonds in the composite [8]. We assume this value in our calculations.

Because of high thermal conductivity of DCC the maximum temperature of materials and the coolant tube remain insensitive to the DCC thickness variation and lie within the allowable temperature range for W. For the DCC a thickness of 1.0mm is chosen as the reference case.

The dependence of the maximum material temperatures on the EUROFER thickness at given W thickness $\Delta_w=3\text{mm}$ shows that in the range of $\Delta_{\text{EUROFER}}=0.1\text{-}0.5\text{mm}$ the temperatures remain within allowable temperature windows (shown as colored vertical bars) (see Fig. 7). Calculations also show that the variation of W thickness affects only the W temperature (Fig. 8).

For the reference case we choose $\Delta_{\text{Eurofer}}=0.4\text{mm}$ (that is compatible with the [6] structural design) and $\Delta_w=3\text{mm}$. The variation of maximum material temperatures with input plasma power in the range of heat flux from 1 to 10 MW/m^2 is shown in Fig. 9. Calculations are done for steady state operation in DEMO I with heat flux to the FW in the range 0.5-1 MW/m^2 and to the divertor 5 MW/m^2 . Advanced DEMO II operation with heat fluxes to the FW in the range 1-5 MW/m^2 and to the divertor 8.9 MW/m^2 is considered.

It is seen that for the irradiated case ($\sim 5\text{dpa}$) the temperatures are slightly above the un-irradiated case, but still remain in the allowable range for the divertor case. However, the cooling conditions used in the calculations lead to overcooling of the first wall. It becomes clear that the cooling condition can be relaxed to operate at somewhat higher wall temperatures required for safe reactor operations.

The effect of unmitigated ELMs heat loads on the W/DCC module temperatures is shown in Fig. 10 for advanced DEMO II operation. The temperatures are similar to the case of W/Cu OFHC shown in [6]. During ELM peaks, melting and evaporation of W occurs. About $0.7\mu\text{m}$ of the W surface are evaporated per ELM. Between ELMs, the temperatures are slightly below the allowable range in DEMO I operation (not shown) and within the allowable temperature range for DEMO II.

It must be noted, that under neutron irradiation in a nuclear reactor the diamond-graphite transition could in principle occur in DCC. The transition time depends on irradiation temperature and at higher temperatures $\geq 750^\circ\text{K}$ it increases with decreasing temperature but remains shorter than in the absence of irradiation.

3.5 Conclusion

We have performed thermo-hydraulic analyses of design concepts of monoblock type water cooled DEMO PFC module with Cu OFHC/EUROFER tube, first suggested in [2], and the W monoblock module with embedded DCC/EUROFER water pipe. Detailed analyses for DEMO I and DEMO II under steady state operation and operation with the ELMs power loads shows:

- 1) For the PFC W module with reinforced DCC/EUROFER tube, steady state DEMO I and advanced DEMO II operation without ELMs results in maximum temperatures of the FW and divertor modules below the upper allowable limits for all materials with layer thicknesses $\Delta_w=3.0\text{ mm}$, $\Delta_{\text{DCC}}=1.0\text{ mm}$, and $\Delta_{\text{EUROFER}}=0.4\text{ mm}$.
- 2) For DEMO operation with unmitigated ELMs, for the divertor modules, the maximum allowable W temperature between the ELMs is within the allowable limits, but at the ELM peaks considerably exceeds the melting temperature. Therefore, the W surface melts and evaporates during the ELM peaks and between the ELMs W recrystallization occurs. Nevertheless, the maximum of EUROFER, DCC and Cu alloy temperatures remain within the operation limits.
- 3) In the case of unmitigated ELMs, evaporation of W and consequent vapor shielding keeps the heat flux to the PFC materials and coolant tube limited. This heat flux reduction does not occur in the case of

mitigated ELMs. Due to the reduced ELM amplitude, no melting and no evaporation occur. This beneficial effect of mitigation, however, is accompanied by a large heat flux at the coolant tube, which for DEMO II divertor operation exceeds the critical heat flux for PWR cooling range.

Acknowledgment

This work, supported by the European Communities under the EFDA Task Agreement WP10-PWI between EURATOM and Karlsruhe Institute of Technology, was carried out within the framework of the European Fusion Development Agreement. The views and opinions expressed herein do not necessarily reflect those of the European Commission.

3.6 References

- [1] B.N. BAZYLEV et.al, J. Nucl. Mat. 307-311, 69, 2002
- [2] A.LI PUMA, M. RICHOU EFDA_D_2LARJJ, v.1.1, Report for TA WP12-DAS-02.
- [3]. S.ZINKLE, N.GHONIEM, Fus.Eng. and Des.,51-52, 2000
- [4] DEMO DESIGN SUMMARY, EFDA_D_2L2F7V v1.0, 2012S.
- [5] YU. IGITKHANOV and B. BAZYLEV, SOFE 2013, paper submitted to the IEEE Transactions on Plasma Science
- [6] YU. IGITKHANOV et.al., ISFNT-11, 2013, paper submitted to the Fus.Eng. and Des.
- [7] M.SHIMAD, M. LOUGHLIN, M. SHUTE, Heat and Nuclear Load Specifications for ITER, ITER_D_2LULDH v2.3,2009
- [8] K. YOSHIDA, H. MORIGAM / Microelectronics Reliability 44 (2004) 303–308
- [9] G. FEDERICHI, R. RAFFRAY, J. Nucl. Mat.,244,1997 101

Figure Caption

Fig. 1 DEMO PFC tungsten monoblock module with cooling channel made of Cu OFHC and EUROFER. Geometrical parameters were optimized in [2] against thermo mechanical stresses for plasma power of $10\text{MW}/\text{m}^2$.

Fig. 2 DEMO PFC water coolant module with DCC/EUROFER tube imbedded into W alloy as a plasma facing material.

Fig. 3 Evolution of maximum temperature of irradiated materials shown for mitigated ELMs. The DEMO II divertor heat load is $8.9\text{MW}/\text{m}^2 + 26\text{Hz} \cdot 0.6\text{MJ}/\text{m}^2$. Critical flux to the coolant of $24\text{MW}/\text{m}^2$ is exceeded for operation time above 1.5s. The vertical bars mark the allowable temperature range of the respective materials.

Fig. 4 Evaporation of W surface in the case of DEMO II unmitigated ELMs taking into account the effect of vapor screening versus the situation without vapor screening.

Fig. 5 The maximum (green) and minimum (blue) EUROFER temperatures (at the tube) for DEMO II divertor heat loads for unmitigated ELMs with and without vapor screening and for mitigated ELMs (dashed lines).

Fig. 6 Heat flux to tube for DEMO II divertor heat loads for unmitigated ELMs with and without vapor screening and for mitigated ELMs.

Fig. 7 Maximum temperature of materials and the coolant tube as a function of EUROFER thickness Δ_{Eurofer} for advanced DEMO II operation. W and DCC thicknesses are fixed. The black and green bar, respectively, marks the range of allowable temperature for W and EUROFER.

Fig. 8 Maximum temperature of materials and the coolant tube as a function of tungsten thickness Δ_{W} for advanced DEMO II operation. DCC and EUROFER thicknesses are fixed.

Fig. 9 Maximum temperatures of materials and the coolant tube as a function of input plasma power Q to the first wall (FW) and divertor of DEMO I and DEMO II operation for the irradiated (solid lines) and un-irradiated case (dashed lines). The change of the temperature slope seen in figure occurs due to the change of water cooling regime from a convective free to sub-cooling at $5\text{MW}/\text{m}^2$.

Fig. 10 Maximum temperatures in W/DCC module for DEMO II divertor heat load of $8.9\text{MW}/\text{m}^2 + 0.8\text{Hz} \cdot 20\text{MJ}/\text{m}^2$ with unmitigated ELMs for the irradiated case.

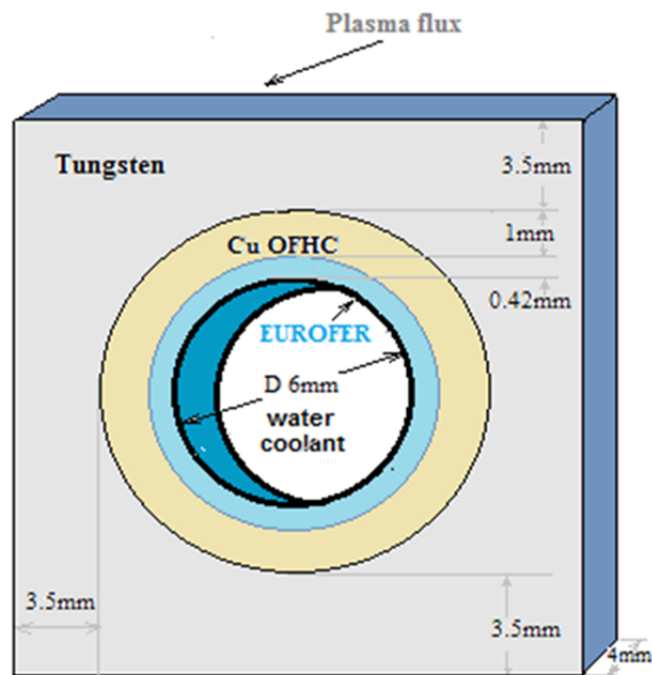


Fig. 1.

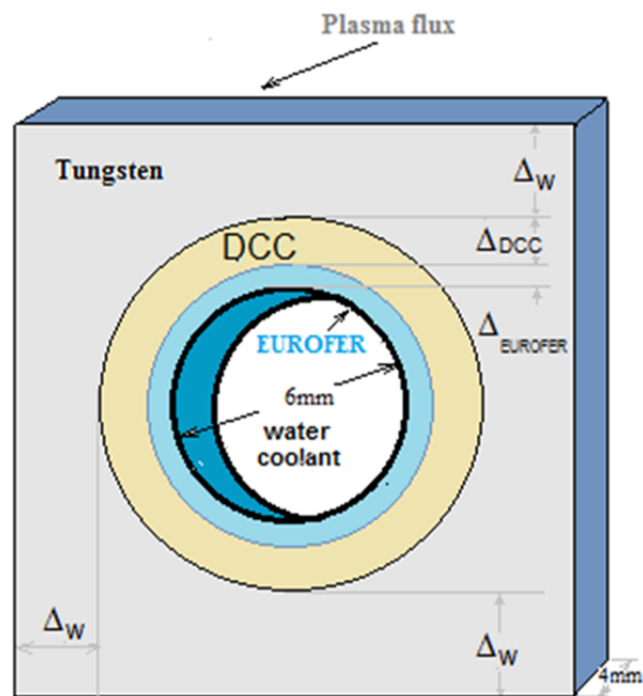


Fig. 2.

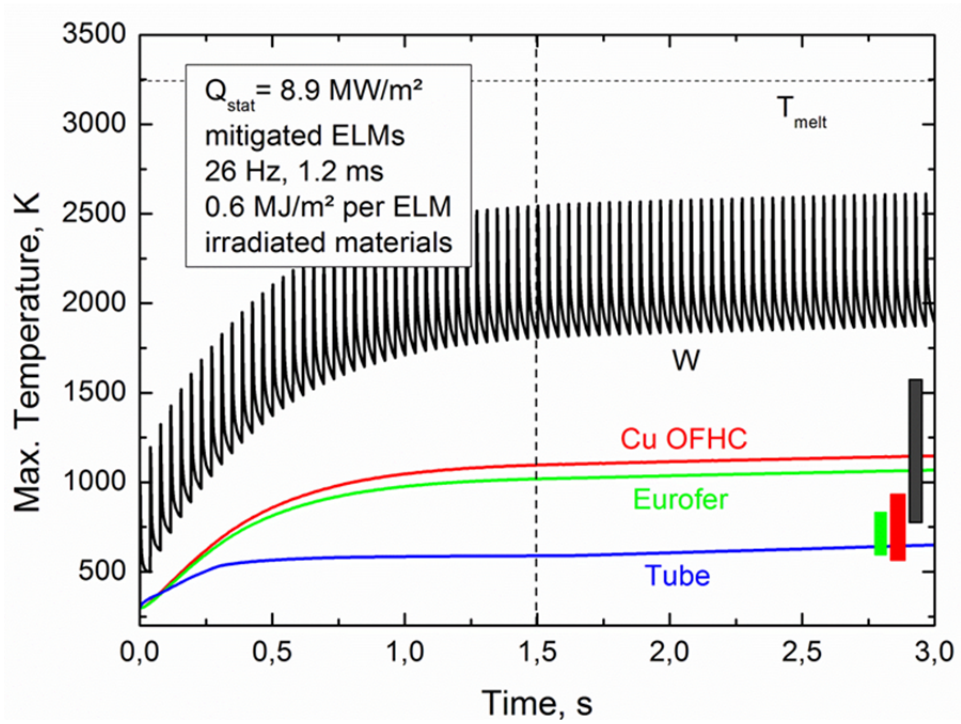


Fig. 3.

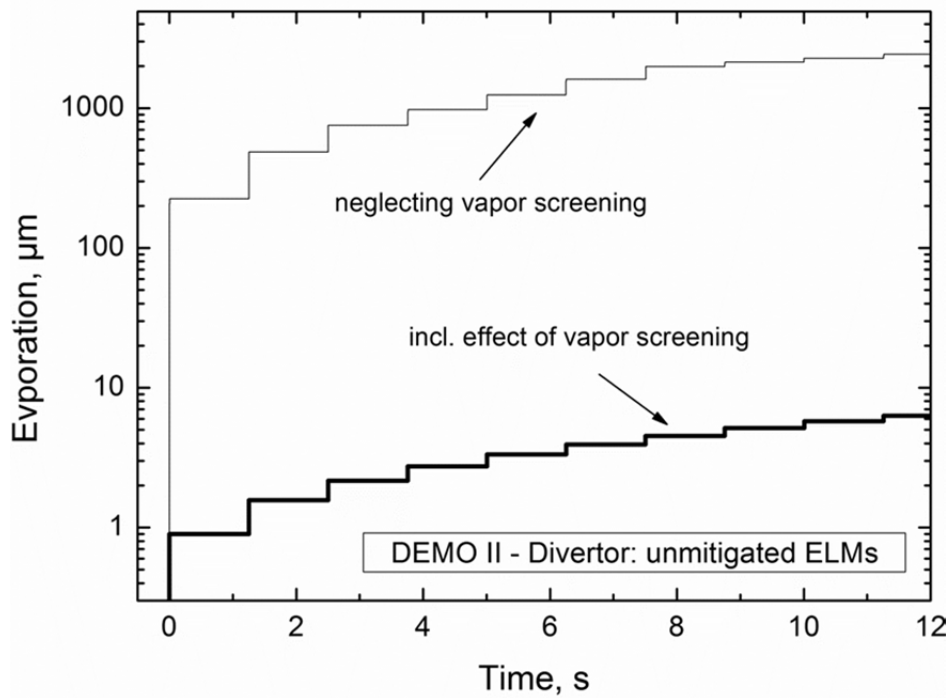


Fig.4

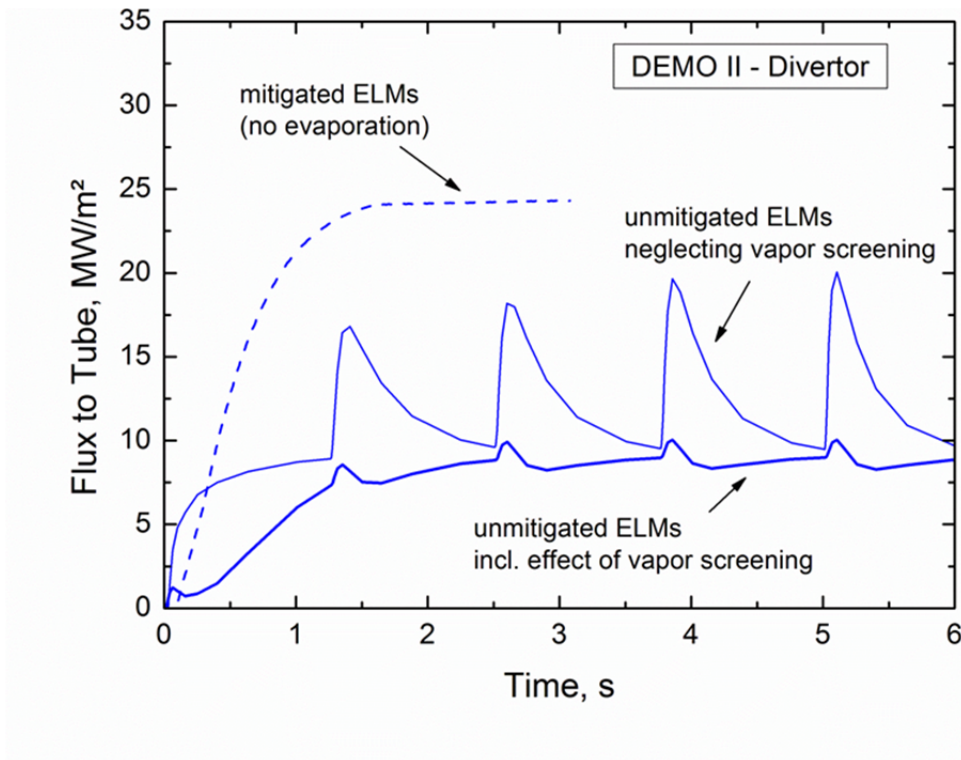


Fig 5.

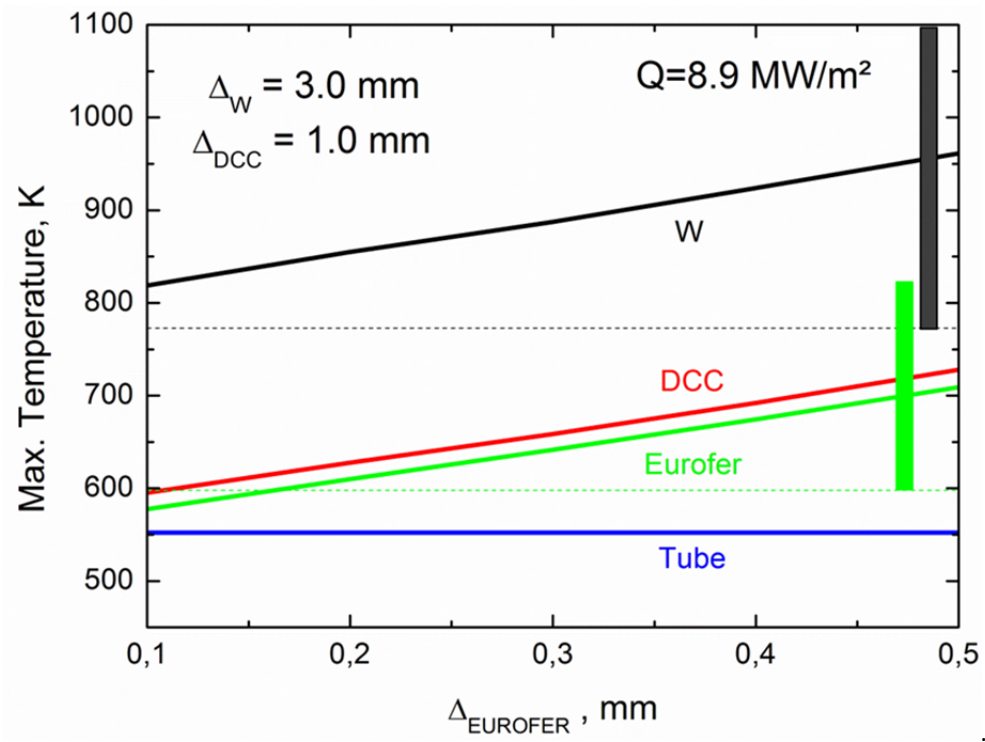


Fig. 6.

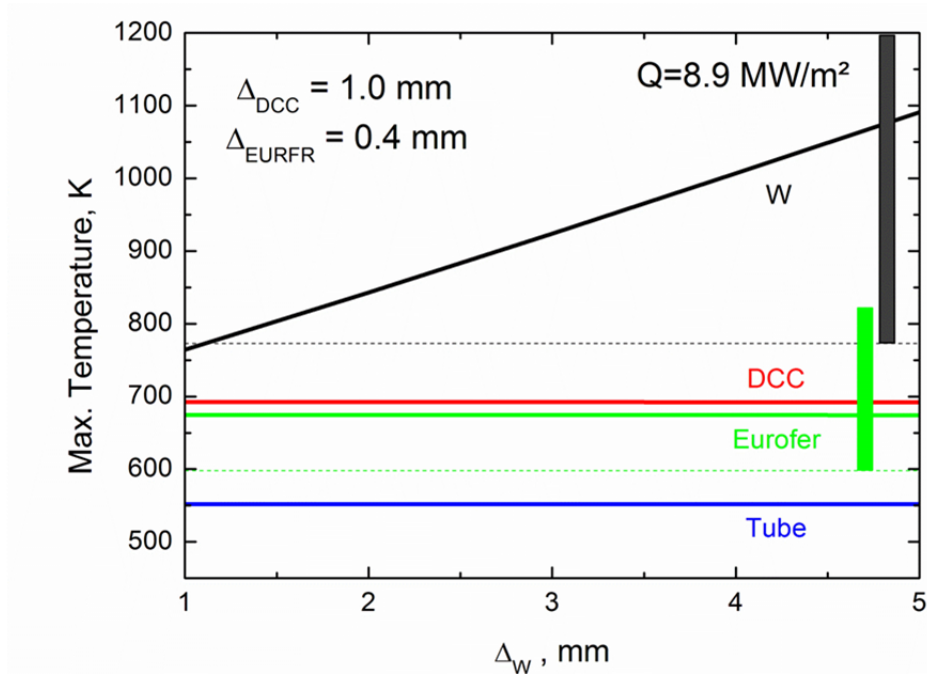


Fig. 7

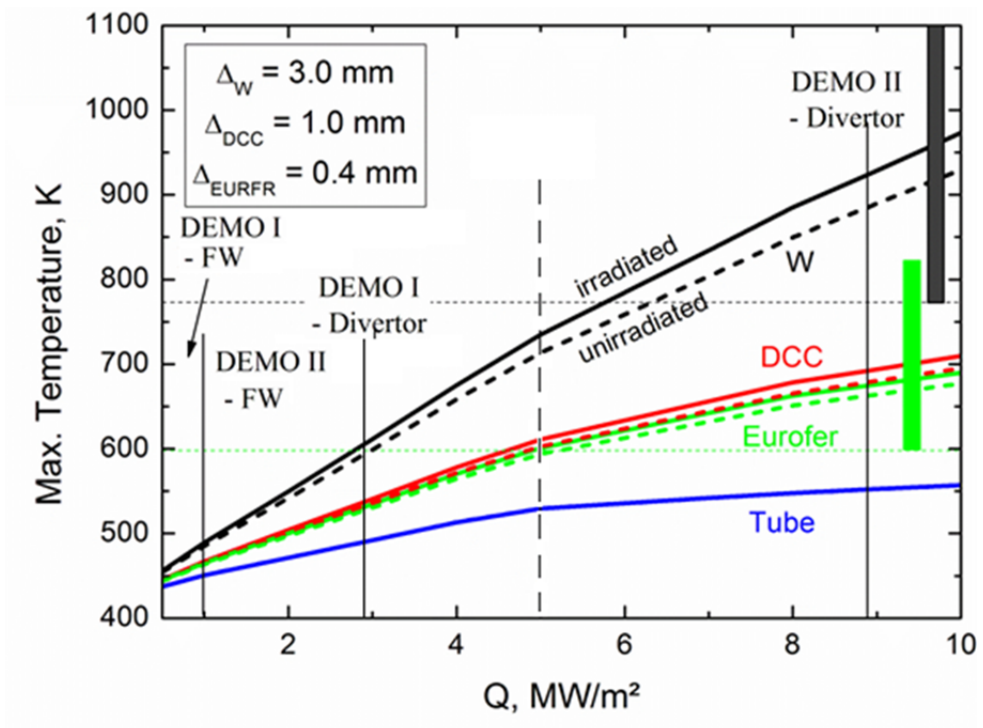


Fig. 8

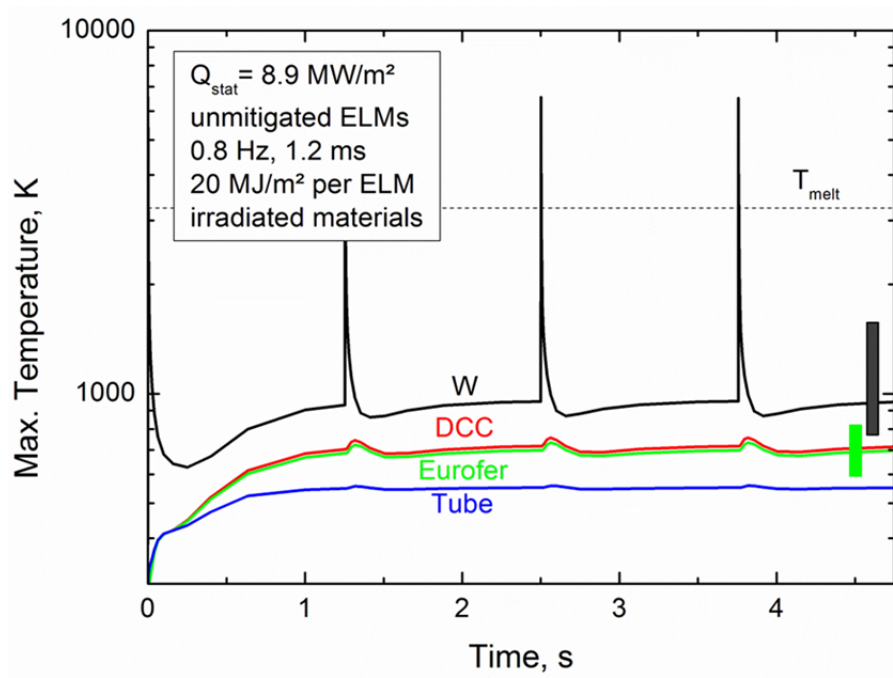


Fig. 9

4 Conversion of magnetic energy of runaway electrons during disruption termination

Yu. Igitkhanov

This work was presented on the 14th International Workshop on Plasma Edge Theory in Fusion Devices 23-25, 09, 2013 Cracow, Poland; the paper is published in "Contributions to Plasma Physics" 54, o.4-6, 585-590 (2014).

Abstract. A substantial portion of poloidal magnetic energy stored in the RE beam could dissipate in the first wall (FW) armour due to ohmic dissipation of inductive current. Relatively small part of magnetic energy can also be converted into heat during a direct impact of the RE beam on the FW due to the ohmic dissipation of a return current, induced by penetration of the RE beam into a metal in the skin time scale. The observed increase of temperature at a spot on the JET dump plate upon increasing the RE current can be explained by assuming that 50% of the RE energy, predominantly magnetic energy, is converted into heat. Calculations of the RE stopping power (SP) onto the ITER FW Be bulk armour predict strong erosion. While the threshold energy for beryllium melting is about $5\text{MJ}/\text{m}^2$, the RE heat deposition is expected to be almost twice as large.

4.1 Introduction

Runaway electrons (RE) cause significant localised damage of in-vessel components in present devices (see for instance [1]). They can pose a considerable threat to plasma facing components (PFC) in future fusion reactors by depositing their energy to the first wall (FW). In this paper we consider the case when RE impinging the tungsten armor, which is the most probable candidate for the FW as a refractory material. The correct evaluation deposited energy is important for assessment of surface erosion and plasma contamination. Usually, the evaluation of stopping power takes into account only the kinetic energy of impinging electrons. Here we consider the mechanism of inductive losses of the RE beam in tungsten armor. When an RE beam intersects a tungsten surface, the beam space charge within a metal is effectively neutralized by a redistribution of the free electrons of the metal with the characteristic time $\sim 1/\omega_p \sim 10^{-16}$ sec, where the plasma frequency of tungsten ω_p is $\sim 9.74 \cdot 10^{15} \text{ sec}^{-1}$ and the effective electron mass $m_{e,\text{eff}} \sim 2-3m_e$. This time is typically quite short, so that net space charge does not limit the RE penetration in a metal. The RE current I_{RE} will induce a return ohmic current I of free electrons in tungsten, which acts to neutralize the magnetic field of the RE, so that $I_{\text{RE}} \sim -I$ during short time and if $\lambda_E/a \ll 1$ (where a is the RE beam radius, $\lambda_E \sim c/\omega_p \sim 3 \mu\text{m}$ is the electron skin length). The ohmic dissipation of plasma current and a drag between the RE beam and the induced electric field eventually converts the RE magnetic energy into heat. The ratio of the magnetic energy converted into heat can be

evaluated by solving the equation, describing the evolution of induced electric field E . The energy balance of plasma heated by a return current driven by a relativistic electron beam can be given as:

$$\frac{d}{dt}W_{mag} = -RI^2 - 2\pi R_0 c E \cdot I_{RE}, \quad (1)$$

where W_{mag} is the magnetic energy of the RE beam, R is the resistance of the metal per unit of length and the last term corresponds to energy loss due to the work done by the RE beam [2], R_0 is the major radius of tokamak. Calculations of collisional damping of the induced current are presented in Fig. 1, where the RE magnetic energy loss in tungsten armour is plotted against the deposition time for the different W surface temperatures. It is seen, that for expected deposition time in DEMO (~ 0.3 - 0.5 sec) substantial portion of poloidal magnetic energy ≤ 1 GW will be dissipated in tungsten for surface temperatures ≥ 1500 K. The dissipation increases for higher temperatures because of the resistivity increase. These assessments are included in the calculation of the energy deposition of RE beams inside the W metallic armour by MEMOS code [3]. Below in this paper we assess the kinetic and magnetic energy stored in the RE during disruption for ITER and JET. Then we will estimate heat load onto the first wall in JET due to the RE impact and compare with experimental measurements of temperatures in the hot spots originated by the RE. We will show by using MEMOS code that for the carbon fibre composite (CFC) and at shallow incidence angles about half of the RE energy dissipates into the FW and that the magnetic energy, stored in the RE current is converted into heat at the wall structure. This can explain the non-linear dependence of the temperature at the hot spot on the RE current, observed in JET experiment. The collisional stopping power (SP) and the density effect correction have been considered in Chapter 4. And, finally, the SP and scattering angle calculations were performed for impinging RE on sandwich type PFC of ITER FW structure made from Be and W.

4.2 Kinetic and magnetic energy stored in the RE

In ITER one expects the average kinetic energy of a runaway electron as $E_d=12.5$ MeV [4]. In this case the relativistic scaling factor is $\gamma=(1-\beta^2)^{-1/2} = E_d/mc^2 \sim 24.5$ and $\beta \approx 0.9992$, where the average velocity of the RE is $\beta \cdot c$ and m is the rest mass of the electron. Since it is known that at most 70% of the plasma current is carried by RE [5], $I_{RE}= 10.5$ MA, their kinetic energy W_{kin} can be estimated by knowing the density of RE, which can be estimated as $n_{RE}=I_{RE}/ec\beta \cdot S \approx 1.2 \times 10^{16} \text{ m}^{-3}$ for the plasma poloidal cross section $S = 21.9 \text{ m}^2$ in ITER. The total number of RE in the entire plasma volume is then, $N_{RE}=V \cdot n_{RE} \approx 10^{19}$, where $V=837 \text{ m}^3$ for ITER; therefore, the total kinetic energy carried by runaways is $W_{kin}=N_{RE} \cdot (E_d - mc^2) \approx 20 \text{ MJ}$. The maximum magnetic energy carried by a RE beam can be estimated as $W_{REmag} \sim W_{mag} \cdot (I_{RE}/I_{pl})^2$ and, alternatively, from the Alfvén current $I_A=0.017\beta\gamma \approx 0.415$ MA as $W_{REmag} \sim W_{kin} \cdot (I_{RE}/I_{pl})$ [6]. Thus, in ITER, the maximum W_{REmag} can be 25 times higher than W_{kin} , i.e., $W_{REmag} \sim 0.5$ GJ. In the JET case, $E_d \sim 10$ MeV and $I_{RE} \sim 1$ MA [7]. Consequently, $I_A=0.33$ MA and $W_{REmag} \sim 2W_{kin}$. In general, losses in W_{kin} eventually could trigger the deposition of W_{mag} into the FW owing to the dissipation of induced currents in the structure. The stemming dissipation of W_{kin} is due to collisions of the RE with either the PFC or impurities in the plasma.

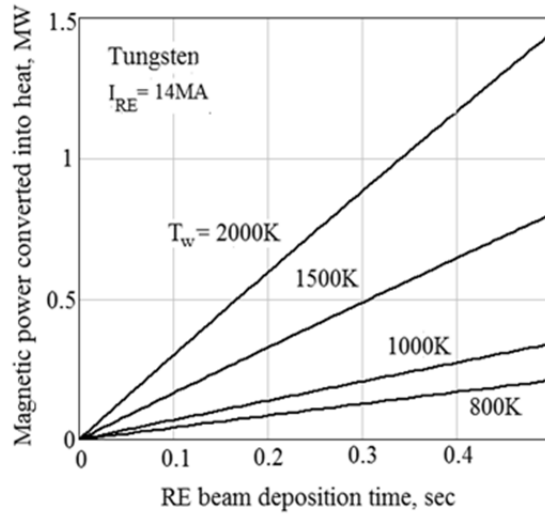


Fig. 1 The RE magnetic energy loss in W armour is plotted against the deposition time for the different W armour temperatures. It is seen, that for expected deposition time in DEMO (~ 0.3 - 0.5 sec) substantial portion of poloidal magnetic energy ≤ 1 GW will be dissipated in tungsten for surface temperatures ≥ 1500 K. The dissipation increases for higher temperatures because of the resistivity increase.

4.3 Heat load onto the first wall due to the RE impact

It has been shown in JET that a localized impact of the RE onto the upper dump plate leads to an increase of the surface temperature ΔT with an increase of the RE current I_{RE} [8]. The RE beam hits the plate where some portion η of the energy incident energy converts into heat. The energy Q released within some thin layer Δ in the surface area S during the time $\tau \leq \tau_{skin}$, can be written as:

$$Q = \frac{1}{S} \cdot \left(\frac{\tau \cdot \varepsilon}{e} \cdot I_{RE} + \frac{L \cdot I_{RE}^2}{2} \right) \propto \eta \cdot \frac{\tau}{S} \cdot R \cdot I_{eff}^2 \quad (2)$$

where the first term is the kinetic energy, ε is the average RE energy and the second term is the magnetic energy and L is the total inductance, R is the resistivity per unit length. The RE beam deposition time $\tau \sim 0.2$ ms $\gg t_{skin} \gg \tau_{skin} \sim 4\pi\Delta^2/c^2\rho$, where $\Delta \sim 0.2$ - 0.15 mm is the penetration length, $\rho \sim 1.2\mu\Omega$ m is the resistivity of CFC target [8]. In this case, the magnetic flux penetrates the plate inducing an ohmic current that reinforces the dissipating RE current. Eventually, the magnetic energy of the RE beam becomes thermal, so that $I_{eff} \sim I_{RE} (L/2R)^{1/2}$. Here, the resistance of the CFC target is $R \sim 1.8 \cdot 10^{-9} \Omega$ for the penetration length $\Delta \sim 0.2$ mm and $R \sim 1.3 \cdot 10^{-9} \Omega$ for $\Delta \sim 0.15$ mm and the spot area $S \sim 0.03$ m² [8]. The energy deposition of RE into the CFC target was evaluated by the MEMOS code for RE with $E_d \sim 8$ - 10 MeV, the deposition time $\tau \sim 0.2$ ms and $\alpha \approx 5^\circ$ - 20° [9]. The calculations show an almost linear dependence of surface temperature increase ΔT with an increase of heat energy Q :

$$Q_{MJ/m^2} \approx (\Delta T^\circ K - 34) / 234 \quad (3)$$

By substituting Q from (2) in (3), one gets the variation of surface temperature on the RE current:

$$\Delta T^{\circ} K \approx 34 + 234 \cdot \eta \cdot R \cdot I_{\text{eff}}^2 \tau / S \quad (4)$$

where η is the conversion efficiency, R is the resistance in Ω , I_{eff} is in A, S is the affected area in m^2 , τ is deposition time in sec. In Fig. 2, the solid curves show the deposition of the RE current energy into heat. They fit the experimental data (read squares) fairly well both in shape and quantitatively, if the conversion efficiency η assumed $\leq 50\%$.

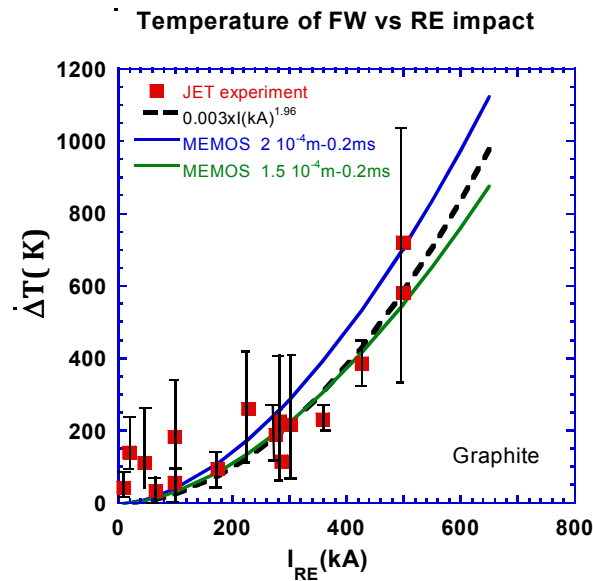


Fig.2 Surface temperature increase at the JET upper dump plate vs. the RE current increase measured in JET (red squares) [7]; the blue and green curves correspond to $\sim 50\%$ of the RE energy conversion into heat. Heat release on the plate due to RE impact calculated by MEMOS.

The MEMOS calculation shows that for the CFC and at shallow incidence angle about half of the RE energy dissipates while the rest reflects back with particles and radiation. Hence, our assessments show that the magnetic energy, stored in the RE current can be converted into heat at the FW structure.

4.4 Collisional stopping power and the density effect correction

The energy loss of RE passing through matter occurs mainly due to ionization and radiation and can be expressed in terms of the collisional and radiative stopping powers (SPs) [9,10]. We consider here only the collisional SP in order to assess the density effect on the energy loss. For relativistic electrons, the mass collisional SP defines the average energy transferred from incident RE electrons to bound atomic electrons [10]:

$$\left. \frac{1}{\rho} \frac{\partial E}{\partial s} \right|_{Coll} = \frac{A}{\beta^2} \left[B + 2 \ln(\beta\gamma) + \ln \frac{mc^2}{2} (\gamma - 1) + 1 - \beta^2 - \delta \right] \quad (5)$$

$$A = 2\pi r_e^2 m c^2 / \rho, \quad B = \ln(mc^2 / I)$$

Here, s is the penetration depth normal to in the target, $E = (\gamma - 1)mc^2$ is the kinetic energy, βc is the velocity of the runaways, Z is the atomic number, n is the electron density of the target, $I = 9.4 \cdot Z \text{ eV}$ is the mean excitation energy of the target atoms [9], and r_e is the classical radius of the electron $r_e = e^2 / mc^2$. The coefficients A and B are listed in the Table 1 for different target materials. The correction factor δ describes the polarizability of the medium, which reduces the effectiveness of distant collisions. The term δ depends on $\beta\gamma$ and can be fitted as [10]:

$$\delta(x) = \begin{cases} 4.606x + C, & x > x_1 \\ 4.606x + C + a \cdot (x_1 - x)^m, & x_0 < x < x_1 \end{cases} \quad (6)$$

where $x \equiv \log(\beta\gamma)$ and the constants x_0, x_1, m, a are given in Table I (see in [10]). This effect has been incorporated into the MEMOS code, following the prescription from [10]. Fig.3 displays the mass collisional SP as calculated from Eq. (4), with and without density effect correction. The density effect is more significant for high RE energies and low Z materials like Be, amounting to as much as 15% of the mass collisional SP at energies of 10 MeV (see Fig.3). For high Z materials, such as W, the density effect is smaller because its electrons are more strongly bound and hence less effective in polarizing the medium. The ENDEP calculations of the SP show a somewhat smaller effect, with and without density effect correction, due to SEG and radiation losses, not taken into account in Eq. (4).

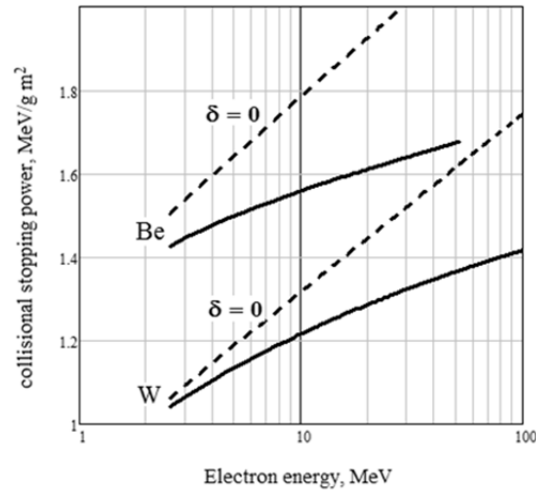


Fig.3 The SP of RE in Be and W vs RE energy. The solid curves show the values of mass-collisional SP calculated with density effect correction.

4.5 The results of ENDEP calculations for RE in ITER

The SP and scattering angle calculations were performed by the ENDEP code for impinging RE on sandwich type PFC structures, resembling ITER's FW. Figs. 4a and 4b show the SP (both collisional and radiative) as a function of penetration depth normal to the material surface for Be and W, respectively. The RE strike the plate with α in the range of 1° to 20° (depending on transverse velocity $\sim E_{tr}$) and $E_0=12.5\text{MeV}$. Five incident energy ranges have been chosen arbitrarily in our Monte Carlo computations (indicated with different colours). Figs. 4a, 4b show that the SP is smallest for the highest energy RE and also for that RE with the steepest incidence angle ($\alpha \approx 20^\circ$). Note also that the SP in Be is larger than that in W. Balance calculations indicate that only half of RE energy is absorbed in Be while the rest is reflected off mainly by back-scattered electrons ($\sim 48\%$) and photons ($\sim 2\%$). The fraction of back-scattered electrons is $\sim 77\%$ of the incident number but accounts for primary and secondary electrons. In W, the fraction of absorbed energy is $\sim 30\%$ while the rest is reflected off by back-scattered electrons ($\sim 55\%$) and photons ($\sim 15\%$). In this case, $\sim 82\%$ of the incident number of electrons is back-scattered. For , the ratio of absorbed energy reaches 80% in Be and 50% in W. We see in Fig. 3 that the SP decays more abruptly with penetration depth in W than in Be. For a given penetration depth, the SP drops by a factor of ~ 5 in W whereas it drops only by a factor of ~ 2 in Be. In the case of W, we find an enhanced SEG and radiation, which are one order of magnitude larger than that in Be.

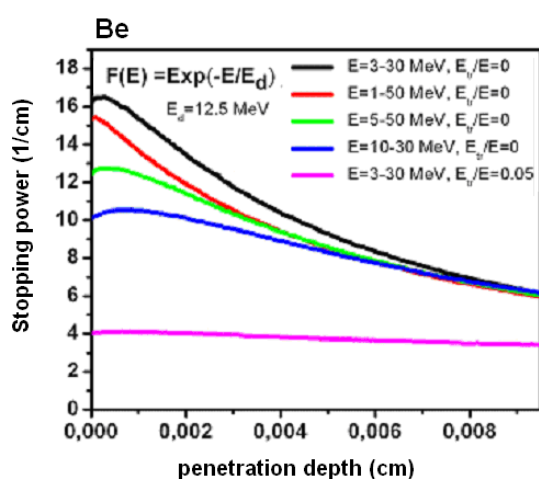


Fig.4a The SP for RE in Be plates shown as a function of the penetration depth. The incident electrons have a Gaussian distribution with $E_d=12.5$ eV. The five incident energy ranges indicated with different colors. The RE beam strikes the plate along the magnetic field line at $\sim 1^\circ$ for $E_{tr}=0$ and at $\sim 20^\circ$ for $E_{tr}/E \sim 0.05$.

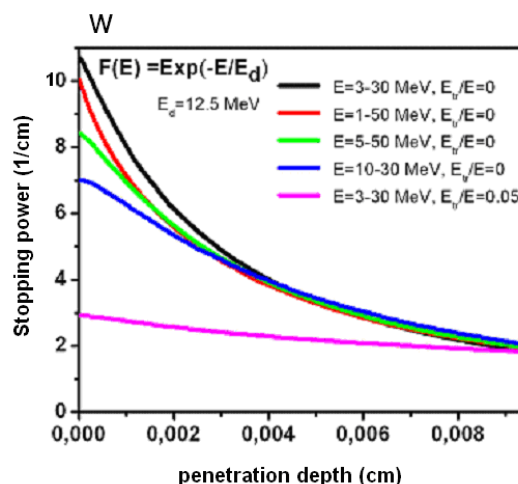


Fig.4b The SP for RE in W plates shown as a function of the penetration depth. The incident electrons have a Gaussian distribution with $E_d=12.5$ eV. The five incident energy ranges indicated with different colors. The RE beam strikes the plate along the magnetic field line at $\sim 1^\circ$ for $E_{tr}=0$ and at $\sim 20^\circ$ for $E_{tr}/E \sim 0.05$.

Therefore, less energetic particles enter in W than in Be. As a consequence, the “slow” RE in W interact more effectively with bound electrons than the “fast” electrons do in Be. For that reason, the SP drops more abruptly in W though, on the whole, the energy deposition is smaller in W because it simply carries less energy. The fraction of RE and energy passing to the structural material is negligible.

4.6 Conclusions

- A substantial portion of poloidal magnetic energy stored in the RE beam could dissipate in tungsten first wall during a direct impact. This occurs because of ohmic dissipation of a return current.
- The observed increase of temperature at a spot on the JET dump plate upon increasing the RE current can be explained by assuming that 50% of the RE energy, predominantly magnetic energy, is converted into heat.
- Calculations of the RE SP onto the ITER FW Be bulk armor predict strong erosion. The RE heat deposition is expected to be almost twice as large than the threshold energy for Be melting.

Acknowledgments

This work, supported by the European Communities under the contract of Association between EURATOM and Karlsruhe Institute of Technology, EURATOM and CCFE, was carried out within the framework of the European Fusion Development Agreement. The views and opinions expressed herein do not necessarily reflect those of the European Commission

4.7 References

- [1] A. Loarte A, V. Riccardo, J. Martin-Solís et al, "Magnetic energy flows during the current quench and termination of disruptions with runaway current plateau formation in JET and implications for ITER", 2011 Nucl. Fusion 51 073004.; Nygren, R., et al., J. Nucl. Mat. 241-243 (1997) 522.
- [2] M. Berger, M. Inokuti et al., Journal of the ICRU, v.9, issue 2, report 37, (1984)
- [3] B. Bazylev et al Physica Scripta, T128 (2007) 229-233;
- [4] M. Sugihara, RE specification for ITER, 2009
- [5] ITER Physics Basis, 1999, Nucl. Fusion 39, 2137
- [6] A. Loarte et al. Physica Scripta T128, p 222, (2007);
- [7] B. Bazylev , G. Arnoux, S. Brezinsek, Yu. Igitkhanov, M. Lehnen, V. Riccardo, V. Kiptily, JET EFDA contributors "Modeling of the impact of runaway electrons on the ILW in JET", Journal of Nuclear Materials 438 (2013) S237–S240.
- [8] G. Arnoux, B. Basylev, M. Lehnen et al., "Heat load measurements on the JET first wall during disruptions", Journal of Nuclear Materials, Vol: 415, Issue: 1, S817
- [9] R. Miller, Introduction to the Physics of Strong-Current Beams of Charged Particles, Plenum press, (1982).
- [10] R. Sternheimer, Phys.Rev.88, 851 (1952);

5 Towards a physics-integrated view of the inner fusion fuel cycle

Chr. Day^a, C. Gleason-Gonzalez^a, V. Hauer^a, Y. Igitkhanov^a, D. Kalupin^b, M. Valovic^c, S. Varoutis^a

^aKarlsruhe Institute of Technology (KIT), Karlsruhe, Germany,

^bEFDA-CSU, Garching, Germany, ^cCulham Science Centre (CCFE), Culham, UK

pape is presented on the 11th Symposium on Fusion Nuclear Technology 16 – 20 September 2013, ICFRM-11, Barcelona, Spain and is published in the Fusion Engineering and Design, 2014

Abstract. The sizing of the inner fuel cycle of a fusion machine is defined by the machine gas throughput and composition, and the sub-divertor neutral pressure at which the exhaust gas has to be pumped. Hence, it is primarily given by plasma physics needs and plasma control aspects, so that an integrated design approach is needed, which has to combine physics and technology. This paper outlines how physics aspects impact on the inner fuel cycle systems such as the torus exhaust vacuum pumps and the pellet injectors. Realisation of detachment conditions, improved understanding of the sub-divertor flow patterns and aspects of core fuelling are discussed as examples. The detachment onset conditions in conventional DEMO divertor is derived by using one-dimensional transport numerical model. Based on the derived detachment criterion the requirements on the gas throughput and the gas exhaust vacuum system are formulated. The analysis aims at the obtaining of number of cryopumps required for steady-state operation under detached divertor conditions.

5.1 Introduction

The fusion fuel cycle is a central element of a DT fusion machine. It comprises the fuel injection and gas based plasma control systems, the torus exhaust vacuum pumping systems and the tritium plant as well as the tritium breeding systems. All these are technical systems which are designed against requirements given by the fusion machine operation, and, finally, by plasma physics conditions. A good example of that is the inner fuel cycle whose size should be defined by the total gas throughput of the machine.

However, the engineering design of the fuel cycle sub-systems in the past has been developed separately, only relying on a small number of interface parameters, which were sometimes not defined with sufficient care and not traced to a rigorous physics basis. In recent years, more effort has been spent to improve this situation and to better interlink physics and technology issues in the interfaces of the inner fuel cycle with the plasma, viz the pellet injection systems and the divertor and its gas exhaust

vacuum pumping system. This paper starts with a qualitative discussion of the machine throughput and its contributions. Numbers are mainly given for ITER, as they are more consolidated than the ones under discussion for a power plant machine. Following that, a short introduction into the divertor and pellet systems is given and a workflow is developed how their technical design can be elaborated strictly from physics requirements.

This paper reflects current work done within the inner fuel cycle modelling project which is organised as focal activity in the EFDA ITER Physics Support Programme (Research Topic A10). The task of this project is to build the complete picture of the fuelling cycle for a machine like ITER/DEMO up to the knowledge presently available (fuelling cycle workflow), therefore to develop the interfaces between workflow elements (define data flowing between the components), to identify missing elements (e.g. not available physics/knowledge on some elements) and trigger their developments, and, finally, to apply the workflow for the fuelling cycle analysis.

5.2 Fuel cycle sub-systems

Figure 1 illustrates the basic scheme of the fuel cycle of a fusion power plant, which can be subdivided into an inner and an outer loop. The inner part denotes the directly plasma related gas flows and includes the fuelling system and the vacuum pumping systems. For a fusion power plant, a shortcut may be added between the pumping and the fuelling systems that provides for direct internal recycling (DIR) of unburnt fuel [1,2]. The outer part covers the breeding blankets, with the systems to generate the tritium, to extract it from the breeder, and purify the coolant which will take up permeated tritium. For ITER, tritium will be supplied from external sources; hence, the outer part is only established at a minimum level via test blanket modules that allow for initial studies in a fusion environment, but with negligible tritium production. The tritium plant with its main elements of fuel clean-up, isotope separation, storage and delivery is a key system for both loops. This paper will focus on the interfaces between the inner fuel cycle and the main plasma chamber. Principle considerations to study the gas management of the inner fuel cycle should start from the elementary particle control functions that have to be provided: (a) provision of the fuel to the plasma; (b) provision of fuel-type gases to the neutral beam injection systems (NBI); (c) provision of additional plasma control (ELM pacing, divertor de-/attachment conditions); (d) tritium accountancy and gas analysis measurement for tritium inventory determination; (e) fusion ash exhaust via divertor and vacuum pumping of exhaust gas from torus and NBI; (f) exhaust gas cleaning and processing as well as fuel recovery. The central design requirement on the inner fuel cycle is the gas throughput for which the torus exhaust vacuum pumping system has to be designed for. This corresponds to the steady-state fuelling rate plus the gas throughputs of other, non-hydrogenic gas species that are injected into the torus chamber mainly for plasma control and divertor protection. The numbers taken from the ITER baseline are shown in Table 1. It must be noted that the design of the vacuum pumping systems does also have to reflect the pressures which have to be maintained in the sub-divertor region. For DT plasmas they are defined as 1-10 Pa, for He-rich plasmas in the initial phase of ITER operation even 0.25-10 Pa. As such a wide pressure variation cannot be met simultaneously at constant pumping speed and constant throughput (pumping speed is defined as the

ratio of throughput and pressure), there has to be a performance cut, at which the manageable throughput decreases with decreasing pressure.

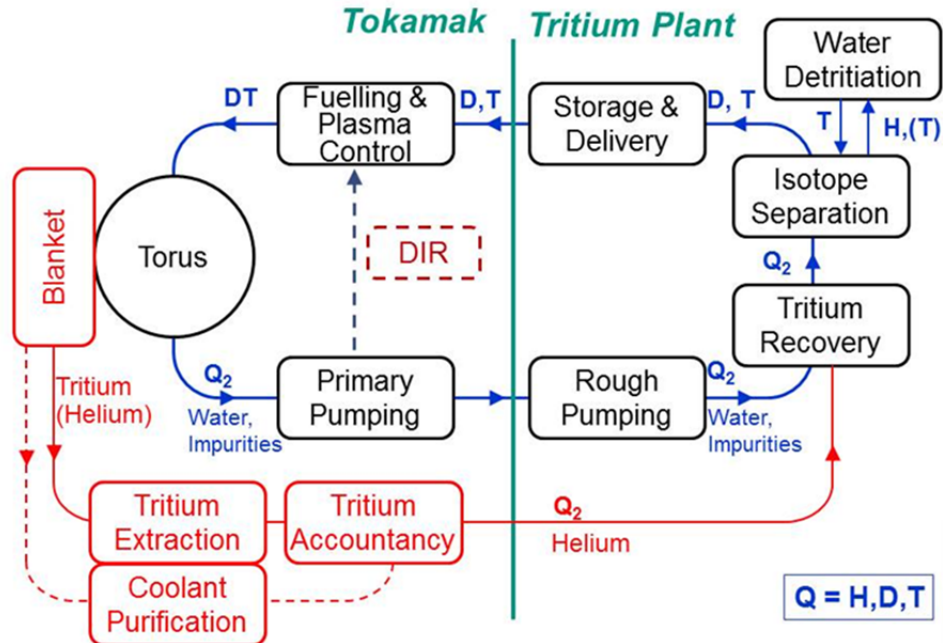


Fig. 1 Block diagram of the fusion fuel cycle.

This cut point is at approximately 4 Pa for the He-rich plasmas, and at 3 Pa under DT plasma operation conditions, so that at the minimum pressure side the acceptable throughputs are considerably smaller (only 6% for the He-rich plasmas, 25% for DT operation). This illustrates very well that the torus exhaust vacuum pumping system has a direct impact on the operational window of the fusion device.

5.3 Contributions to machine throughput

Fuel need for the fusion reaction: A simple calculation of the DT fusion reaction yields for 100 MW fusion alpha power ($E=3.5$ MeV) an atomic throughput of $N=3.6 \cdot 10^{20}/s$ or a molecular gas throughput of $0.6 \text{ Pa} \cdot \text{m}^3/s$ (referenced to $T=273.15$ K). For ITER with a reference fusion power of 500 MW, this sums up to $3.4 \text{ Pa} \cdot \text{m}^3/s$, this is a negligible contribution. Neutral beam fuelling: The three ITER NBIs together will inject 51 MW with deuterium ions accelerated to 1 MeV, which corresponds to an injected molecular gas throughput of $0.6 \text{ Pa} \cdot \text{m}^3/s$, which is also a negligible contribution.

Table 1. Gas throughput at ITER.

Gas source	Pulse flat top duration [s]	Av.exhaust throughput [Pa·m ³ /s]	Comment
Fuelling	400	200	hydrogenic
Fuelling	1000	160	fuelling
Fuelling	3000	120	
Fuelling	200	120	He/H fuelling
He ash		10	Burning plasma
Other gases		10	N ₂ , Ar, Ne

The gas throughput has a number of different contributions that are discussed below.

In order to understand the need for significantly larger throughputs one has to have a closer look on the plasma itself. From the simplest point of view, the plasma can be subdivided in the core and the edge. The density profile in the core can be linear or peaked, but there is always a strong density gradient in the pedestal. This means that any injected material has to be transported through the SOL to the core against the density gradient. From transport code calculations it was found that there is a maximum achievable edge density limit that cannot be surpassed by conventional gas fuelling (for ITER this limit is at about 10 Pa·m³/s). In other words: All additional gas flows directly through the SOL to the divertor and increases the flowrate to the pumping system, but does not help to fuel the plasma core. The main fuelling has therefore to be done by a method that is able to deposit fuel particles deeper into the core. One method is the supersonic molecular beam injection (SMBI) that utilizes an additional Laval nozzle at the exit of the gas injection tube to provide increased velocities. But the most prominent method with the best fuelling efficiency at the moment is pellet injection.

Pellet core fuelling: Transport calculations show that if one is aiming to have maximum density in the core (in order to have maximum volumetric fusion energy production, which is essential to increase the efficiency for a power plant), this would be around the Greenwald density which is 1.2·10²⁰/m³ for ITER, which asks for core fuelling at a rate of about 40 Pa·m³/s (at ITER reference fusion power) [3]. However, although pellets can survive the edge barrier and reach the core, they do also have significant losses on the way, so that the throughput to be injected as pellets has to be higher than the number above. The accurate calculation of ablation and deposition profiles is an ongoing R&D activity, but the additional SOL flowrate is expected to be of the order of ~ 140 Pa·m³/s to ensure the wanted core fuelling rate. i.e.

the pellet injector system has to inject $\sim 180 \text{ Pa}\cdot\text{m}^3/\text{s}$ at ITER, 75% of which gets lost, flows out through SOL and acts fully as a load for the pumping systems. For a DEMO with 3 GW fusion power, the estimated pellet fuelling rate is $280 \text{ Pa}\cdot\text{m}^3/\text{s}$ with a similar ratio of core/SOL flow [4].

Fuelling for helium removal: Regarding the core fuelling requirement, for a burning DT plasma, one has to check, if the acceptable He impurity level stays below 5%. With the burn-up rate of $3.4 \text{ Pa}\cdot\text{m}^3/\text{s}$, this constraint is fulfilled for any core fuelling rate above $3.4/0.05 \text{ Pa}\cdot\text{m}^3/\text{s} = 68 \text{ Pa}\cdot\text{m}^3/\text{s}$, which is ensured by the pellet core fuelling rate stated above. Thus, this does not add an additional requirement.

ELM fuel pellet pacing: On top, there comes additional fuel gas for pellet ELM pacing (if this approach will be implemented). Results from all major devices (AUG, DIII-D, MAST, JET) show clearly that pellet pacing of ELMS is a viable method for ELM control. For ITER, the ELM pacing portion is estimated to be of the order of $75 \text{ Pa}\cdot\text{m}^3/\text{s}$ [5]. ELM control can also be achieved by magnetic perturbation. As the pellet injector parameters for core fuelling and ELM control are rather different (location, size, frequency), it would be beneficial to have dedicated systems and not to need to combine the two functions in one injector.

Divertor radiative seeding: This effect is not adding fuel but high or medium Z impurities to reduce the power transported into SOL and, thus, limit the divertor power load. Calculations show the impurity seeding rate to reduce the divertor wall load to values below $5 \text{ MW}/\text{m}^2$ is in the order of (integrally) below 0.05% for Xe and 2% of Ne, hence negligible [4]. The value of $5 \text{ MW}/\text{m}^2$ is the currently accepted value under the neutron loads foreseen at DEMO and considerably less than accepted for ITER.

Gas puffing to reconstitute confinement for a metal wall environment: This contribution reflects the newest findings in AUG with a tungsten wall or JET with the ITER-like wall, which shows that additional gas has to be puffed to achieve a plasma that is similarly stable as for a carbon wall. This new result is not yet fully understood and the results are not all consistent, but the additional gas portion may be significant (up to 50% of the pellet core fuelling throughput) [6, 7]. This gas is not fuel, but e.g. nitrogen (It is currently tried to find an alternative gas, as nitrogen is anticipated to form ammonia and this potentially leads to corrosion problems in the fuel cycle inlet systems).

It is obvious that the chosen ITER reference throughput is not an 'accurate' frozen number but will be found within the ITER research programme itself. The current design for tokamak exhaust pumping in ITER is based on a cryogenic solution, which is always characterised by a point design given by the maximum acceptable heat load of the pumped gas throughput. In view of the aspects delineated above, it would be beneficial for a DEMO to develop a torus exhaust pumping system that provides sufficient flexibility against potentially rising gas throughput numbers.

The following section presents two example cases, which show how a detailed physics approach linked with engineering considerations to enable an integrated design development.

5.4 Physics-integrated approach for the torus exhaust vacuum pumps

The machine throughput and composition alone is not sufficient to make an appropriate design of the vacuum system. On top has to come the information on the pressure or density at which this throughput has to be pumped. This density is given from plasma considerations, among which the divertor detachment criterion is the strongest one.

The realization of fusion plasma with a high efficiency and hence maximum density is a central requirement to a fusion power plant. With further increase of the plasma density more impurities are released by plasma facing components that raise the radiation levels. To stimulate this also for the divertor, impurities have to be puffed into the divertor for obtaining the required radiation and thus cooling of the divertor volume. As the temperature in the divertor decreases over a large volume, electrons and ions recombine to form neutrals volumetrically. This process is amplified by the presence of those neutrals that, recycled at solid surfaces, now act as a “break” for the plasma that flows towards the targets through friction. They increase the time that the charged particles have for recombining, making this process more likely to happen. When this occurs in large quantities the measured particle flux at the target plates drops strongly. Neutral atoms transport the residual power and as they are not bound by magnetic field lines, they can deposit power and particles over broad areas reducing the peak values to acceptable levels for materials to sustain the bombardment. This regime is known as detached divertor operation. Plasma detachment allows higher operating temperatures upstream. Due to the high neutral particle densities/pressures established in the divertor volume in front of the pump ducts, the pumping of the helium ash becomes more efficient.

The detachment criterion defines very clearly operational limit points that can be translated into requirements on the gas throughput and the gas exhaust vacuum system under. In order to illustrate this strong interrelation, a quantitative analysis has been made for the ITER like divertor and torus exhaust vacuum configuration (with cryopumps) in a DEMO reactor environment with argon as radiative seeding gas. The analysis provides the number of cryopumps required for steady-state operation under detached divertor conditions. The effective pumping speed at the full divertor ring results from the balance of the pumping speed of all divertor vacuum pumps (connected via ducts and ports with the subdivertor region of some divertors; other divertors are linked to these via toroidal slots) and the plasma that is treated as a pump with black hole pumping speed via the openings with which divertor cassettes face the plasma (toroidally and poloidally). The numerical values were taken from [8]. The dependence of the effective pumping speed per cryopump on divertor neutral density was approximated as shown in figure 2. The modelling of the transition from attached to detached states was done according [9].

Detachment can occur when the radiation in the divertor / SOL region is strong enough to limit the ionisation capability downstream of the radiating region. To obtain reduced ion flux to the target while satisfying the momentum balance along the field lines, a significant pressure drop from the mid-plane to the target has to occur. Such a pressure drop can be achieved if neutrals interact with the cold plasma

fan over a significant length [10]. The radiation in the SOL is limited because of the edge density limit, and the possibility of plasma detachment depends on momentum and energy losses in the boundary plasma.

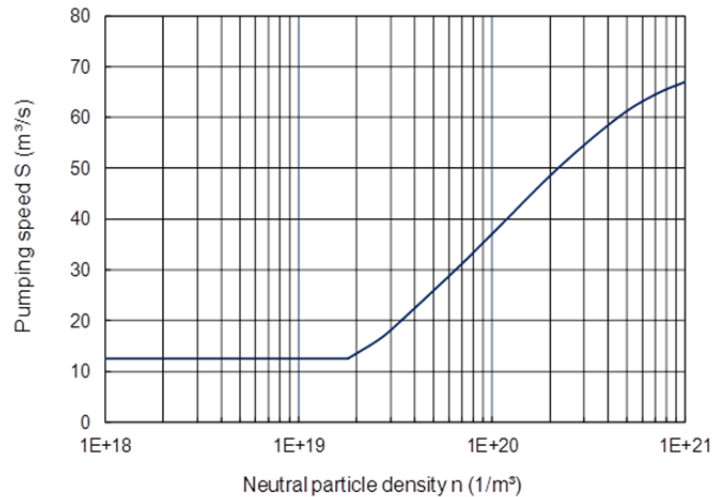


Fig. 2. Approximation of the effective pumping speed per cryopump as a function of the divertor particle density.

In the chosen approach [9] two regions are defined: the radiation region and the cushion. In the radiation region, energy is lost by impurity radiation. The power is transported by parallel heat conduction, which is valid except very close to the cushion. In the cushion, the plasma is cold and the remaining power is so small that ionisation is excluded. The temperature is taken to be constant within the region and convection dominates the heat flow. The location of the cushion develops self-consistently according to the energy, particle and momentum balance equations, which are solved for given values of the upstream density n_{up} and power q_{up} and variable impurity level of the injected argon. In the cushion, neutrals provide momentum loss, reducing the pressure below that of the attached state. Calculations are performed for DEMO-typical conditions, where the power to the divertor is $P \sim 230$ MW, which translates into an input heat flux density along the field lines of $q_{//} \sim 500$ MW/m². We also assume an upstream (separatrix) temperature T_{up} of ~ 3 keV and a density $n_{up} = 0.35 \cdot 10^{20}/m^3$. With increasing impurity concentration, the particle fluxes at the divertor plate decrease continuously. For the input numbers stated above, detachment was found for an argon ion concentration of 0.7% at a requested particle exhaust flux Φ of $2 \cdot 3 \cdot 10^{23}/m^2/s$ and the neutral density in the divertor n to be $1 \cdot 10^{20}/m^3$. To maintain this operational point and, thus, to ensure the detachment onset, the particle flux to be exhausted can be calculated as a function of the divertor neutral density. In a final step, utilizing the curve shown in figure 2, this can be converted in number of cryopumps, as plotted in figure 3. At the required flux and density values, this yields about 6 cryopumps needed.

This is a very good example how a physics requirement can be directly translated into an engineering design requirement. It must be noted that the quantitative result above should be seen as very preliminary as based on many assumptions, but the general algorithm and workflow holds independent of the numbers used.

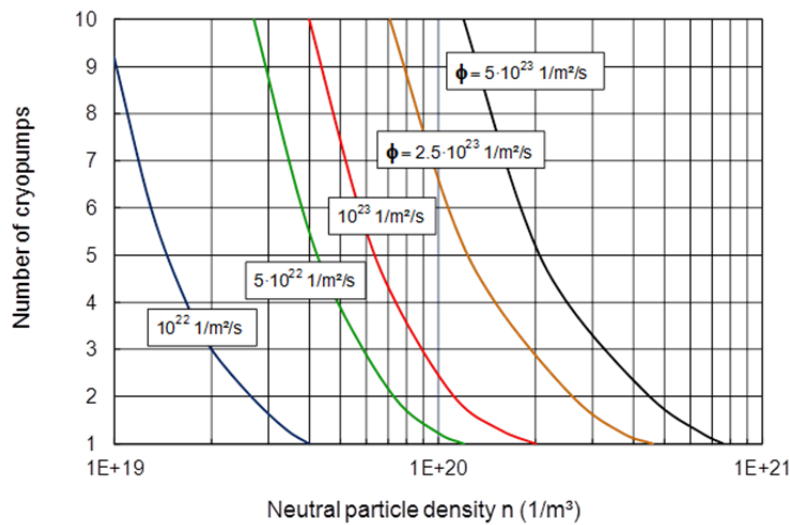


Fig. 3. The number of required cryopumps as a function of neutral density for different particle fluxes in the divertor

Figure 2 above was derived for a cryogenic pump at ITER-relevant duct geometries. If DEMO will have different pumping systems and pump ports, this has to be considered [2]. The calculation of the effective pumping speed available at the divertor from the actual pumping speed of a torus exhaust vacuum pump is a very complicated problem as such, as the neutral flow is covering a wide range of Knudsen numbers starting from viscous in the divertor cassette itself down to free molecular at the most downstream side. Therefore, the EFDA ITER Physics Programme is supporting two approaches for converting complex flow configurations into networks of flows: An empiric approach (ITERVAC-Code) [11] and a deterministic approach using tabulated solutions of the kinetic equation [12]. It is found that the two approaches agree reasonably well.

Both the detachment analysis [9] and the effective pumping speed evaluation [7] is based on a 1D lumped approach. An alternative, much more consistent and physics-based approach is to simulate the sub-divertor neutral gas region by the Boltzmann equation for neutral gas movements using particle fluxes along the (simplified) divertor contour as boundary conditions that have been consistently calculated in a separate step by a plasma physics code (SOLPS [13], SONIC). Also this approach has already started and is being developed under the EFDA ITER Physics Programme. The Boltzmann equation is solved statistically using the DSMC method. First results are very encouraging [14].

This approach can be done in 3D if needed and allows to go one step further, as it gives a consistent picture of density and particle distribution in the complete sub-divertor volume. Just as an example, figure 4 illustrates the calculated helium partial pressure distribution along a reference plane in a 2D representation of the ITER-type divertor for two different total pressure cases. The divertor geometry and the simulated areas are indicated in the top of figure 4. The middle shows the simulation results in terms of pressure, and the bottom picture illustrates the pressure profile along the line indicated in the middle. In a similar way all other macroscopic quantities (e.g. velocity) can be calculated from the DSMC result.

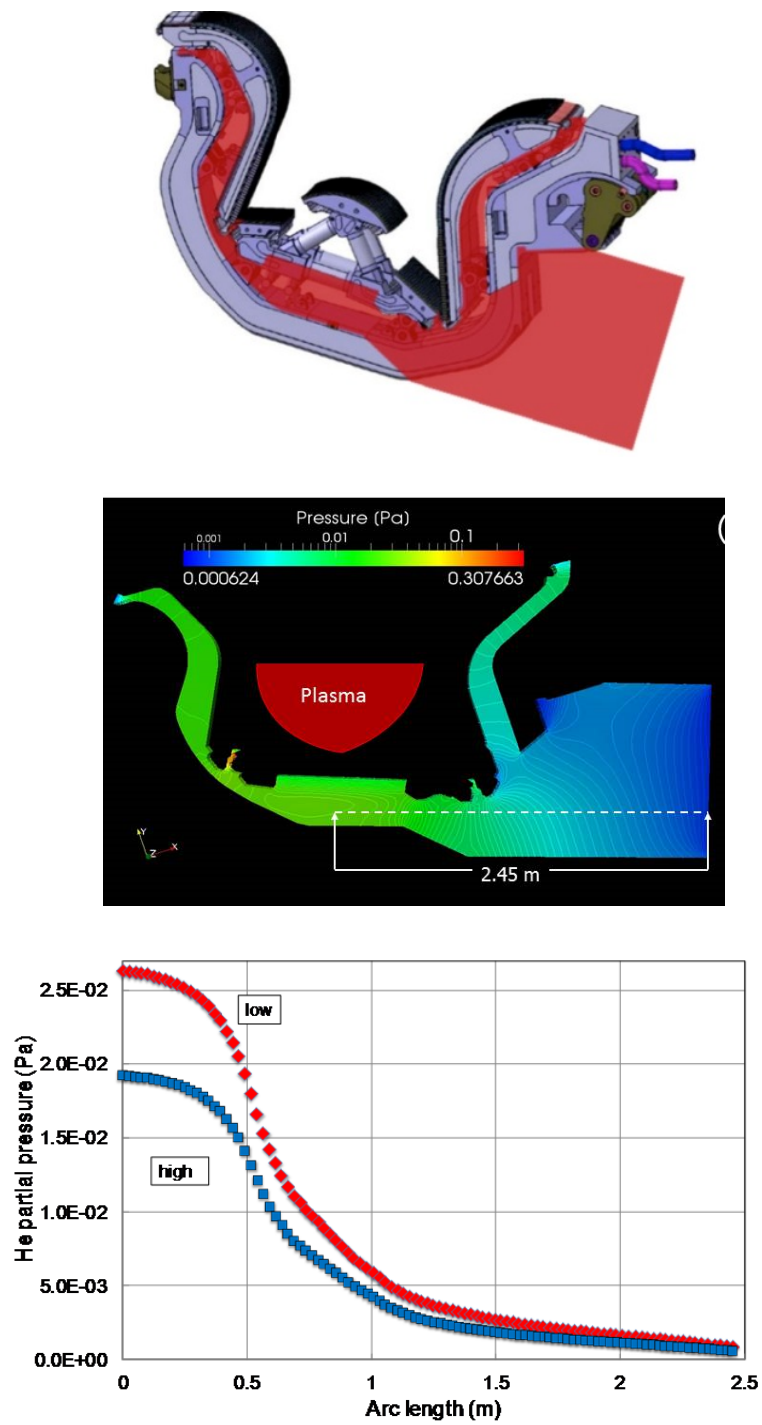


Fig. 4. Example of a consistent DSMC simulation of neutral partial pressures in the sub-divertor region, using SOLPS fluxes along the divertor targets as boundary conditions. 'High' indicates a case with a high total pressure of 9.9 Pa, 'low' denotes a total pressure of 2.6 Pa.

5.5 Physics-integrated approach for the pellet injectors

As described in section 2, the main function of the pellet injection systems is core fuelling (injection from high field side), whereas ELM mitigation can alternatively be done with resonance magnetic perturbation (RMP) coils. However, this can only work if the pellets and the mitigated ELMs do not interact, which is under investigation now. The pellet throughput is inversely proportional to the pellet retention time, which depends on (i) the depth of deposition and (ii) post pellet losses (which depend on the character of the ELM mitigation). The processes of pellet particle deposition depend primarily on the ExB drift of the ionised ablated pellet particle cloudlets (plasmoids) and their homogenisation dynamics. It therefore directly depends on the magnetic configuration and this is why different injection directions have to be considered (low field side vs. high field side).

The pellet throughput (namely the losses, which make for about 75% for current pellet injector configurations) depends strongly on the deposition depth and the density profile. Adequate models and understanding is urgently needed in all above elements to optimise fuel throughput inside physics and engineering envelopes. The former is defined in terms of pellet ablation and losses, whereas the latter is defined in terms of pellet size, frequency and injection depth (velocity) which defines the deposition zone. A workflow to translate from one into the other world is under work, involving experimental results (MAST, JET) and parametric studies with the HPI2 code.

5.6 Conclusion

This paper shows the importance to have a fundamental understanding of the necessary machine throughput and its contributions, and the advantages that result if this physics understanding can be integrated in the technical design development of the fuel cycle systems. To enable this, workflows have to be defined that translate physics conditions in engineering parameters. This requires a team approach which combines physics and engineering expertise. In order to improve this understanding, the determination of the optimum particle throughput is one of the central headlines of the upcoming European fusion programme to be implemented under the Horizon 2020 EU framework programme.

Acknowledgments

This work, supported by the European Communities under the Contract of Association between EURATOM and Karlsruhe Institute of Technology (KIT) and Culham Science Centre (CCFE), respectively, was carried out within the framework of the European Fusion Development Agreement (EFDA) under its ITER Physics Support Activities. The views and opinions expressed herein do not necessarily reflect those of the European Commission.

5.7 References

- [1] C. Day, T. Giegerich, The Direct Internal Recycling concept to simplify the fuel cycle of a fusion power plant, *Fus. Eng. Des.* (2013), in press
- [2] T. Giegerich, C. Day, The KALPUREX Process – a new vacuum pumping process for exhaust gases in fusion power plants, This Conference
- [3] A.S. Kukushkin et al., *J. Nuc. Mat.* 415 (2011) S492-S496
- [4] G.W. Pacher et al., *Nuclear Fusion* 47 (2007) 469-478
- [5] A.S. Kukushkin et al., *J. Nuc. Mat.* 415 (2011) S497-S500
- [6] R. Neu et al., Experience with tungsten plasma facing components in ASDEX Upgrade and JET, *IEEE Transactions on Plasma Science* (2013), in press
- [7] E. Joffrin et al., Scenario development at JET with the new ITER-like wall, *Nuclear Fusion* (2013), in press
- [8] V. Hauer, Chr. Day, *Fus. Eng. Des.* 84 (2009) 903-907
- [9] Yu. Igitkhanov et al., *Proc. 21st EPS, Montpellier*, , vol18B, part II, p.714, 1994
- [10] G. Janeschitz et al., *J. Nucl. Mat.* 220-222 (1995) 73-88.
- [11] C. Day et al., Development of a simulation code for ITER vacuum flows, in: *IAEA Fusion Energy Conf.* (2006), http://www-pub.iaea.org/MTCD/Meetings/FEC2006/it_p2-12.pdf
- [12] S. Misdanitis, D. Valougeorgis, Modelling of ITER related vacuum gas pumping distribution systems, *Fus. Eng. Des.* (2013), in press
- [13] A.S. Kukushkin et al., *Fus. Eng. Des.* 86 (2011) 2865-2873
- [14] F. Köchl et al., Modelling of pellet particle ablation and deposition: The hydrogen pellet injection code HPI2, *Nuclear Fusion* (2013), in press

6 Extend physics assessment of novel divertor configuration

Yu. Igitkhanov,

Karlsruhe Institute of Technology, IHM, Karlsruhe, Germany

Final EFDA report 2013

Task: WP13-PEX-02-T02-01/KIT/PS;

Task: WP12-PEX-02-T03-01/KIT/PS

In this report we assess some important physics issues related to the snowflake (SF) configuration, namely effect of flux expansion/connection length/poloidal length on stability of impurity radiation in SF configuration and the coupling of MARFE with the ballooning type MHD instability.

6.1 Effect of flux expansion, connection length on stability of radiation

In the snowflake (SF) configuration the poloidal magnetic flux becomes strongly broadened well above the second-order null point, making the geometrical connectivity of the divertor with the main SOL easier than in the standard divertor. This may lead to the increased impurities flow to the vicinity of the null point and an increase of plasma radiation from that region. The plasma radiation locally decrease the temperature in circumstances where the cooling itself leads to an increase of radiation and hence the further cooling. Below we will consider a 2D stability analysis of the MARFE-type perturbation inside the last magnetic surface in a toroidal geometry with a separatrix and will show that the broadening of the null point region facilitates the onset of thermal instability. The impurity radiation loss is proportional to the electron density, n , the impurity fraction f_z , the local emissivity, L , and the volume of the radiative region, dV :

$$W = \int f_z n^2 L(T, n) dV \approx \overline{f_z n^2 L} \cdot V_{rad} \quad (1)$$

The radiative volume V_{rad} is determined by the peak of either f_z , L , or n^2 . Each of those parameters can strongly affect the magnitude of impurity radiation. Experimental observations show that for some cases (MARFE [1], and radiative divertor [2]) a significant amount of radiation (approximately a half) is coming from relatively small volume of rather cold plasma. It is possible that this effect may be explained by the local increase of the emissivity and impurity fraction f_z . However, even for $f_z = \text{const.}$, and $L = \text{const.}$ these features of the MARFE and radiative divertor can be explained by high value of $n^2 V$ in the low temperature region caused by the perpendicular plasma energy transport. Impurity radiation in simple 1D approximation can be easily expressed as

$$W \approx 4\pi R \cdot \Delta_0 \cdot \sqrt{2 \int f_z \cdot n^2 \cdot \chi_{||}(T) \cdot L(T) \cdot dT} \quad (2)$$

Here $\chi_{||} = \chi_0 T^{5/2}$ is the electron conductivity along B and Δ_0 denotes the SOL width at the mid-plane. However, the radiation is localized in the vicinity to null point, where the SOL width Δ is broader than at the mid-plane because of the contribution of heat transport across the field lines and the magnetic geometry of the SF configuration:

$$\Delta \propto \Delta_0 \cdot \sqrt{\chi_{||} / \chi_{\perp}} \cdot \left(\frac{b}{\Delta_0} \right)^{2/3} \quad (3)$$

Substitution of this estimate in Eq. (2) gives $W \approx \sqrt{\chi / \chi_{\perp}} \cdot (\dots)^{1/2} \propto \sqrt{\chi_{\perp}}$ or

$$W \approx S_{rad} \cdot \sqrt{2 \int f_z \cdot n_2 \cdot \chi_{\perp}(T) L(T) dT}, \quad (4)$$

Therefore, a strong impurity radiation occurs in the low temperature region, where the perpendicular plasma heat transport dominates. Here S_{rad} is the surface of the radiating flame enveloping the area near the null point. The upper limit of the integral in Eq. (4) can be taken infinity, because the integral converges unless χ_{\perp} , f_z or L increase very rapidly with the temperature increase.

The radiation losses can be roughly estimated from the energy balance equation on the close magnetic surfaces close to separatrix by retaining only radial derivatives in the energy balance equations and considering the parallel heat transport as a sink:

$$\chi_{\perp} \nabla_{\perp} \cdot T \approx f_z n^2 L - \chi_0 \frac{T^{5/2}}{l^2} \quad (5)$$

The connection length l between the equatorial plane and the vicinity of the null point for the standard divertor is $l = (qR) \ln(b/\Delta_0)$, where q , R and Δ_0 (the SOL thickness) are taken at the equatorial plane. For the SF case $l_{sf} = (qR) (a^2/b\Delta_0)^{1/3} = l \cdot (a/b)^{1/3} (a/\Delta_0)^{1/3} / \ln(b/\Delta_0)$ that considerably exceeds l [3]. Linearizing Eq. (5) and assuming adiabatic type of perturbation one gets the condition for the instability onset:

$$f_z \cdot n \cdot T^2 \frac{d}{dT} \left(\frac{L(T)}{T^2} \right) > \left(\frac{\pi}{\Delta} \right)^2 \cdot \chi_{\perp} + \chi_0 \frac{T^{7/2}}{n \cdot l^2} \quad (6)$$

In the vicinity to null point $l \rightarrow \infty$ and the last term in (6) can be omitted. Therefore, the increase of connection length reduces a stabilizing effect of parallel heat flux. The heat flux due to the perpendicular thermal conduction varies as $1/\Delta^2$. Δ being determined in part by the width of a radiative cloud above the null point and this in turn depending on the radial temperature gradient. Simple assessment can be made without solving Eq.(6) by assuming that temperature in the cloud is about $T \sim 20\text{eV}$, density $\sim 10^{20}\text{m}^{-3}$, the anomalous value of $\chi_{\perp} \sim 3\text{m}^2\text{s}^{-1}$ and $\chi_{\parallel} \sim 1.3 \cdot 10^{22} \cdot T^{5/2}$. Comparing two terms on the r.h.s. of Eq. 6 it is seen that perpendicular thermal conduction is dominant for $\Delta \leq 23/T^{5/4}$ (eV) $\sim 50\text{cm}$. Using the coronal emissivity for carbon impurities to estimate the radiation term in Eq. (6) for considered density and temperature a typical value might be $\sim 10^{26} f_z \text{m}^{-3} \text{s}^{-1}$. This term should be compared with the first term in the r.h.s. of Eq. 6, which gives $f_z \geq 0.25/\Delta^2$, where Δ is in cm. For our estimations we will take $\Delta \sim 15\text{cm}$. Therefore, for example, a 0.1% impurity level would sustain a MARFE with the width greater than 15cm. Fig. 1 shows the marginal impurity level in the case of the SF configurations and for the conventional x-point case. It is important to note additionally that in the case of SF configuration Δ substantially exceeds that for the conventional x-point configuration. The smaller temperature gradient length the weaker the stabilizing effect is and, a smaller impurity concentration could trigger the instability. This simple assessment shows that the SF configuration is more vulnerable to the onset of MARFE type instability. The main reason eventually is the higher concentration of plasma/impurity density expected in the broader region above the null-point on the closed magnetic surfaces in the SF configuration.

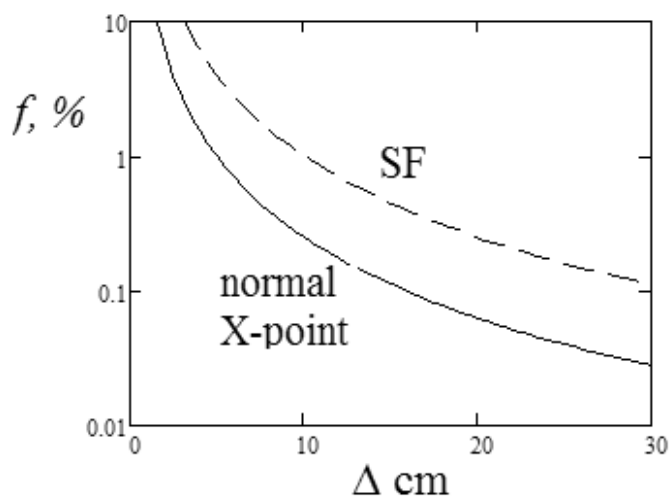


Fig.1 Impurity concentration (carbon) required for onset of the temperature instability in the case of the SF (dashed) and conventional x-point divertor.

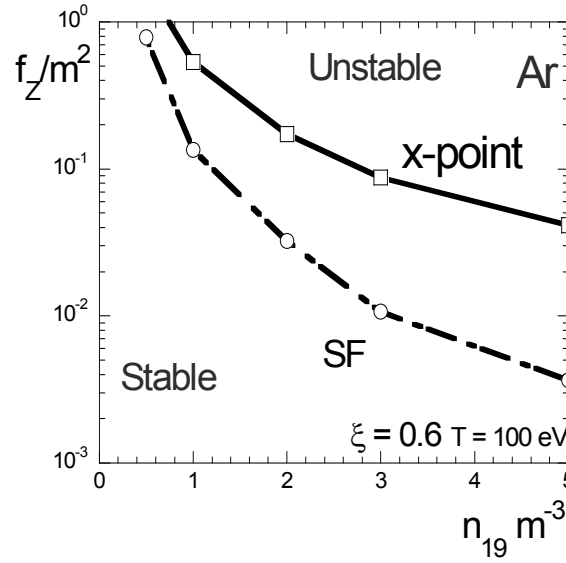


Fig. 2 Ar concentration vs. plasma density at given toroidal mode number m , boundary temperatures $T = 100\text{eV}$, $\xi = 0.6$; above the curves the configuration is unstable for both cases (see details in appendix)

The detailed analysis of thermal instability onset has been carried out for the x-point configuration (see the attachment below). In the Fig. 2 the critical impurity concentration (in this case of Ar) required for MARFE onset as a function of the plasma density for the SF and the normal x-point configurations is shown. The perturbation mode number m is localized at the radial $\xi=0.6$ position. It is seen that the SF configuration is more vulnerable to the onset of MARFE. It can be triggered at lower impurity concentration. For higher densities above the null-point the difference in marginal impurity concentration f_z is more pronounced. Excitation of high toroidal mode numbers occurs for smaller concentration.

6.2 Coupling of ballooning instability with thermal instability

Here we analyze a snow flake (SF) alternative divertor magnetic configuration with respect to coupling of ballooning instability with thermal (MARFE) instability under DEMO conditions [4]. We also consider of ballooning instability in specific snow-flake topology of magnetic field in the vicinity to X-point. The separatrix and x-point region is immediate affected by boundary plasma and as a result could trigger MHD instability. However the features of MHD perturbation near the expanded SF region is not well known. Ballooning modes appear to be the most unstable in this region due to increase of potential magnetic well. The ballooning equation for the marginal stability reads as:

$$\left(\bar{B}\nabla\right)\cdot\left[\frac{k_{\perp}^2}{B^2}\cdot\left(\bar{B}\nabla\right)\cdot\xi\right]+2(1-\gamma)\cdot\left[\bar{B}x\bar{k}\right]\cdot\nabla p)\cdot\left(\frac{\left[\bar{B}x\bar{k}\right]\cdot\bar{k}}{B^4}\right)\cdot\xi=0 \quad (1)$$

Metrics for SF geometry is simplified and is taken as magnetic topology of the straight current strings combine with the toroidal angle ϕ (see Fig.3).

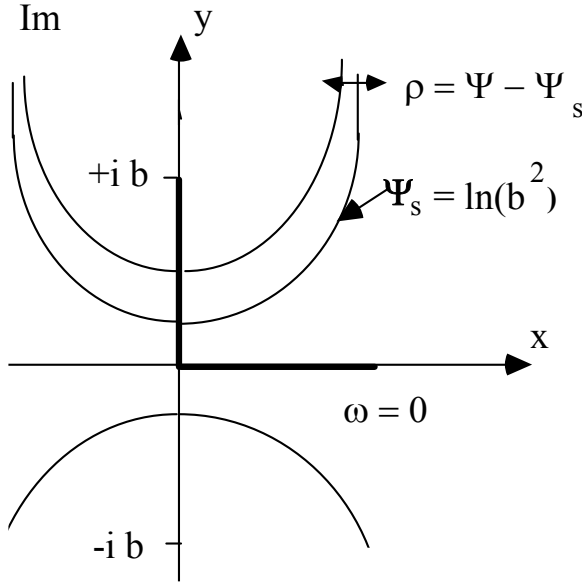


Fig. 3 Magnetic topology of the straight current strings

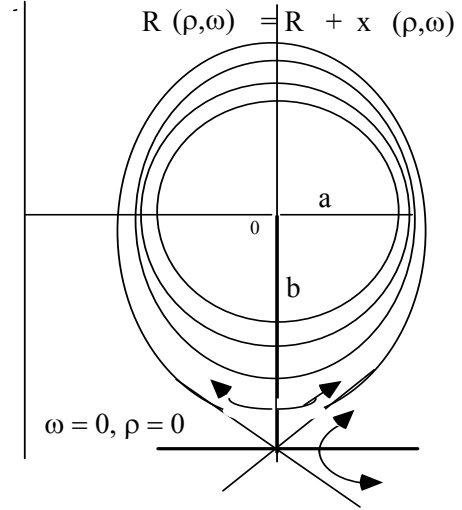


Fig. 4 Magnetic topology of SF used for ballooning stability analysis.

$$ds^2 = h_\rho^2 d\rho^2 + h_\omega^2 d\omega^2 + R^2 d\phi^2$$

And near the SF region, where $\rho, \omega \ll 1$

$$h \equiv h_\rho = h_\omega = \frac{b}{2\sqrt{1 - \cos \omega + \rho^2/2}}$$

The flux expansion at the SF-region:

$$\Delta_{X-\rho \text{ int}} \approx \sqrt{\Delta_{\text{mid-pl.}} b}$$

Criterion of ballooning stability near the separatrix and SF area can be derived as follows. Using the magnetic topology shown in Fig: 4 the criterion for ballooning stability can be written as [5]:

$$\left. \frac{dP}{d\rho} \right|_{X-\rho \text{ int}} < \text{Const.} \cdot \frac{B^2 R}{q^2} \frac{b}{\sqrt{\rho}}, \quad (2)$$

or as:

$$\frac{4\pi q^2 R}{B^2} \left. \left(\frac{dP}{dr} \right) \right|_{\text{mid-plane}} > \sqrt{\frac{b}{\Delta}} \quad \text{or} \quad \left. \left(\frac{dP}{dr} \right) \right|_{\text{mid-plane}} > \frac{b}{P_0} \left(\frac{B^2}{4\pi q^2 R} \right)^2 \quad (3)$$

Where

$$\alpha \equiv \frac{4\pi q_\pi^2 R}{B^2} \left(\frac{dP}{dr} \right) \Big|_{mid-plane} > \frac{b}{P_0} \left(\frac{B^2}{4\pi q^2 R} \right)$$

Here the safety factor q was taken as: $q_\pi(\rho) \equiv q_\pi(0.1) = q_{95} / 3$

Neglecting the dependence on shear and assuming that P_0 is the pedestal pressure, one can find that:

$$\frac{\partial P}{\partial r} \Big|_{x-\rho_{int}} \approx \frac{P}{\sqrt{\Delta_{mid.-pl.}} b} < Const. \frac{B^2}{4\pi R q_s^2} s(q, k, \varepsilon, \delta), \quad \text{where } q_s = q_{95} \frac{\pi}{6} \ln(4\pi / \rho),$$

The difference in magnetic potential well for the SF case and normal X-point configurations are shown in Fig.5

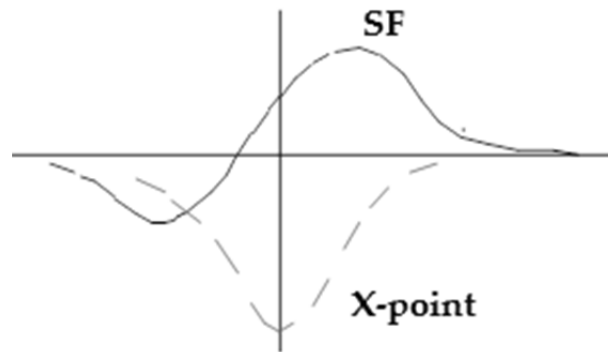


Fig. 5 Magnetic well in case of SF and normal X-point configurations (dashed line)

One can conclude that due to different magnetic well inside and outside in the case of SF configuration the critical pressure gradient inside is less than outside. From Ballooning MHD mode stability ($\Delta_{mid.-plane} \sim \lambda \rho_\theta$) follows the edge density limitation:

$$n_{[10^{20} m^{-3}]} < 1,15 \left(\frac{I_{M4}}{\pi a^2} \right)^{3/2} \left(\frac{1}{T_{100}^{3/4}} \right) \left(\frac{R}{a} \right)^{3/4} \frac{A^{1/4} \sqrt{k}}{(1+k^2)^{3/4}} \lambda a s(k, \delta, \varepsilon q)$$

From the other side, the requirements to avoid thermal (MARFE) stability

$$\chi_{||}^0 T^{5/2} / Z_{eff} R^2 q^2 > n^2 C_z \bar{L}_z, \quad \text{where } \bar{L}_z = (2L - TdL / dT)$$

electron density at the separatrix mid-plane has to be

$$n_{[10^{20} m^{-3}]} = \frac{45(T_{100})^{7/4}}{qR} \frac{1}{\sqrt{\bar{L}_z C_z Z_{eff}}}$$

Thermal - Ballooning stability diagram is shown in Fig.6

Thermal instability (MARFE) is suppressed for higher temperature range, whereas the ballooning modes are unstable for higher pressure. Critical density can for perturbation in inner region (see Fig.6) reads:

$$n_{[10^{20} m^{-3}]} = 1.15 \left(\frac{I}{\pi a_m^2} \right) \frac{a_m^{0.175} R^{-0.3}}{\left(\sqrt{Z_{eff} \alpha L_{33} C_Z q_{95}^2} \right)^{3/10}} \left(\frac{A^{1/4} (s \sqrt{k \lambda})}{(1+k^2)^{3/4}} \right)^{7/10}$$

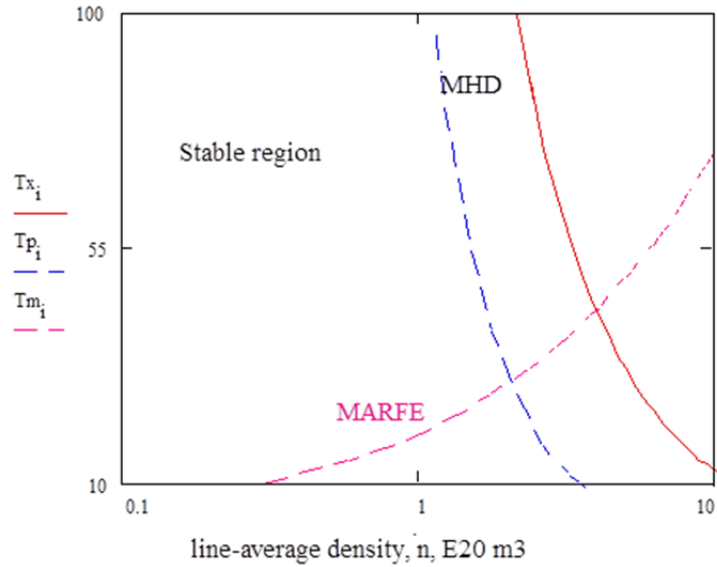


Fig.6 Stability diagram for DEMO. For expecting densities at the edge (>1020 m-3) and temperatures above several keV the SF divertor will be unstable against the coupled ballooning-thermal modes.

and for outer region

$$n_{[10^{20} m^{-3}]} = 0.67 \left(\frac{I}{\pi a_m^2} \right)^{7/9} \frac{1}{\left(Z_{eff} \alpha L_{33} C_Z q_{95}^2 \right)^{1/9}} \left\{ \frac{A (s \lambda)^2}{\sqrt{\frac{R}{a}} (1+k^2)} \right\}^{7/18}$$

6.3 Conclusion

The analysis of a density limit in tokamaks for DEMO configuration is done for up-down symmetric equilibrium of SF configuration. It is shown that the ideal ballooning mode significantly change their feature. The ballooning perturbation inside the configuration is much weaker, than outside. due to the stabilizing effect of a favorable magnetic curvature in inner side. The upper attainable density exhibits almost linear dependence on the plasma current similar to the Greenwald limit. However it differs from the Greenwald value:

at low temperatures ($<100\text{eV}$) this limit is less restrictive. A weak dependence on impurity content was obtained. However the influence of impurities can emerge through the resistive modes, which in turn can trigger the ideal modes.

Acknowledgements

This work, supported by the European Communities under the EFDA contract of Association between EURATOM and Karlsruhe Institute of Technology (KIT), was carried out within the framework of the European Fusion Development Agreement. The views and opinions expressed herein do not necessarily reflect those of the European Commission.

6.4 References

- [1] Lipshultz B., J. Nucl. Mater. 1458~147, (1987) 15.
- [2] Porter G., Bulletin of the American Physical Society, 40 (1995) 1693.
- [3] Ryutov D.D. Phys. Plasmas 14, 064502 (2007); doi: 10.1063/1.2738399
- [4] Zohm H.: On the minimum size of DEMO, Fusion Science and Technology 58
- [5] Pogutse O. et al., EPS, 1995

7 Plasma Boundary Modelling: Model of the SOL and Divertor transport

Yu. Igitkhanov,

Task: WP13-PEX-01-T01-02/KIT/PS

Final EFDA report 2013

7.1 Introduction

The main purpose of this report is the development of analytical transport models of the edge tokamak plasma, suitable for implementation into the integrated code TOKES and in perspectives for implementation into System integrated Code for predictive modelling of the fusion reactor DEMO. The tokamak edge plasma in reactor configurations is expected to be rather thin in most and outmost areas (adjacent to the last closed magnetic surface) with strong radial plasma gradients inside the separatrix and the area outside the separatrix, a scrape-off layer (SOL), with open magnetic field lines, terminated at the divertor plates and limiters. The region beyond the separatrix plays an important role because it serves as a shield, protecting the wall from the hot plasma and bulk plasma from the penetration of impurities and because it is mostly affected by transients. The transport model, proposed here, provides plasma density, temperature and velocity distribution along and across the magnetic field lines in bulk and the edge plasma region. It describes the dependence of temperature and density at the separatrix on the plasma conditions at the plate and the efficiency of the divertor operation, depending on power and particle sources. The calculation gives eventually the power and particle loads on the divertor plates and side walls.

7.2 2D fluid equations for SOL and divertor plasma in TOKES

We are considering a 2D orthogonal coordinate system in the rectangular SOL domain with the x-axes across and the y-axes along the magnetic field lines (See Fig. 1). In tokamak configuration plasma near the wall has in general a complex curvilinear configuration. The magnetization of the plasma and relatively narrow boundary region, however, makes it possible to “straighten out” the separatrix and, in some approximation, to treat the problem in a rectangular geometry (Fig.1). If there is substantial uncertainty regarding the transport in radial direction, the effects of the curvature and of the variation of the poloidal magnetic field along B can be simply ignored. The SOL width, Δ_{sol} , is specified as a distance from the first wall to the separatrix and is much less than a minor radius, a . The plasma is

assumed to be in steady state quite dense and cold (excluding transients), and is described by the system of hydrodynamic equations. The following hydrodynamic equations for density, n , momentum and energy in the SOL plasma are employed [1]:

$$\frac{\partial n}{\partial t} + \frac{\partial}{\partial x} nV_x = - \frac{\partial}{\partial y} (nV_y) + n(\langle \sigma V \rangle_{ion} N_0 - \alpha_{rec} n - \alpha_3 n^2) \quad (1)$$

$$nV_x = -D_B(T) \frac{\partial n}{\partial x} \quad (2)$$

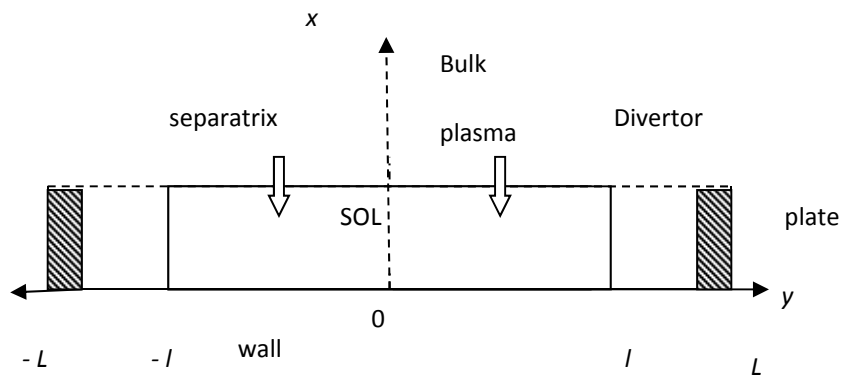


Fig. 1 The computational domain for the SOL and divertor region.

where N_0 is the neutral gas density, $D_B(T)$ is the Bohm diffusion coefficient, (σV) is the ionisation rate, The recombination rate α has the form $\alpha = \alpha_{rec} + n\alpha_3$, where α_{rec} and α_3 are the radiative and three-body recombination rates, respectively. The momentum and energy equations read:

$$m_i \frac{\partial nV_y}{\partial t} + \frac{\partial}{\partial y} n(m_i V_y V_y + 2T) + \frac{\partial}{\partial x} (m_i nV_y V_x) = \frac{\partial}{\partial y} \left(\eta_{yy} \frac{\partial V_y}{\partial y} \right) + Q_p \quad (3)$$

$$\begin{aligned} & \frac{\partial}{\partial t} \left(3nT + \frac{m_i n (V_x^2 + V_y^2)}{2} \right) + \frac{\partial}{\partial x} \left(5nT + \frac{m_i n (V_x^2 + V_y^2)}{2} \right) V_x + \\ & + \frac{\partial}{\partial y} \left(5nT + \frac{m_i n (V_x^2 + V_y^2)}{2} \right) V_y + \frac{\partial}{\partial y} \chi^0 T^{5/2} \frac{\partial T}{\partial y} + \frac{\partial}{\partial x} n D_B(T) \frac{\partial T}{\partial x} = Q_\varepsilon \end{aligned} \quad (4)$$

$$Q_p = -m_i n V_y \left[(\alpha_{rec} + \alpha_3 n^2) + v_{cx} \right] \quad (\text{The velocity of neutrals is neglected}) \quad (5)$$

$$Q_\varepsilon = -Q_{rad} - (I_i + \varepsilon_*) n N_0 \langle \sigma V \rangle_{ion} - (\varepsilon_{tot} \alpha_{rec} + (\varepsilon_{ion} - I) n \alpha_3) n^2 \quad (6)$$

Here $T \equiv T_e = T_i$, η_{yy} is the viscosity and χ^0 is the Spitzer-Harm conductivity coefficient along B (for one eV), D_B is the radial diffusion coefficient (in calculation is taken as $1\text{m}^2/\text{sec}$. though, generalization to functional Bohm coefficient is straightforward). Particle source, nN_0S_0 is due to ionization of neutrals, $S_0 = \langle \sigma V \rangle_{ion}$. The momentum sink, Q_p , is due to charge exchange with cold neutrals, N_0 , and the recombination. The energy sink, Q_ε , is due to radiation, ionization and recombination of neutrals., Neutrals are currently given arbitrary by specifying a distribution of atoms in divertor.

Here $\tau_{cx} = 1/N_0 \langle \sigma_{cx} V_i \rangle$ is the charge exchange collision time and Q_{rad} are the radiation losses for cold neutrals. In the energy loss term ε^* is the average excitation energy, $\varepsilon_{tot} = \varepsilon_i + \varepsilon_e$, where:

$$\varepsilon_i = \left(\frac{3}{2} T_i + \frac{m_i (V_y^2 + V_x^2)}{2} \right) n_i, \quad \varepsilon_e = \left(\frac{3}{2} T_e \right) n_e, \quad Q_{rad} = N_0 n L_H \quad (7)$$

and L_H is the cooling rate for hydrogen radiation, I is the ionization potential.

The following improvements are foreseen in near future:

- 1) separation of electron and ion temperatures, $T_e \neq T_i$,
- 2) appropriate model of the neutral atoms (self-consistent calculation),
- 3) equations for realistic curvilinear geometry.
- 4) the terms with parallel current along the magnetic field lines will be added
- 5) to include terms associated with impurities

7.3 Boundary conditions

The 2D fluid equations are required initial and boundary conditions at the computation boundaries. As initial conditions, density, temperature and velocities are taken from the 1D analytical profiles along the B and exponential across the SOL. Since we are looking for stationary solution, this choice is unimportant. The kinetic effects in boundary conditions are neglected and all transmission coefficients derived assuming a half Maxwellian function for the incident particles. We also neglect here the influence of impurities on the boundary parameters. One can distinguish five boundaries: at the separatrix, in private zone region, at the divertor plates and at the first wall.

Input particles, Γ and heat, $Q_e = Q_i = Q$ fluxes are specified at the separatrix:

- Separatrix between the SOL and core: $x = 1$ ($r = \Delta_{sol}$), $-l \leq y \leq l$

$$q_x = -nD_B \left. \frac{\partial T}{\partial x} \right|_{x=1; -d \leq y \leq d} + 5nTV_x = Q / S_{sep} \quad (8)$$

$$nV_x = -D_B \left. \frac{\partial n}{\partial x} \right|_{x=1; -d \leq y \leq d} = \Gamma / S_{sep} \quad (9)$$

- Divertor & private zone boundary: $x = 1$ ($r = \Delta_{sol}$), $|-L| \leq y \leq |L|$

$$q_x = -nD_B \left. \frac{\partial T}{\partial x} \right|_{x=1; |-L| \leq y \leq |L|} = 2(1-\alpha)nV_T T \quad (10)$$

$$\Gamma_x = -D_B \left. \frac{\partial n}{\partial x} \right|_{x=1; |-L| \leq y \leq |L|} = \frac{1}{4}(1-\alpha)V_T n \quad (11)$$

- Divertor plates: $y = \pm L$ $0 \leq x \leq 1$

$$-\chi_0 T^{5/2} \frac{\partial T}{\partial y} = 2T\Gamma_y \quad (12)$$

$$\Gamma_y \equiv nV_y = \frac{1}{4}(1-R)nc_s(T) \quad (13)$$

$$V_y = c_s(T), \quad T = T_w \quad (14)$$

where T_w is the wall temperature, $c_s(T)$ is the sound speed.

- Private region: $x = 1 \quad -L \leq y \leq -l; \quad l \leq y \leq L$

$$q_x \equiv -TD_{Bohm} \frac{\partial n}{\partial x} = 2(1 - \alpha)nT \cdot c_s(T) \quad (15)$$

$$\Gamma_x \equiv -D_{Bohm} \frac{\partial n}{\partial x} = \frac{1}{4}(1 - \alpha)n \cdot c_s(T) \quad (16)$$

where α is some reflexion coefficient ≤ 1 , which describes the ratio of reflected back from private region particles.

- Wall: $x = 0, \quad -L \leq y \leq +L$

$$\text{We assume } n = 0, T = 0 \quad (17)$$

The boundary conditions at the divertor plate can be generalized by assuming that the distribution function at the boundary is a one-directed and somewhat shifted Maxwellian function for ions (due to the acceleration in the electric pre-sheath, eq) and truncated at some velocity double side Maxwellian function for electrons (because of a cut-off in the retarding electric field). The boundary conditions at the plate then can be obtained by equating the fluid particle and energy fluxes to kinetic ones:

$$\left(\frac{5}{2}nV_sT_e + q_e\right) = f_eT_enV_{Te} \quad (18)$$

$$\left(\frac{m_iV_i^2}{2} + \frac{5}{2}T_i\right)nV_i + q_e = f_iT_inV_{Ti} \quad (19)$$

$$(m_inV_i^2 + nT_i + nT_e - \eta_i \frac{\partial V_i}{\partial y}) = f_{pe}T_en + f_{pi}T_in \quad (20)$$

where

$$f_e = 2 + \varepsilon \quad (21)$$

$$f_i = \frac{e^{-M_1^2}(2 + M_1^2) - \sqrt{\pi}M_1\left(M_1^2 + \frac{1}{2}\right)\text{Erf}(-M_1)}{G(M_1)}. \quad (22)$$

$$f_{pi} = \frac{2\sqrt{\pi}M}{G(M_1)} \cdot \left\{ \frac{M_1}{\sqrt{\pi}} e^{-M_1^2} + \left(M_1^2 + \frac{1}{2}\right)\text{Erf}(-M_1) \right\} \quad (23)$$

$$f_{pe} = \frac{2\sqrt{\pi}M}{G(M_1)} \cdot \left\{ -\sqrt{\frac{\varepsilon}{\pi}} e^{-\varepsilon} + \frac{1}{2} \text{Erf}(-\varepsilon) \right\} \quad (24)$$

Here $M=V_i/V_{Ti}$ where V_i is the fluid velocity along B at the plate and V_{Ti} is the ion thermal velocity;

$$\text{Erf}(x) = \frac{2}{\sqrt{\pi}} \int_{-\infty}^x e^{-t^2} dt$$

The parameter M_1 is equal to M if $V \geq C_s$, while at $V \leq C_s$, it is found from the condition

$$\int_0^{\infty} F_i(M_1) V dV / \int_0^{\infty} F_i(M_1) dV = C_s$$

where F_i is boundary distribution function for ions, $u = V/V_{Ti}$

$$F(M_1)_i = \frac{c_i \mathcal{G}(u)}{\sqrt{\pi} V_{Ti}} \exp \left\{ - (u - M_1)^2 \right\}$$

$\theta(x)$ is the Heaviside function and $C_s = (5(T_e + T_i)/3m_i)^{1/2}$ is the sound velocity. The dimensional potential of the sheath $\varepsilon = e\phi/T_e$ is found from quasineutrality condition [2]:

$$\varepsilon = \frac{\ln \sqrt{\frac{m_i T_e}{m_e T_i}} \text{Erf}(-M_1)}{G(M_1) \text{Erf}(-\sqrt{\varepsilon})} \quad (25)$$

$$\text{where } G(M_1) \equiv e^{-M_1^2} + \sqrt{\pi} M_1 \text{Erf}(-M_1) \quad (26)$$

Note that the plasma parameters may have a discontinuity at the boundary, but the fluxes remain continuous. The value of the electric potential in pure plasma at the plate is about $e\phi \sim 3.5 T_e$ in absence of current flow to the plate and electron emission. But this potential could considerable increase in non-stationary case, when the material surface becomes due to erosion not even.

7.4 Kinetic effects in the SOL plasma

One of the factors limiting the applicability of the hydrodynamic approach is the effect of the suprathermal particles upon the parallel heat conductivity and viscosity. Even when the conditions of hydrodynamics are strongly satisfied (e.g. the mean free path of particles are small compare with the SOL length), the expressions for the parallel heat conduction and viscosity coefficients turn out to be wrong. This is related to the fact that hydrodynamic fluxes are higher order moments and are determined mainly by suprathermal particles for which the hydrodynamic approximation turns out to be violated. When this occurs, the heat and momentum fluxes become non-local in their nature. It is shown [19] that the non-local representation for fluxes naturally follows from the equations for higher order

moments of the distribution function, provided that the spatial derivatives of these moments with respect to coordinates are retained. This allows one to use differential equations for moments and their derivatives instead of complicated integral expressions for the flux in numerical calculations. In simulation of kinetic effects a simplified approach is often used, assuming the heat flux to be constrained from above by the quantity

$$q_e = \frac{q_{SH} \cdot q_{kin}}{q_{SH} + q_{kin}}, \quad (27)$$

where $q_{kin} = FLF \cdot 2nTV_{Te}$

Here $FLF = 0.1-0.3$ is a flux limiting factor which is found either from experiments or from the results of numerical solution of a kinetic equation [20-22]. Unfortunately, the great uncertainty found in the experimental data does not allow one to make a quantitative conclusion about the value of FLF . As a non-local approach, FLF increases the upstream plasma temperature and reduces the density, whilst not changing significantly the plasma parameters in the vicinity of the plate. However, with the introduction of the FLF the transport remains local. Such an approach does not represent all the features related to the nature of the non-local transport. Furthermore, the applicability of the integral expression is limited to cases with low parallel plasma gradient, where a strong anisotropy in the particle distribution function can be neglected. In cases of large temperature gradient the main contribution to transport is supplied by the "tail" particles. These hot electrons can reach the divertor plate and, essentially produces an increase in the sheath potential (see Fig. 2) that can result in increased plate erosion. For a higher sheath potential, however, the energy transfer ability of each electron-ion pair on the plate is increased. The implication is that the plasma temperature near the plate may be less than that predicted by fluid modelling, thus reducing sputtering by hot ions to some extent. In summary of the above arguments, one can say that the non-local transport redistributes the fluxes over the thermal layer, reducing the peak power load. Therefore existing hydrodynamic models probably give pessimistic values of heat loading and local plasma temperature at the divertor plate. The kinetic effects can noticeably affect the transport of impurities in the divertor, in particular that of helium. The localisation of impurities is determined by the competition of many forces, including the ion thermal force. Under ITER divertor plasma conditions one can expect a reduction in the ion thermal force in comparison with the hydrodynamic limit [16, 17]. In the case of helium ions this reduction is approximately equivalent to a reduction of the thermal force coefficient by a factor of two to three.

Summarize, we are suggesting the following kinetic correction in fluid equation. Since electrons are predominantly deviate from hydrodynamic limit the local expression for parallel heat conductivity in energy equation, $q_{e,SH}(y) = -\chi_{e,SH} dT_e/dy$ can be replaced by:

$$q_e(y) = \int_{-L}^{+L} G(y - y') \cdot q_{e,SH}(y') dy' \quad (28)$$

where

$$G(y - y') \approx \frac{1}{2\lambda(y')} \exp\left(-\left|\int_{y'}^y \frac{d\eta}{\lambda(\eta)}\right|\right) \tag{29}$$

Here

$$\lambda(y) = V_{Te}(T_e^*) \cdot \tau_{ei}(n, T_e^*), \quad T_e^* \approx 3.8 \cdot T_e$$

$$\lambda(y) = V_{Te}(T_e^*) \cdot \tau_{ei}(n, T_e^*)$$

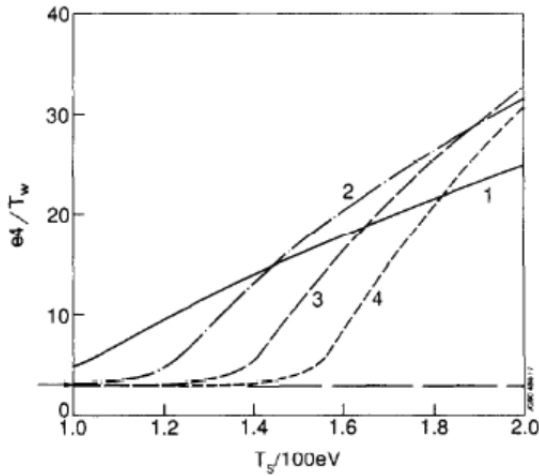


Fig. 2 The influence of hot particles on the sheath potential $e\phi/T_w$ versus temperature T_s , and density n_s at the separatrix:

- (1) $n_s = 1 \cdot 10^{13} \text{ cm}^{-3}$, (2) $n_s = 2 \cdot 10^{13} \text{ cm}^{-3}$,
- (3) $n_s = 3 \cdot 10^{13} \text{ cm}^{-3}$, (4) $n_s = 4 \cdot 10^{13} \text{ cm}^{-3}$

and T_w is, the temperature at the plate.

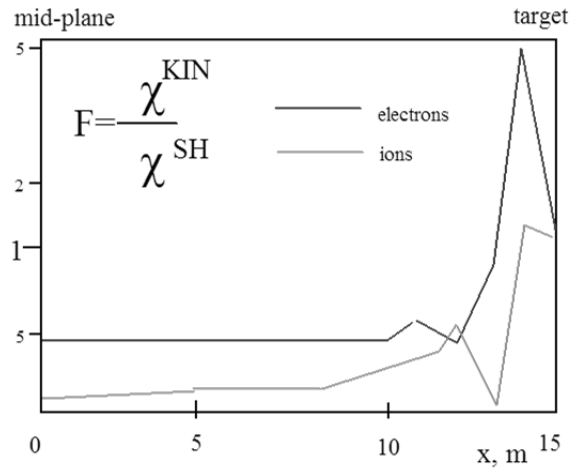


Fig. 3 Kinetic correction to heat conductivity vs. distance along B; here $F = 1 / FLF$; Heat flux near the plate increases several times due to the contribution of supra-thermal particles.

Analyse of kinetic correction of fluid equations shows, that the supra-thermal particles are largely responsible for the parallel transport in boundary plasma. Non-locality produces two kinds of effect on the heat flow: reduction in the hot region of the SOL and enhancement in the cool region near the plate. Reduction of the heat conductivity results in stronger temperature gradients and, this, in combination with pressure balance along B reduces upstream plasma densities. Supra-thermal particles can considerable enhance the sheath potential and increase neutral ionization and excitation rates. An efficient numerical procedure for kinetic correction to 2D fluid includes the following corrections:

- 1) the flux limit factors for electron and ion heat flux along B or
- 2) the introduction of non-local heat flux expression (which changes energy equation to integer-differential and requires another numerical solver).

7.5 Model for H-Mode Pedestal formation

During the L to H-mode transition, when input power Q exceeds some critical value, Q_{LH} [3]:

$$Q_{LH} = 0.084 \cdot \bar{n}^{0.73} B_T^{0.74} S^{0.98} M^{-1} \quad (30)$$

a strong pressure gradient forms at the edge because of the turbulent transport suppression outwards beyond some radial position. This pressure gradient separates the anomalous core and the neoclassical pedestal region, which spreads from the top of the pedestal up to separatrix and is marginally stable. There are two suppression factors: 1) proportional to $1/(1+k(\omega_{ExB}/\gamma)^2)$, where γ is an increment of the ion temperature gradient (ITG) instability and ω_{ExB} is ExB shearing rate, and 2) due to increase of edge (e.g. bootstrap) current and, consequently, the magnetic shear at the edge. Since $\gamma \sim 1/s$, increase of shear suppresses the turbulence. We assume here, that the turbulent transport is mainly suppressed by $\mathbf{E}_r \times \mathbf{B}$ velocity shear at the plasma edge. This means, that the radial transport coefficients for thermal conductivity and particle diffusion drop down to subdominant (neoclassical) value:

$$\chi_{e,i} = \chi_{e,i}^{an} \cdot \left\{ 1 + k \cdot \left(\frac{\omega_{ExB}}{\gamma(s)} \right)^2 \right\}^{-1} + \chi_{e,i}^{neo} \quad (31)$$

$$D_{e,i} = \chi_{e,i} \cdot n \quad (32)$$

Here $\chi_{e,i}^{an}$ is the anomalous conductivity, which dominates in the core region, where $\gamma > \omega_{ExB} \sim 0$. Within pedestal region, where $\gamma < \omega_{ExB}$, anomalous transport is suppressed by the magnetic shear s and ExB shear. In this region the dominate transport is neoclassical (second term in (4)). Here k is some fitting factor ~ 1 . The anomalous conductivity is

$$\chi_{e,i}^{an} = \chi_{GB} \approx \rho_{tor}^2 C_s / s^\varepsilon \Delta_{ped} \quad (33)$$

and

$$\gamma_s = \chi_{GB} k_\perp^2 \approx \rho_{tor}^2 C_s k_\perp^2 / s^\varepsilon \Delta_{ped} \quad k_\perp^2 \rho_{tor}^2 \approx 0.03 \quad (34)$$

where γ is the growth rate of a gyro-Bohm type instability. Expression for shearing rate ω_{ExB} reads as:

$$\omega_{ExB} = \frac{\partial}{\partial r} \left(\frac{E_r}{B} \right) \approx \frac{\partial}{\partial r} \left(\frac{\nabla p}{n \cdot B} \right) \approx \rho_{tor} C_s / \Delta_{ped}^2 \quad (35)$$

Here we assume, that $E_r \sim \text{grad } P$ and $\text{grad } P \sim nT/\Delta_{ped}$. The width of the pedestal region, Δ_{ped} , can be defined as a radial position inside the separatrix, where turbulence is suppressed by the combined

effect of the magnetic and $\mathbf{E} \times \mathbf{B}$ shear (see Figs. 4). The pedestal width depends on the toroidal Larmor radius ρ_{tor} and the magnetic shears s , and can be expressed as:

$$\Delta_{ped} = \rho_{tor} \cdot s^2 \quad \rho_{tor} = 3.23 \cdot 10^{-3} \cdot B_T^{-1} Z^{-1} \sqrt{A \cdot T_i} \quad (36)$$

Here B_T is the toroidal magnetic field in Tesla, A is the mass number, Z is the charge state, T_i is the ion temperature in keV, ρ is in m. The shear depends on radial position, but for simplicity sake it can be arbitrarily chosen at 95% flux surface.

The pedestal width Δ_{ped} , be define as a radial position where turbulence is suppressed by magnetic and electric shear.

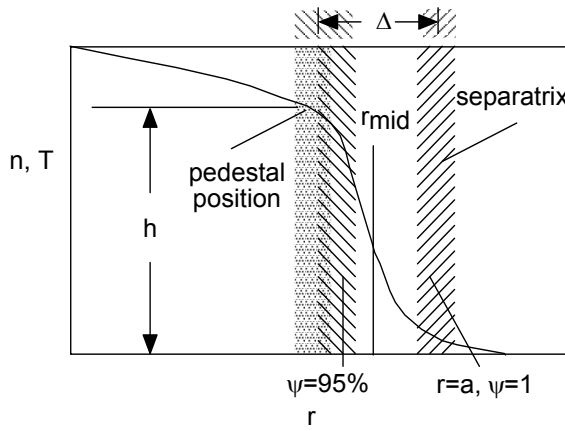


Fig. 4 Definition of pedestal width.

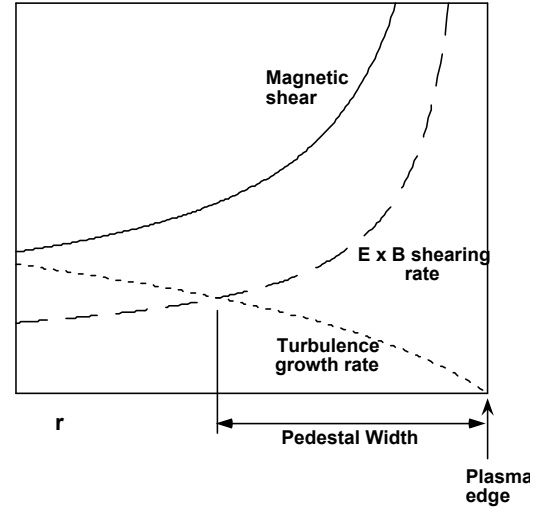


Fig. 5 Pedestal width is defined at radial position where turbulence is suppressed by magnetic and electric shear.

The radial transport suppression in TOKES, which describes the L to H transition is implemented (taking into account threshold dependence of the H-mode onset on input power) as

$$\chi = \frac{\chi_{an}}{1 + \mu\theta(Q - Q_{LH})(s^2 \rho_i / k_{ped})^2} + \chi_{neo} \quad (37)$$

$$\Delta_{ped} \propto \mu \rho_{tor} s^2 k_{ped} \approx p / \nabla p$$

For ITER Q_{LH} value is estimated about 60MW.

7.6 Conclusions

The main purpose of this report is the development of analytical and numerical transport models of the tokamak plasma, suitable for implementation into the integrated transport code. The tokamak edge plasma in reactor configurations is expected to be rather thin outmost area with strong radial plasma gradients inside the separatrix and the area outside the separatrix, a scrape-off layer (SOL), with open magnetic field surfaces, terminated at the divertor plates. The region beyond the separatrix plays an important role because it serves as a shield, protecting the wall from the hot plasma and bulk plasma from the penetration of impurities and because it is mostly affected by transients. The transport model, proposed here, provides plasma density, temperature and velocity distribution along and across the magnetic field lines in bulk and the edge plasma region. It describes the dependence of temperature and density at the separatrix on the plasma conditions at the plate and the efficiency of the divertor operations, depending on power and particle sources. The calculation gives eventually the power and particle loads on the divertor plates and side walls. The following tasks have been completed:

The 2D transport model for the SOL have been prepared and implemented into the TOKES code. This model is suitable for description of stationary plasma processes in the edge tokamak region.

The model of pedestal formation at the plasma edge in H-mode operation was implemented in TOKES. The model based on power scaling for L to H transition and includes the mitigation of turbulence at the edge once the flowing power exceeds the H-mode onset threshold.

The boundary conditions for fluid equations at the divertor plates and at the main chamber wall are formulated and implemented into the integrated code.

Analyses of available experiments and benchmarking with simple analytical solutions in respect to SOL transport phenomena will be provided.

Acknowledgements

This work, supported by the European Communities under the EFDA contract of Association between EURATOM and Karlsruhe Institute of Technology (KIT), was carried out within the framework of the European Fusion Development Agreement. The views and opinions expressed herein do not necessarily reflect those of the European Commission.

7.7 Reference

- [1] Braginski S.I., Reviews of plasma physics (ed. Leontovich, M.A.), Vol. 1, Consultants Bureau, New York (1965).
- [2] Igitkhanov Yu., Kukushkin A., Pigarov Yu., Pistunovich V., Sov. J. Plasma Physics 12(1) Jan. 1986
- [3] ITER Physis Bases; Nucl. Fusion 39, (1999)

8 Modeling of Li layer behavior under ITER like ELM loads

Yu. Igitkhanov and B. Bazylev , KIT, Karlsruhe

Final Report on EFDA Task

Novel PFC material solutions / Liquid Metals, WP13-PEX-03B-T05-01/KIT/PS,

EC ref. number FU07-CT-2013-00054

Abstract. The main objective of this task is the modelling of Li surface erosion under ITER and DEMO Type I ELM high power loading. This includes 1) melting and evaporation of the Li surface, 2) molten layer flow and deformation caused by the magnetic fields and thermo emission current, 3) effect of shielding owing to the Li evaporation. The 3D version of the predictive code MEMOS has been employed. The behaviour of liquid metal both in a Capillary Porous System (CPS) structure and as free flowing films are considered. The influence of porous substrate (W) on the melt motion damage is investigated for heat loads accounting for the melt layer and Li vapour shielding effect. Calculations for the ITER conditions show that the CPS will not be very effective as a compensator of molten layer evaporation or removal under the ELM impact. Remaining liquid Li layer is estimated to be below $0.4 \mu\text{m}$ which could easily evaporate. Damage caused by $J \times B$ (volumetric) force and by tangential pressure (surface) force is taken into account. It is shown that for ITER and DEMO mitigated ELMs heat loads the vapour shield is not efficient. However, under expected conditions erosion, splashing and stability of liquid flow remains an issue and requires further investigation. Calculations for the DEMO conditions show that impact of unmitigated ELMs on Li surface will cause a dramatic level of erosion. Evaporation depth could exceed the molten layer thickness. For the mitigated ELM the evaporation becomes much smaller, however it still exceeds $0.15 \mu\text{m}$ per ELM. The deformation of the molten layer surface due to pressure gradient does not exceed $10 \mu\text{m}$ per one ELM. The CPS structure could work only in the case of mitigated ELMs. Up to now the impact of single ELMs under DEMO conditions is considered. Modelling of the surface erosion under multiple ELM impact has been completed for the JET case (see Bazylev et al., paper submitted to PSI 2014 conference). Similar calculation can be done for DEMO conditions. The further benchmarking of MEMOS results with experimental data is highly demanding.

8.1 Introduction

A predictive code MEMOS has been modified (and consequently validated against experimental results) in order to simulate heat removal under DEMO conditions by using the CPS. Modelling of the flow of liquid metals under the influence of strong magnetic fields and the associated heat transport under high

power loads is the main objective. As first step we simulate the behaviour of liquid metal both in a CPS structure and as free flowing films.

The expected damage of plasma facing components (PFC) made from refractory materials as well as from the liquid metals in CPS under tokamak transient energy loads is simulated numerically in the wide region of heat loads using 2D and 3D versions of the code MEMOS [1]. The code was successfully validated for the short pulses against experiments at QSPA-T (Troitsk, Russia) [2] and QSPA-kh50 (Kharkov, Ukraine) [3] facilities and long-time plasma loads against experiments at TEXTOR. Now 3D MEMOS is validated against melt motion experiments in JET-ILW—with ITER-like wall and in its 3D version describes a macro brush structure of PF surface.

Target heating by plasma and electron-beam impact takes into account the effect of plasma shielding by vapour cloud due the armour material evaporation. The Stefan problem including a surface evaporation, melting and re-solidification are described. Motion of the melted material is simulated by 2D/3D Navier-Stocks equation in the „shallow water “approximation. On the armour surfaces thermo-emission current and the temperature dependent thermo-physical properties of materials is taken into account. The simulation of the molten layer motion includes the driving forces like a gradient of plasma pressure (in the case of developed plasma shielding), the surface tension and $J \times B$ force caused by current flowing into the armour (hallo current or by thermo-emission current).

Recently we use in MEMOS calculation new specifications of Type I ELM power loads, envisaged for DEMO reactor plasmas [4]. The power load of unmitigated ELMs on the DEMO I case is estimated as $3\text{MW}/\text{m}^2$ and for the mitigated ELMs with about 33 times reduced amplitude like in ITER. The case of DEMO1 was considered, were the uncontrolled ELM peak deposition energy/deposition time to the divertor plate are $10\text{MJ}/\text{m}^2/1.2\text{ms}$. In the case of DEMO II peak deposition energy/deposition time to the divertor plate is $20\text{MJ}/\text{m}^2/1.2\text{ms}$. Pressurized water reactor (PWR) cooling conditions with about 150°C inlet water temperatures and pressure about 15,5MPa are used for the calculations.

8.2 Modelling of Li layer behaviour under ITER like ELM loads

The behaviour of Li layer on various porous substrates is investigated by using MEMOS code, which takes into account capillary porous system and Li layer recovery under transients (ELM) impact. Calculations were performed for the following conditions: the melt motion and the evaporation of Li film on impermeable tungsten substrate, the Li coating of 5-50 μm thickness on W bulk material and W capillary porous system. Previously the following reference parameters where assumed heat load, $Q = 0.1 \text{ MJ}/\text{m}^2$, the ELM pulse load time $\tau = 0.5 \text{ ms}$, the magnetic field $B = 5 \text{ T}$ and the tangential pressure in the range of 2×10^{-4} to 2×10^{-3} bar. The electric current component normal to the target surface is varied in the range 5-50 A/cm^2 and that the initial surface temperature is $T_0 = 30^\circ\text{C}$ (assuming that Li melts during the transient). The thickness of evaporation layer is investigated for the reference pulse duration and heat load ranged between 0.1 and $0.4 \text{ MJ}/\text{m}^2$. The applied force and the energy flux correspond to the rectangular pulse shape. The time shape of the pulse was simulated similar to that of a real ELM.

Significant evaporation starts at heat loads $\geq 0.2 \text{ MJ/m}^2$ (see Fig. 1). Strong plasma shielding forms above the Li layer thus preventing Li from intensive evaporation. For the reference heat load, the vaporization is negligible, and the melt motion only causes the melt layer damage. In calculations the effects of tangential plasma pressure and the $J \times B$ force on liquid Li motion were investigated as well as the dependence of the surface damage on the pulse shape. The effect of different Li thickness on the formation of crater was investigated. It is shown that surface craters are caused by the tangential pressure for different thickness of Li layer and after 3 ms from pulse trail (see Fig. 1 and 2). The capillary porous system is taken into account. In scenarios with $\Delta Li = 5 \text{ }\mu\text{m}$ removed melted materials from the crater bottom is recovered by the capillary forces from the W porous matrix and the thickness of liquid Li at the crater bottom remains about $0.4 \text{ }\mu\text{m}$.

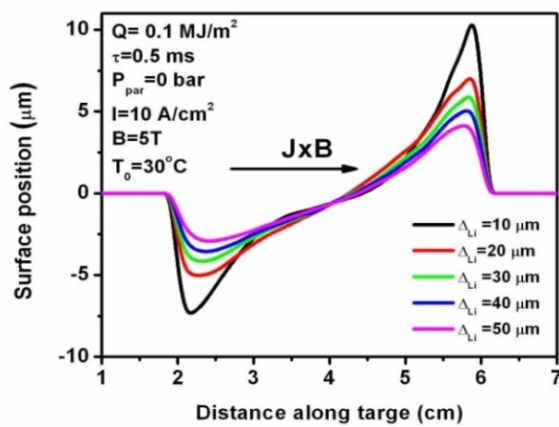


Fig. 1 Crater shape caused by $J \times B$ force on Li layer for different thickness of Li layer after 3 ms.

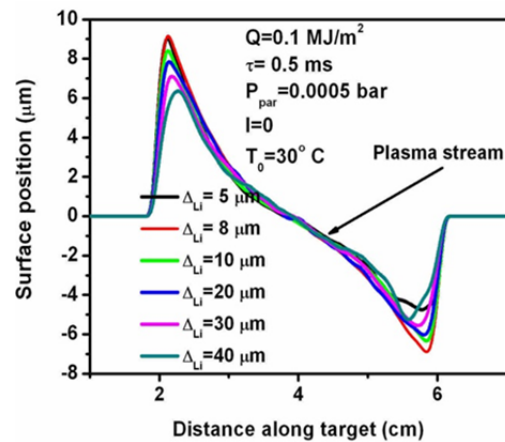


Fig. 2 Crater shape caused by tangential pressure on Li layer for different thickness of Li layer after 3 ms. Capillary porous system is taken into account.

The capillary porous system is taken into account. In scenarios with $\Delta Li = 5 \text{ }\mu\text{m}$ removed melted materials from the crater bottom is recovered by the capillary forces from the W porous matrix and the thickness of liquid Li at the crater bottom remains about $0.4 \text{ }\mu\text{m}$.

Calculations show that even small ELMs can completely remove Li away from W substrate.

The damage caused by $J \times B$ (volumetric) force strongly depends on layer thickness (due to effect of melt layer viscosity). Damage caused by tangential pressure (surface force) weakly depends on layer thickness. Under these conditions the vapor shield does not develop for investigated heat loads.

The first 3D MEMOS results of Li characteristics on the W sample with CPS after irradiation with plasma energy are presented here. In the Fig. 3 plasma heat loads in MW/cm^2 on the Li surface is shown. $3 \sim \text{m}$ of Li is coated on tungsten CPS. Target initial temperature was taken as 300 K. Impact energy $Q = 0.1 \text{ MJ/m}^2$ in maximum and pulse duration about 0.5ms. The pulse shape was taken as rectangular. The effect of vapor shielding is taken into account. A spatial energy pulse profile in Y direction (see Fig.1) was taken as half Gaussian with half width of 2 cm (similar to the typical ELM shape). In Z direction energy

pulse has Gaussian profile with half width of 7 cm. Two plasma pressure values in maximum 0.1 bar and 0.15 bar have been chosen.

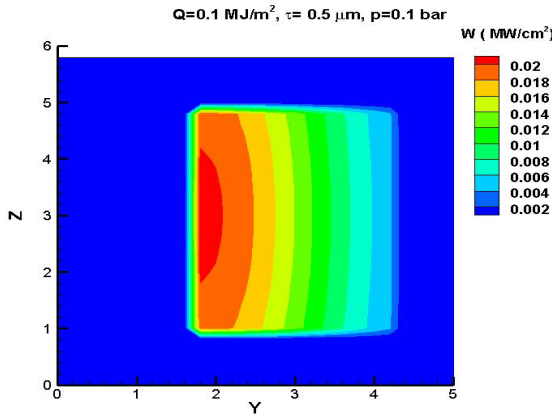


Fig. 3 Contour plot of plasma heat loads (in MW/cm²) on the Li surface, Q=0.1MJ/m², t=0.5msec, vapor pressure p=0.1bar. ITER like conditions.

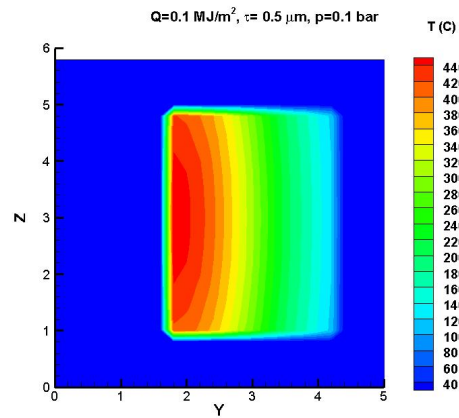


Fig.4 Contour plot of temperatures (in °C) on the irradiated surface for 0.1MJ/m² of energy load, evaporation depth 0.5μm, maximum pressure 0.1bar; low evaporation. ITER like conditions.

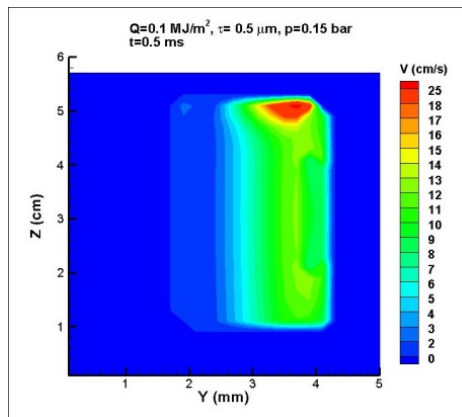
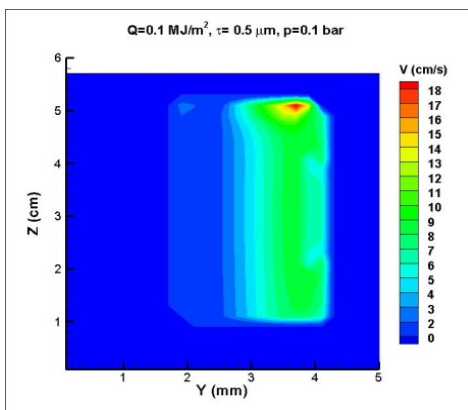


Fig.5 Contour plots of melt layer velocity along the irradiated surface for of energy load of 0.1MJ/m², evaporation depth 0.5μm and the maximum pressures 0.1bar on the left figure and 0.15bar on the right figure. Evaporation level is low. Gradient of plasma pressure generates the melt motion. ITER like conditions

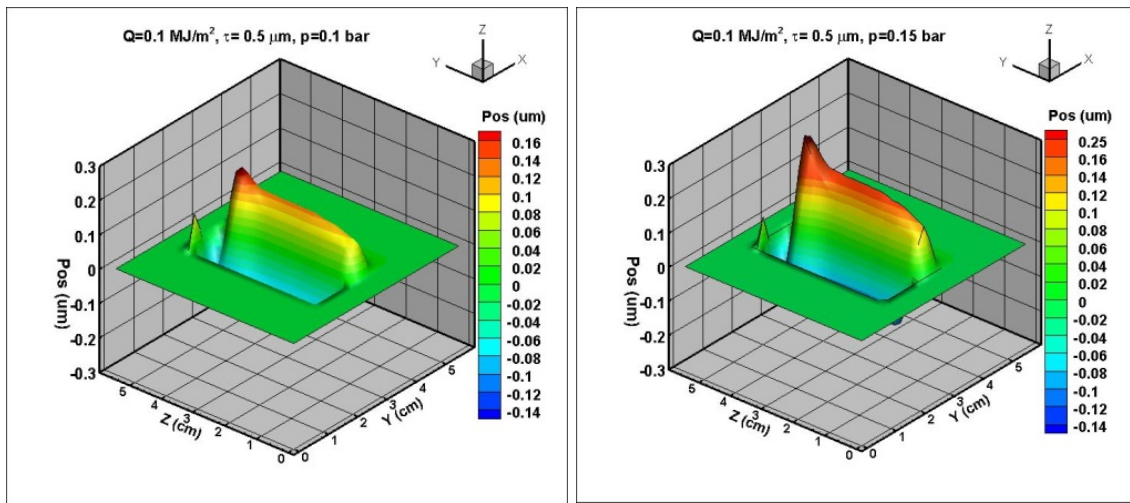


Fig.6 Final surface profile for two plasma pressure scenarios 0.1 bar (left) and 0.15 bar; (right) evaporation is at low level. Position in μm is plotted along the target surface.

8.3 Results of MEMOS calculation of Li melting under DEMO like ELM impact

Recently we use in MEMOS calculation new specifications of Type I ELM power loads, envisaged for DEMO reactor plasmas [4]. The power load of unmitigated ELMs on the DEMO I case is estimated as $3\text{MW}/\text{m}^2$ and for the mitigated ELMs with about 33 times reduced amplitude like in ITER. The case of DEMO1 was considered, were the uncontrolled ELM peak deposition energy/deposition time to the divertor plate are $10\text{MJ}/\text{m}^2/1.2\text{ms}$. In the case of DEMO II peak deposition energy/deposition time to the divertor plate is $20\text{MJ}/\text{m}^2/1.2\text{ms}$. Pressurized water reactor (PWR) cooling conditions with about 150°C inlet water temperatures and pressure about 15.5MPa are used for the calculations. In the case of mitigated like in ITER the ELMs power loads to the DEMO divertor have been taken in the range of $0.01\text{--}0.025\text{MW}/\text{cm}^2$. Fig. 7 shows the contour plot of evaporated Li for mitigated ELMs impact for ELM heat flux $Q=0.3\text{MJ}/\text{m}^2$, $\tau=1.2\text{msec}$, and incoming plasma and vapour pressure $p=0.25\text{bar}$, which correspond to DEMO1 conditions with Type 1 mitigated ELMs with reduced about 33 times amplitude. Fig. shows the final surface profile after the mitigated ELMs impact on the Li surface. Position in μm is plotted along the target surface. Erosion forms the hell and hill shape due to molten layer motion under pressure impact. Fig. 9 shows the contour lines of evaporated Li depth for mitigated ELMs impact (in μm) for the ELM load $Q=0.24\text{MJ}/\text{m}^2$ and deposition time $\tau=1.2\text{msec}$, The vapor pressure $p=0.2\text{bar}$ is assumed. The corresponding surface deformation after the ELM impact is shown in Fig. 10. With decreasing of ELM size, the Li erosion becomes smaller (see Figs. 11-12). Impact of unmitigated ELMs on Li layer is shown in Fig.13, where $Q=1.2\text{MJ}/\text{m}^2$, $\tau=1.2\text{msec}$ and plasma pressure $p=0.4\text{bar}$ are considered. It is shown, that evaporation of Li reaches almost 0.14mm even in the case of capillary porous Li supplies. This depth of erosion could even exceed the molten layer thickness. The resulting evaporation depth as a function of the DEMO ELM heat loads is summarized in Fig. 14. The evaporation of Li dramatically increases with

impact power and for heat loads above 1.2MJ/m^2 per ELM exceeds 0.1mm . Under those conditions the CP system does not work.

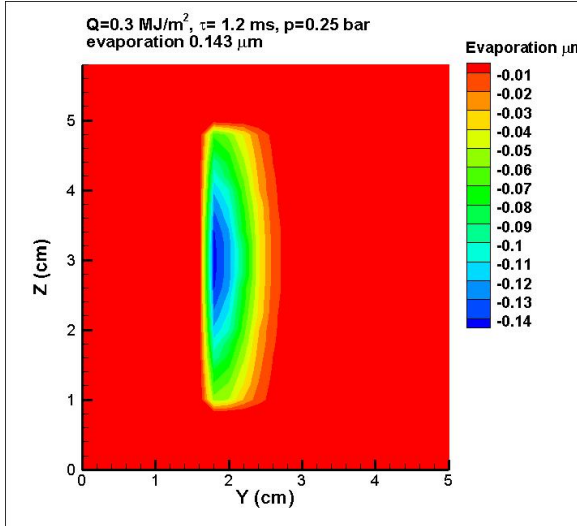


Fig. 7 Contour plot of evaporated Li for mitigated ELMs impact (in μm), $Q=0.3\text{MJ/m}^2$, $\tau=1.2\text{msec}$, vapor pressure $p=0.25\text{bar}$. DEMO like conditions.

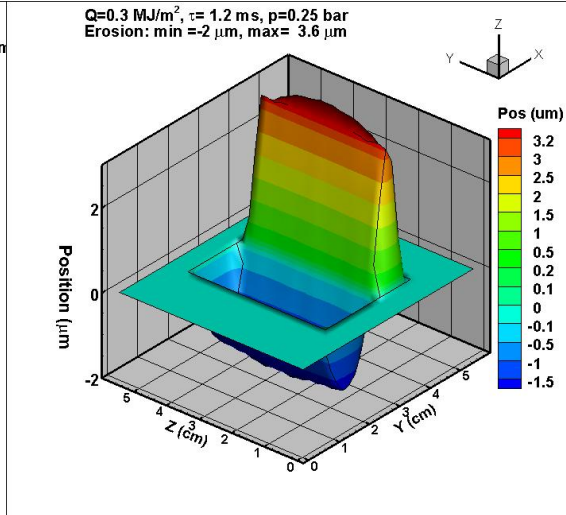


Fig.8 Final surface profile after DEMO mitigated ELMs impact. Position in μm is plotted along the target surface. Erosion level: $\text{min}=-2\mu\text{m}$, $\text{max}=3.6\mu\text{m}$.

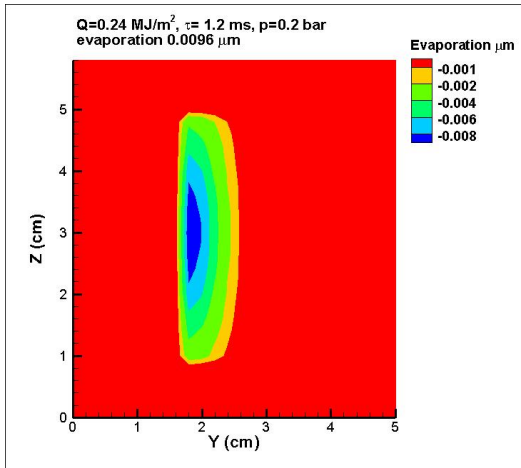


Fig. 9 Contour plot of evaporated Li for mitigated ELMs impact (in μm), $Q=0.24\text{MJ/m}^2$, $\tau=1.2\text{msec}$, vapor pressure $p=0.2\text{bar}$. DEMO like conditions. conditions. The mitigated ELMs.

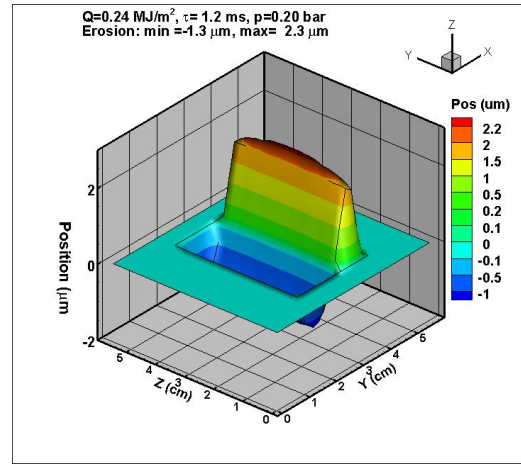


Fig.10 Final surface profile after DEMO mitigated ELMs impact. Position in μm is plotted along the target surface. $Q=0.24\text{MJ/m}^2$, $\tau=1.2\text{msec}$, vapor pressure $p=0.2\text{bar}$.

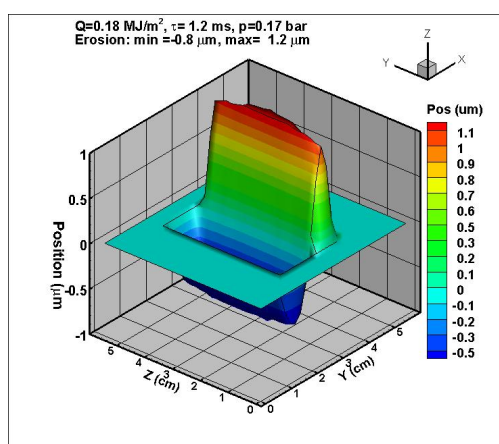


Fig.11 Contour plots of melt layer velocity along the irradiated surface for of energy load of $0.1\text{MJ}/\text{m}^2$, evaporation depth $0.5\mu\text{m}$ and the maximum pressures 0.17 . Evaporation level is low. Gradient of plasma pressure generates the melt motion. ITER like conditions

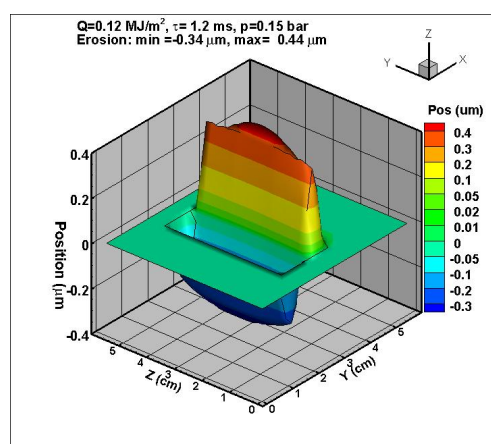


Fig.12 Contour plots of melt layer velocity along the irradiated surface for of energy load of $0.1\text{MJ}/\text{m}^2$, evaporation depth $0.3\mu\text{m}$ and the maximum pressures 0.15bar . Evaporation level is low. Gradient of plasma pressure generates the melt motion. ITER like conditions

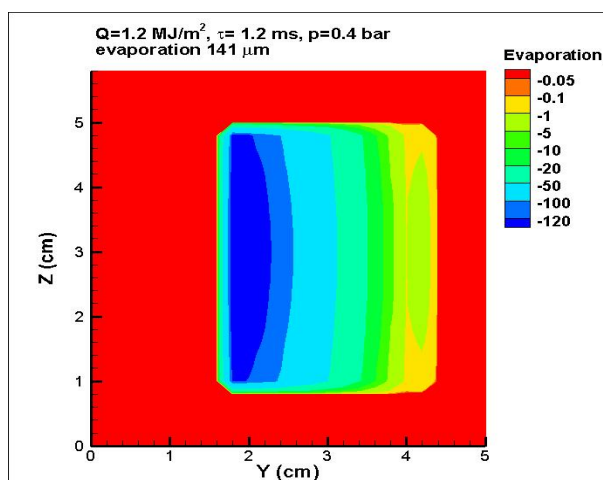


Fig. 13 Contour plot of evaporated Li for mitigated ELMs impact (in μm), $Q=1.2\text{MJ}/\text{m}^2$, $\tau=1.2\text{ms}$, vapor pressure $p=0.4\text{bar}$. DEMO like conditions. Conditions for unmitigated ELMs.

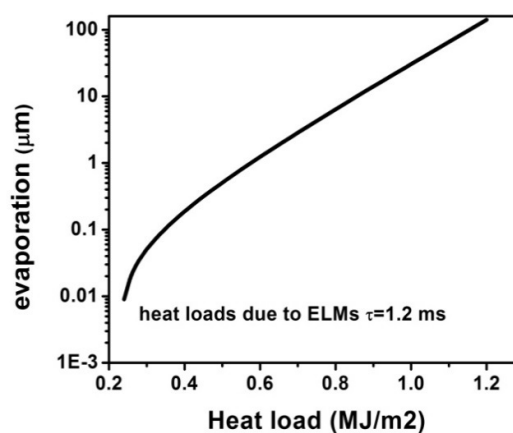


Fig. 14 Li Evaporation depth vs the ELM heat loads. The evaporation of Li dramatically increases with impact power and for heat loads above $1.2\text{MJ}/\text{m}^2$ per ELM exceeds 0.1mm . Under those conditions the CPS does not work.

plot of evaporated Li for mitigated ELMs impact for ELM heat flux $Q=0.3\text{MJ}/\text{m}^2$, $\tau=1.2\text{ms}$, and incoming plasma and vapour pressure $p=0.25\text{bar}$, which correspond to DEMO1 conditions with Type 1 mitigated ELMs with reduced about 33 times amplitude. Fig. shows the final surface profile after the mitigated ELMs impact on the Li surface. Position in μm is plotted along the target surface. Erosion

forms the hell and hill shape due to molten layer motion under pressure impact. Fig. 9 shows the contour lines of evaporated Li depth for mitigated ELMs impact (in μm) for the ELM load $Q=0.24\text{MJ}/\text{m}^2$ and deposition time $\tau=1.2\text{msec}$, The vapor pressure $p=0.2\text{bar}$ is assumed. The corresponding surface deformation after the ELM impact is shown in Fig. 10. With decreasing of ELM size, the Li erosion becomes smaller (see Figs. 11-12). Impact of unmitigated ELMs on Li layer is shown in Fig.13, where $Q=1.2\text{MJ}/\text{m}^2$, $\tau=1.2\text{msec}$ and plasma pressure $p=0.4\text{bar}$ are considered. It is shown, that evaporation of Li reaches almost 0.14mm even in the case of capillary porous Li supplies. This depth of erosion could even exceed the molten layer thickness. The resulting evaporation depth as a function of the DEMO ELM heat loads is summarized in Fig. 14. The evaporation of Li dramatically increases with impact power and for heat loads above $1.2\text{MJ}/\text{m}^2$ per ELM exceeds 0.1mm. Under those conditions the CP system does not work.

8.4 Conclusions

The lithium surfaces divertor concept allows one to increase the heat-flux exhaust capability by flowing the heated material to a cooling region and eventually out of the machine, and/or by being able to withstand a higher peak heat flux. In our calculation we investigate the impact of Type I ELM heat loads expected in ITER or in DEMO on erosion of Li divertor target. We investigate a molten layer distortion under different forces, acting on the molten layer. The 3-D version of MEMOS code is employed. The effect of porous substrate (W) on the melt motion damage is investigated for various heat loads, expected for transients. Calculations are taking into account the formation of Li vapour shielding. It is shown, that the CPS could not effectively compensate of molten layer evaporation or removal under ITER or DEMO ELMs impact.

In the case of ITER envisaged Type I ELMs heat loads the remaining liquid Li layer is estimated to be below $0.4\ \mu\text{m}$ which could easily evaporate under high heat loads. Damage caused by JxB (volumetric) force impact strongly depends on layer thickness (due to effect of melt layer viscosity). Damage caused by tangential pressure (surface force) weakly depends on layer thickness. Under these conditions the vapour shield does not develop for investigated heat loads. The same is correct for the DEMO case. However, under reactor conditions erosion, splashing and stability of liquid flow remains an issue and requires further investigation.

In the case of DEMO1 envisaged unmitigated Type I ELMs heat loads that evaporation of Li reaches almost 0.14mm even in the case of capillary porous Li supplies. This depth of erosion could even exceed the molten layer thickness and results in intolerable erosion (see Fig 13 and 14).

In the case of DEMO1 mitigated ELMs (with 33 times reduced amplitude, like in ITER) impact the evaporation of Li per ELM is small $\leq 0.15\mu\text{m}$ and effect of molten layer deformation due to pressure gradient effect does not exceed $10\ \mu\text{m}$, e.g. after one ELM impact the crater depth is about $2\ \mu\text{m}$ and the hill height about $3.6\ \mu\text{m}$.

Up to now, the impact of a single ELM is considered. Modelling of the surface erosion under multiple ELM impact has been completed for the JET case (see Bazylev et al., paper submitted to PSI 2014 conference). Similar calculation can be done in future for DEMO conditions. We would like also to point out, that a further benchmarking of MEMOS code with experimental results (e.g. JET) will help to increase the confidence of numerical predictions.

8.5 References

- [1] B. Basylev and J.W. Coenen, Problems of Atom. Sci. and Techn. 1, Series: Plas. Phys.19 (2013) 3
- [2] N.I. Archipov, et al.// J. Nucl Mater. 1996, v. 233-237, p.686.
- [3] I. Garkusha, et al.,“The latest results from ELM-simulation experiments in plasma accelerators “, Physica Scripta, Volume 138, Issue , article id. 014054, 6 pp. (2009).
- [4] Yu. Igitkhanov and B. Bazylev “Modeling of DEMO PFC Erosion due to ELM Impact”, in the IEEE Transactions on Plasma Science, 10.1109/SOFE.2013.6635280 2013, Page(s): 1 – 6

Appendix I

Yu. Igitkhanov

DEMO conventional divertor operation; predictive studies of transition from attached to detached states.

EFDA Task WP13-PEX-01-T01

I.1 Introduction

A 2 point model of the boundary tokamak plasma is used below. A schematic of the SOL plasmas (between mid-plane to the X-point) and divertor plasma (between the X-point and the plate) is shown in Fig. 1

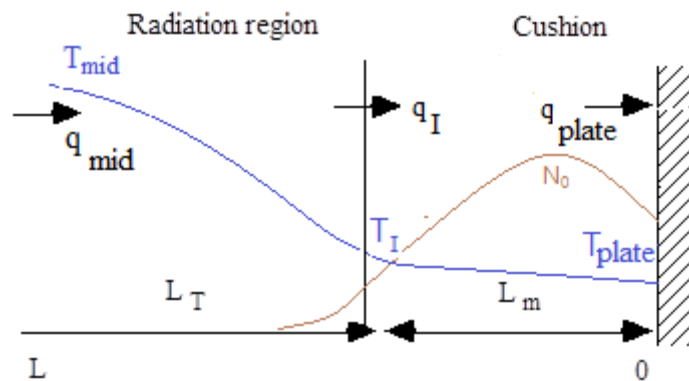


Fig. 1 Chart of the SOL and divertor plasma regions in detached state. The boundary between the radiation mantle and a cold divertor area is given provisionally

In the radiation region, energy losses occur due to the radiation of impurity ions and the power is transported by parallel heat conduction. In the right-hand part of the cushion, the plasma is cold and the remaining power is so small that ionisation is excluded and temperature is taken to be almost constant along the region ($T_i \sim T_w$). Convection dominates the heat flow in this region. In the vicinity of the interface between the two regions, ionisation takes place (ionization front).

In the model we are not specifying the position of the border between these two regions, because the cushion will be self-consistently developed according to the balance equations. In the cushion, neutrals provide momentum loss, reducing the pressure considerably below the pressure in mid-plane. This is the main difference with attached state, when the pressure drop between the mid-plane (upstream pressure) and the plate (downstream pressure) practically remains unchanged (if one neglects the contribution of kinetic pressure at the sheath, where a Mach number assumed to be equal to one).

I.2 Balance equations

The relation between upstream and downstream pressure can be found by integrating the momentum balance equation. It has been pointed out (*Lackner, 96*) that the near target-plate plasma pressure in the low divertor temperature region (see Fig. 1) is essentially determined by the heat flux to the target plate

$$P_p = q_{up} \cdot \frac{(1 + \gamma M^2)}{M} \cdot \frac{(1 - f_{rad})}{(1 - f_m)} \cdot \frac{1}{2\sqrt{\gamma_t \cdot \varepsilon}} \quad (1)$$

On the other hand, in the case of dominant heat conduction the capability to lose energy by impurity radiation from the scrape-off layer increases monotonically with pressure:

$$P_{mid} \approx q_{mid} \sqrt{\frac{f_{rad}(2 - f_{rad})}{f_z l_z}} \quad (2)$$

Strong radiation losses can be established at high upstream and low downstream pressure (see **Fig.2**). Therefore strong radiation losses (detachment) can be ensured only at high upstream and low downstream pressure (JET).

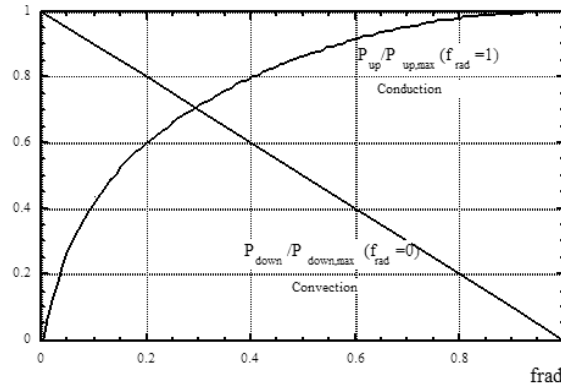


Fig. 2 Ratio of upstream, P_{up} to downstream pressure, P_{down} depending on the radiation fraction, $f_{rad} = q_{rad}/q_{mid}$.

A situation with large heat losses (needed to get the divertor heat flux down in order to achieve detachment) would thus not be consistent with the low plasma pressure where required to remain constant on flux surfaces (or even dropping twice due to the sheath effect at the plate).

Charge exchange (CX) friction implies, however, an increase of the mid-plane pressure over the near-target plate value, allowing one to make such a scenario self-consistent. In fact, as substantial CX losses require a lowering of the electron temperature to values in the regime $T_d < 10$ eV, the two effects—momentum losses and increased radiation losses—will develop in synergy, with radiation losses bringing

down T_d to allow momentum losses, and momentum losses allowing the mid-plane pressure to remain sufficiently high for substantial radiation losses.

Basically, calculation of this effect requires, in general, detailed 2D SOL modeling calculations, to include the geometrical effects onto the actual magnitude of the charge exchange momentum. For the understanding of the global trends it is, however, useful to describe its effect by a momentum loss fraction f_{mom} in the momentum balance between the flow stagnation point on the field line (usually taken in the outer mid-plane) and the near-target plate region as

$$P_{plate} \approx \frac{1 - f_{mom}}{1 + \gamma M_d^2} P_{mid} \quad (3)$$

Complemented by the solution of the heat conducting equation (T [keV]):

$$T_{mid}^{7/2} = T_{plate}^{7/2} + \frac{7}{2\chi_0} \overline{q_{||} L} \approx 5.7 \times 10^{-8} \overline{q_{||} [MW / m^2]} L [m] \quad (4)$$

and the relation between target plate particle and energy fluxes

$$q_{mid}(1 - f_{rad}) \approx \Gamma_{plate} (\delta_t T_{plate} + \varepsilon), \quad (5)$$

where

$$\Gamma_{plate} \approx M \frac{P_{plate}}{\sqrt{T_{plate}}} \cong \frac{M}{1 + \gamma M^2} \frac{1 - f_{mom}}{\sqrt{T_{plate}}} P_{mid} \quad (6)$$

is a particle flux to the plate. Expressions (5) and (6) included arbitrary Mach numbers at the target plates and to include a fractional radiation loss f_{rad} covering impurity radiation (hydrogen radiation losses are included in the definition of the effective ionization energy, ε). Equation (5) serves as a definition of radiation loss due to impurities, f_{rad} . Electron energy flow into the Langmuir sheath region is taken into account by the electron energy transfer coefficient δ_t . Equation (5-6) can be converted to the relation between the mid-plane pressure and the temperature in front of the target plates (T_{plate})

In the cold divertor regime of interest here,

$$T_{mid}^{7/2} \gg T_{plate}^{7/2}, \text{ so that}$$

will hold, so that

$$T_{mid}^{7/2} \cong \frac{1}{2\chi_0} \langle q_{up} L \rangle \approx 5.7 \cdot 10^{-8} q_{up} [MW / m^2] \cdot L [m] \quad (7)$$

and equation (7) gives the relationship between the mid-plane density and the temperature in front of the target plates:

$$n_{up} = n^* \frac{1 - f_{rad}}{1 - f_{mom}} \quad (8)$$

where

$$n^* \equiv \frac{q_{up}^{5/7}}{L^{3/7}} \frac{1 + M^2}{M} \left(\frac{2}{7} \chi_0 \right)^{2/7} \frac{\sqrt{T_d}}{(\varepsilon + \delta_i T_d)}$$

For upstream separatrix densities ($n \geq n^*$) the radiation losses required for detachment are consistent only in the case of considerable momentum losses.

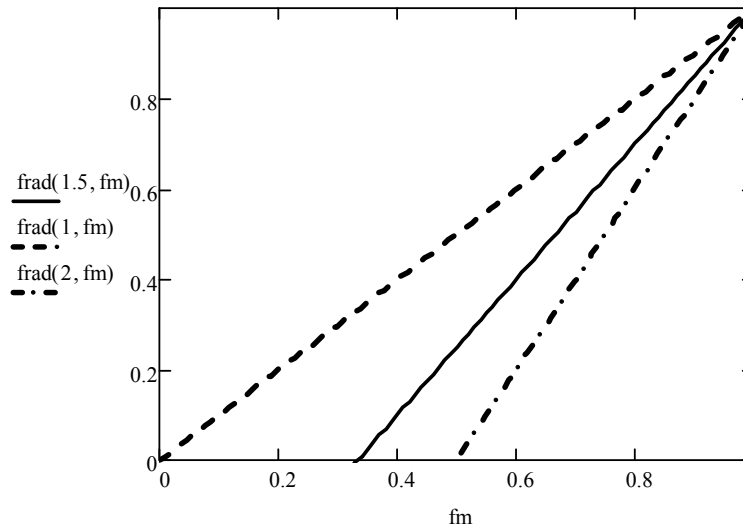


Fig. 3 It is how how fraction of radiation depends on momentum loss for $n^* = 1, 1.5$ and 2 . No radiation without momentum loss is allowed.

Detachment can be achieved when radiation is strong enough to exhaust the plasma ionization capability in the downstream region. High radiative losses are allowed at low upstream density when the convective losses to the target decrease with increase of the downstream pressure. The transition from the attached to the detached state can be performed gradually at the same upstream density value (without violating the density limit). Momentum removal from plasma is essential in order to sustain a pressure drop along B, required for substantial radiative losses in the detached regimes. Efficiency of momentum removal could have a strong impact on divertor performance, define the requirements for a wall or baffle location in divertor. Actual momentum and radiative losses can be determined by using 2 point model described below. Here we suggest a simple 2point model of A/D transition.

The relation between upstream and downstream pressure can be found by integrating the momentum balance equation (see e.g. Braginskii):

$$\nabla_{\parallel} (p + mnV_{\parallel}^2) = -\nabla_{\perp} (mV_{\parallel} D_{\perp} \nabla_{\perp} n) - \frac{mnV_{\parallel}}{\tau_{cx}} \quad (9)$$

The plasma pressure ($p = p_e + p_i$) drop along the magnetic field line is determined by momentum loss due to CX collisions with neutrals (the last term on the r.h.s., V_{\parallel} is the plasma velocity along B) and by radial spreading across B (the first term). Here $m = m_i$ and $n = n_e = n_i$. For simplicity one can neglect the radial transport. Then, taking into account that $V_{\parallel} = 0$ at the mid-plane (upstream) the integration along B (x axes) gives:

$$p_{up} - (p + mnV_{\parallel}^2)_d = -\int \frac{mnV_{\parallel}}{\tau_{cx}} dx \quad (10)$$

or

$$p_d \cong p_{up} \frac{(1 - f_m)}{1 + \gamma M^2} \quad (11)$$

Where we introduce the momentum loss fraction f_m due to charge exchange collisions with neutrals

$$f_m \equiv \frac{p_{up} - p_d}{p_{up}} \approx \frac{1}{p_{up}} \cdot \int \frac{mnV_{\parallel}}{\tau_{cx}} dx \quad (12)$$

and γ is the ratio of specific heats. When $f_m = 0$, there is almost no pressure drop and $p_{up} = (1 + \gamma M^2) p_d \sim 2 p_d$ because at the sheath entrance $M \sim 1/\gamma$ (not 1 because of a definition of $c_s = (\gamma T/m)^{1/2}$). Here M (or M_d) is the Mach number at the plate (indexes d or *down*, *plate* or w are identical as well as *upwards* and *mid-plane* terms). In general, the relation between upstream and downstream pressure reads as (see Eq. 3)

$$p_{up} \cong q_{up} \frac{(1 - f_{rad})}{(1 - f_{mom})} \frac{(1 + \gamma M^2)}{M} \frac{\sqrt{T_{plate}}}{(\varepsilon + \delta_t M^2)} \quad (13)$$

where $\gamma = c_p/c_v$. Then, using (3) the particle flux density at the plate can be expressed via the upstream pressure, p_{up} :

$$\begin{aligned} \Gamma_{plate} &= \frac{n_p}{4} \sqrt{\frac{8T_p}{\pi \cdot m}} \approx c_{s0} \cdot \frac{n_p}{4} \sqrt{T_p} \approx c_{s0} \cdot \frac{1}{4\sqrt{T_p}} \cdot p_p \approx \\ &\approx c_{s0} \cdot \frac{(1 - f_m)}{4\sqrt{T_p}} \cdot p_{up} \end{aligned} \quad (14)$$

Here c_{s0} is the ion sound speed at 1eV. In general, the particle flux density at the plate reads as (see Eq. 6)

$$\Gamma_{plate} \approx \frac{M}{1 + \gamma M^2} \cdot \frac{1 - f_m}{\sqrt{T_{plate}}} \cdot P_{up}$$

Integrating the energy balance equation

$$divq = -nn_z L(T)$$

along the magnetic field line and neglecting the radial losses, one has:

$$q_{up} = q_d + \int nn_z L(T) dV = q_{up} + q_{rad} \quad (15)$$

$$\text{where: } q_{rad} \equiv \int nn_z L(T) dV = q$$

The energy losses downstream (at the plate) q_p can be written as

$$q_p = \Gamma_{plate} \cdot (\gamma_t \cdot T_p + \varepsilon), \quad (16)$$

and, therefore

$$q_{up} \cdot (1 - f_{rad}) = \Gamma_{plate} \cdot (\gamma_t \cdot T_p + \varepsilon) \quad (\text{see Eq. 5})$$

where

$$f_{rad} \equiv q_{rad} / q_{up}. \quad (17)$$

Here $\varepsilon \approx 20\text{eV}$ is the average ionization losses per particle, $\gamma_t \sim 3.5$ accounts for the ion acceleration in the pre-sheath. Substituting particle flux from (A5), one can find the link between the upstream pressure and q_{up} , f_m and f_{rad} :

$$P_{up} = q_{up} \cdot \frac{(1 + \gamma M^2)}{M} \cdot \frac{(1 - f_{rad})}{(1 - f_m)} \cdot \frac{\sqrt{T_p}}{(\gamma_t \cdot T_p + \varepsilon)} \quad (18)$$

It can be shown that the last ratio in (A10) explicitly depending on temperature has a sharp maximum at low T_p

$$\max \frac{\sqrt{T_p}}{(\gamma_t \cdot T_p + \varepsilon)} \approx \frac{1}{2\sqrt{\varepsilon\gamma_t}}$$

Therefore (A10) can be written as:

$$p_{up} \leq q_{up} \cdot \frac{(1 + \gamma M^2)}{M} \cdot \frac{(1 - f_{rad})}{(1 - f_m)} \cdot \frac{1}{2\sqrt{\gamma_t \cdot \varepsilon}}$$

Now we prove that the capability to lose energy by impurity radiation from the SOL increases monotonically with upstream pressure. Multiply the energy balance equation by $q = -\chi dT/dx$ (x is the coordinate along B)

$$q dq = \chi n n_z L(T) \cdot dT$$

and replace the x -variable via temperature variable ($dx = (\chi/q)dT$) one can find:

$$q_{up}^2 - q_d^2 = p_{up}^2 f_z^{up} \cdot \langle l_z \rangle \quad (19)$$

where

$$\langle l_z \rangle \equiv 2 \chi_0 \int l_z(T) \sqrt{T} dT \quad (20)$$

$l_z(T)$ is the emissivity, f_z is the impurity concentration n_z/n and χ_0 is the electron thermal conductivity at 1eV. Equation (A11) can be rewritten as:

$$f_{rad} (2 - f_{rad}) = \left(\frac{p_s}{q_s} \right)^2 f_z^{up} \cdot \langle l_z \rangle \quad (21)$$

and (see Eq. 1)

$$\frac{p_s}{q_s} = \sqrt{\frac{f_{rad} (2 - f_{rad})}{f_z^s \cdot \langle l_z \rangle}}$$

The ratio p_s/q_s in (13) can be excluded using (10). Then the relation between the radiation fraction and the momentum loss fraction for given impurity concentration reads as:

$$f_{rad} \cong 1 - \left\{ 1 + \text{const} \frac{f_z \bar{l}_z}{(1 - f_{mom})^2} \right\}^{-1/2} \quad (22)$$

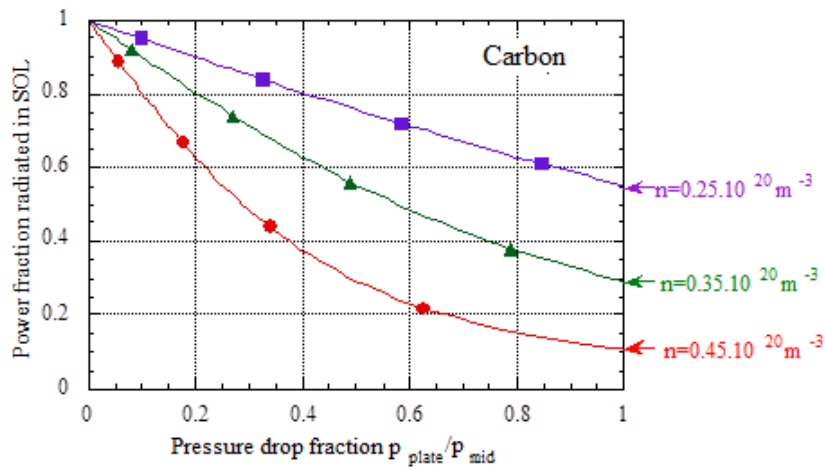


Fig. 4 Power fraction of impurity radiation vs pressure drop fraction plotted here for the different carbon concentrations.

I.3 A 2-Point Model for simulation of attach to detach (A/D) transition

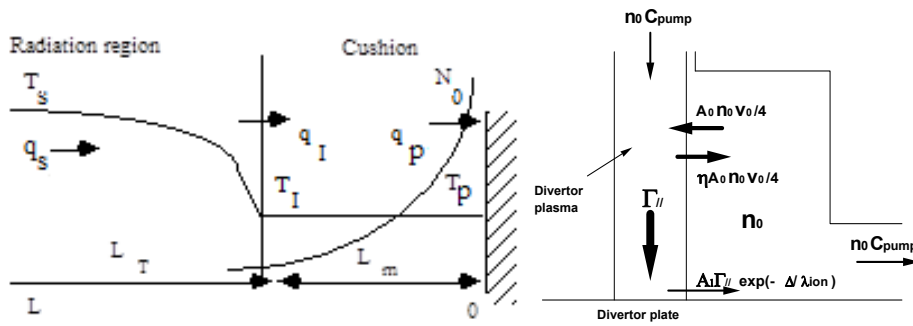


Fig. 5 Model of divertor plasma in detached state and neutral particle balance in the divertor region.

(1) The particle flux density along the field line at the plate

$$\Gamma_{plate} = c_{s0} \frac{M}{1 + \gamma \cdot M^2} \cdot \frac{1 - f_m}{\sqrt{T_p}} \cdot n_s T_s, \quad M \sim 1, \gamma = 5/2$$

(2) The remaining (after impurity radiation) power flow to the plate by convection

$$q_p = \Gamma_{plate} \cdot (\varepsilon + \gamma_t \cdot T_p), \quad \text{where} \quad \varepsilon \approx 20 \text{ eV}, \quad \gamma_t \approx 7,8$$

(3) The momentum loss fraction (d is the lateral gap between the plasma and the wall)

$$f_m = 1 - \exp(-L_m / \lambda^*);$$

$$\lambda^* = 2.398 \cdot d(m) (11.51 \cdot Kn + 1) \quad Kn = 2.5 \cdot 10^{19} / (d \cdot n_0),$$

(4) Equation for the neutral density n_0 in the divertor region:

$$\Gamma_p \exp(-\Delta / \lambda_{ion}) A_1 = \frac{B_{||}}{B_p} n_0 (C_{pump} + \frac{A_0}{4} v_0 (1 - \eta)), \quad A_1 = 2\pi R \Delta$$

(5) Heat flux in upstream of the cushion (L_T)

$$q^2(T) = q_p^2 + \frac{\chi_0 (2n_s T_s)^2 f_z}{2} \int_{T_w}^T \sqrt{T} l_z(T) dT; \quad l_z(T) \text{ e.g. } corona$$

(6) The length of the radiation zone, L_T

$$L_T = \chi_0 \int_{T_p}^{T_s} \frac{T^{5/2}}{q(T)} dT = L - L_m$$

(7) Neutrals undergo the CX within the SOL plasma fan

$$\lambda_{ion} = \Delta$$

We have 7 unknowns, $q_p, T_p, T_s, \Gamma_p, n_0, f_p, L_m$

and with given upstream parameters : n_s, q_s

Constants: $f_z, \varepsilon, \gamma_{\tau}, c_{s0}, M, d_m, \Delta, \chi_0$

Appendix II

A MARFE-type thermal instability on closed magnetic field lines

II.1 Introduction

The thermal-radiation instability develops when a local decrease of temperature re-enforces the impurity radiation, causing a further cooling of the plasma, and when thermal conduction enables the compensation of this energy loss. The experimental observations indicate that the MARFE tends to locate itself near to the x-point, where it can be almost in quasi-steady state condition [1,2]. The linear stability analyses of the plasma edge parameters which provides the onset of the x-point MARFE should be carried out in a 2-D toroidal magnetic geometry with an x-point. The main problem of solving such a problem in the toroidal geometry is that the variables (usually they are the flux co-ordinates) are not separable, thus one is unable to apply the usual representation involving the ordinary Fourier expansion without having a mixture of the eigenmodes. The problem arises due to the poloidal variation of the metric coefficients and the equilibrium quantities. A number of investigations have been performed in this direction, reducing the 2-D problem to a 1-D problem by simply excluding the radial or poloidal heat flux in the heat equation or by considering the cylindrical approximation, thus ignoring the toroidal and x-point effects [3]. In some consideration the perpendicular heat fluxes were excluded because of the high classical electron heat conduction along the field lines, enforcing nearly constant temperature on magnetic flux surfaces. However, because of the strong temperature dependence of the classical parallel conduction and the electron heat flux limit at low densities, noticeable gradients along field lines are to be expected at typical tokamak edge parameters if there are sufficiently strong, localized energy sinks. These can be caused by, for example, impurity radiation. It is obvious that this simplification does not work close to the x-point, where the radial fluxes are expected to be strong. For the same reason the toroidal effects must be fully employed in the stability analyses of the MARFE-type perturbation in a realistic tokamak configuration [4]. Here we consider a 2D linear stability analysis of the MARFE-type perturbation inside the last magnetic surface in a toroidal geometry with a separatrix. Based on the special type of perturbation which allows one to resolve the separability problem of the heat equation in toroidal geometry, we will prove that both the radial and parallel heat fluxes should be taken into account and cannot be omitted without change of the spectral properties of the anisotropic heat conduction equation. The separation of variables can be strictly performed in case of the 2D toroidal geometry including the x-point by employing a so-called "ballooning type" of perturbation. The ballooning representation has been first invented to overcome the same difficulty in the ballooning equation of the MHD perturbation in the toroidal geometry [5].

Below we will show that this type of perturbation, being applied to the heat equation can resolve the problem of the separability of the variables and to provide the analyses of the onset conditions without any "simplified" suggestions, corrupting the operator of the 2D differential equation.

II.2 Equations and topology for the standard divertor configuration

We begin the linear stability analyses by considering the heat equation in orthogonal flux co-ordinate system and assuming the constant pressure along the magnetic field lines:

$$\dot{\varepsilon} + \frac{1}{\sqrt{g}} \frac{\partial}{\partial x^i} (\sqrt{g} q^i) = S_\varepsilon, \quad \text{and} \quad (\vec{B} \nabla p) = 0, \quad (1)$$

where:

$$q^i \equiv -\chi_\perp g^{ik} \frac{\partial T}{\partial x^k} - (\chi_\parallel - \chi_\perp) b^i (b^k \frac{\partial T}{\partial x^k}), \quad |\vec{b}^2| = 1 \quad (2)$$

Here b^i and q^i are the covariant components of a unit vector in the direction of the magnetic field, $\vec{b} = \vec{B} / |\vec{B}|$, and the heat flux components, respectively. $\varepsilon = 3nT$. In (2A) we took into account the different heat conduction coefficients along B , χ_\parallel and across the magnetic surfaces, χ_\perp . The source term in (1A) arises from impurity radiation $S_\varepsilon = -n^2 c_z L(T)$, where n is a plasma density $L(T)$ is a cooling rate function and c_z is an impurity concentration. The rest of the definitions are obvious. We aim to consider the linear stability of the equations (1A) in toroidal geometry close to the separatrix area. For this purpose we choose the orthogonal flux co-ordinate system allowing for a plasma shape with x-point. For simplicity we choose the topology created by a pair of parallel wires carrying equal currents [6]. The model possesses a separatrix, with an x-point midway between the wires and allows one to investigate thermal stability at various distances from the separatrix and to examine the effect on marginal stability when changing the location (in poloidal angle) of the x-point. The metric coefficients can be expressed analytically. The line element in this case reads as: $ds^2 = h^2 (d\rho^2 + d\theta^2) + R^2 d\varphi^2$, where ρ is marking the magnetic surfaces, and θ and φ are the poloidal and toroidal angular variables. Here $g_{\psi\psi} = g_{\theta\theta} \equiv h^2$, $g_{\varphi\varphi} = R^2$, $\sqrt{g} = h^2 R(\theta, \varphi)$ and $h^2 = e^{2\rho} / 4y_0^2 b^2$. The major radius for the current point position at the surface is

$$R(\theta, \rho) = \frac{R_0}{y_0} \pm \sqrt{\frac{a+b}{2}}.$$

Here R_0 is the distance from the azimuthal axes to the current position at the mid-plane, y_0 is the distance of the current wire from the x-point position (see Fig.1). Here $a \equiv e^\rho \cos \theta - 1$ and $b^2 \equiv (1 - 2e^\rho \cos \theta + e^{2\rho})$. We shall consider the surfaces lying inside the separatrix and they are labeled by a parameter ρ , such that when $\rho \rightarrow -\infty$ the surfaces become circular. As $\rho \rightarrow 0$, the shape of the surfaces approaches that of a separatrix and $h \propto 1/\rho$. For numerical convenience we will use below another parameter for labeling the surfaces, ξ , which is linearly shifted relative to ρ , $\xi \equiv k\rho + \text{const}$. Here $k \approx 7.9$. ξ ranges from $-\infty$ at the core area to some positive value $\xi = \xi_{sep}$ ($\xi_{sep} \approx 0.58$) at the separatrix. The ψ_{95} distance corresponds to about $\xi_{95} \approx 0.6$. The poloidal magnetic field caused by straight currents and the toroidal magnetic field can be chosen as $b_\theta = \gamma / \sqrt{h^2 + \gamma^2}$, $b_\varphi = \sqrt{1 - b_\theta^2}$, $b_\rho = 0$, where $b_\theta \equiv B_\theta / B$, $b_\varphi \equiv B_\varphi / B$ are the physical components and $\gamma \approx \text{const}$. is taken to match the ITER magnetic field. The heat equation in the orthogonal co-ordinates reads:

$$\frac{\partial}{\partial \theta} \{h^2 R q^\theta\} + k \frac{\partial}{\partial \xi} \{h^2 R q^\xi\} + \frac{\partial}{\partial \varphi} \{h^2 R q^\varphi\} = -n^2 c_z L(T) h^2 R \quad (3)$$

where $p \approx \text{const}$. on the magnetic surfaces. Here

$$q^\theta \equiv -\frac{\chi_\theta}{h_\theta^2} \frac{\partial T}{\partial \theta} - (\chi_{||} - \chi_\perp) \frac{b_\theta b_\varphi}{h_\theta R} \frac{\partial T}{\partial \varphi}; \quad (4)$$

$$q^\xi \equiv -\frac{\chi_\perp}{h_\rho^2} \frac{\partial T}{\partial \xi}; \quad (5)$$

$$q^\varphi \equiv -\frac{\chi_\varphi}{R^2} \frac{\partial T}{\partial \varphi} - (\chi_{||} - \chi_\perp) \frac{b_\theta b_\varphi}{h_\theta R} \frac{\partial T}{\partial \theta}; \quad (6)$$

$$\text{and } \chi_\theta \equiv \chi_\perp + (\chi_{||} - \chi_\perp) b_\theta^2, \chi_\varphi \equiv \chi_\perp + (\chi_{||} - \chi_\perp) b_\varphi^2.$$

In equilibrium, due to the toroidal symmetry of the problem we can omit the third term in Eq.(4). The equation reveals several equilibrium solutions which may be classified as those which have a constant temperature along the field line (MARFE-free, radial equilibrium) and to a MARFE equilibrium when the temperature varies along the field line, i.e. exhibit a MARFE-like character. The first case can also be considered as a poloidally symmetric radiating region on closed flux surfaces (detached MARFE) and its linear stability against the most unstable poloidal mode has been treated in [3] as an eigenvalue problem, ignoring the dependence of the metric coefficients on θ . In the geometry adopted here a poloidally symmetric equilibrium reads as a balance of the radial heat fluxes incoming to and outgoing from the poloidal layer:

$$\left\{ Rq_\xi \frac{h}{k} \right\}_\xi^2 = \left\{ Rq_\xi \frac{h}{k} \right\}_\infty^2 - \int_\infty^T 2n^2 c_\perp L(T) \left(\frac{hR}{k} \right)^2 \chi_\perp dT, \text{ where } q_\xi \frac{h}{k} d\xi = -\chi_\perp dT \quad (7)$$

Since the coefficients in this equation are the functions of ρ and θ , the equilibrium differs from that in [3]. In equilibrium the temperature gradient along the magnetic field lines from the mid-plane to the x-point caused by a strong radiative cooling due to impurity accumulation in the vicinity of the x-point. The stability analyses of equation (1), with the periodic boundary conditions in poloidal direction on the closed magnetic field lines must be treated as an eigenvalue problem for the parabolic partial differential equation (3). In this equation the thermal coefficients are functions of temperature and density: $\chi_{||} = \chi_{||,0} T^{5/2}$, $\chi_\perp = \chi_{\perp,0} nT$. The eigenfunction must be periodic in θ, φ space and zero in infinity with respect to ξ . Obviously the operator in (3) is not separable as it stands. Following [5] we consider equation (3) in "ballooning space"- which is the extended infinite θ domain and try the temperature perturbation of the form

$$T(\theta, \xi, \varphi) = W(y) e^{im(\varphi - \int_0^y q(\xi, t) dt)} \quad (8)$$

where $y \equiv \theta - \theta_0$, m is a toroidal mode number and $q(\xi, y) \equiv \frac{h_\theta b_\theta}{R b_\theta}$. The trial function (8)

corresponds to a perturbation with a long parallel wavelength and short perpendicular wavelength with a large harmonic number $m q \gg 1$. θ_0 is a free parameter in the ballooning presentation. The perturbation (8) enables us to separate variables and brings us to the following 1D Schrodinger-type equation for $\Phi(y)$:

$$\Phi''_y = U(y, \xi, m, \gamma) \Phi, \quad (10)$$

$$\text{where } \Phi \equiv \frac{W}{b_\theta \sqrt{R}}$$

and for the potential well we have:

$$U(y, \xi, m, \gamma) \equiv U_m(y, \xi, m) + U_\chi(y, \xi, \gamma) + U_\theta(y, \xi, \nabla T_0) \quad (11)$$

$$U_m(y, \xi, m) \equiv m^2 \frac{\chi_\perp}{\chi_{||} b_\theta^2} \left(\frac{h_\theta^2}{R^2 b_\theta^2} + I_\xi^2 \right) \quad (12)$$

$$U_\chi(y, \xi, \gamma) = \gamma \frac{h^2}{\chi_{||} b_\theta^2} \frac{\partial}{\partial T} \left(\frac{L(T)}{T^2} \right) \quad (13)$$

$$U_\theta(y, \xi, \nabla T_0) = \frac{1}{4} \left[\left(\frac{\partial \ln(R\chi_\theta)}{\partial y} + \frac{\partial \ln \chi_\theta}{\partial T} \left(\frac{\partial T}{\partial y} \right)_0 \right) \right]^2 + \frac{1}{2} \frac{\partial}{\partial y} \left[\left(\frac{\partial \ln(R\chi_\theta)}{\partial y} + \frac{\partial \ln \chi_\theta}{\partial T} \left(\frac{\partial T}{\partial y} \right)_0 \right) \right] \quad (14)$$

$$- \frac{1}{R\chi_\theta} \left[\frac{\partial}{\partial y} \left(R \left(\frac{\partial \chi_\theta}{\partial T} \right) \frac{\partial T}{\partial y} \right) \right]_0$$

Here $\gamma \equiv p^2 c_z$ is the eigenvalue and we denote the equilibrium terms in (11) by prescribing index 0. Equation (10) is an ordinary 1D differential equation, which can be easily analyzed and solved numerically, assuming that a new independent variable y varies in the infinite domain. The boundary conditions are now: $\Phi(\pm\infty) = 0, y \in (-\infty, \infty)$. The basic idea of the chosen transformation is that the spectrum of this eigenvalue problem in the infinite y -range is the same as in the original equation (3) in the periodic poloidal domain [5]. Following the property of the ballooning modes only terms of the order of m^2 remained in equation (10). Further we are solving the eigenvalue problem (10-14) numerically. The domain of integration of y in poloidal angle was found to be adequate. As a reference we took the DEMO - parameters ($R=7.5$ m, $B=6$ T etc.). Argon has been taken as an impurity sample and the cooling rate $L(T)$ was employed from [7], assuming a non-coronal radiative equilibrium. The second equation in (1) for pressure balance along the magnetic field suggests that the pressure perturbation equals to zero and that impurity density variation follows the perturbation of the plasma ions. The first term U_m in the expression for the potential well (11) is always positive. It represents the toroidal part of the perturbation and is attributed to a stabilizing role of the perpendicular (to the magnetic field lines) heat fluxes both along the magnetic surfaces $\sim (h_\theta/R_{b\theta})^2$ and across the surfaces

$$I_\xi \equiv k \int_0^y \frac{\partial q}{\partial \xi} dy'$$

The second term U_z is a destabilizing term and is attributed to the thermal instability. This term creates a negative potential due to a negative slope of the cooling rate function in the corresponding temperature domain. The rest of the terms in U_θ are associated both with the poloidal variation of the magnetic topology (volume element and the parallel heat flux) and with the equilibrium temperature gradient along the field lines. The stabilizing effect of the parallel heat flow reveals itself in denominators of all terms, which contain the value $\chi_\theta \approx \chi_{||} b_\theta^2$, so that the contribution of all terms (stabilizing or destabilizing) in the potential well is normalized to that of the parallel heat conductivity. In the vicinity of the x-point the flux expansion and the vanishing of the poloidal projection of the parallel heat flux should diminish the stabilising effect as $\sim (b_\theta/h)^2 \rightarrow \rho^{-4}$ ($\rho \rightarrow 0$) and $U_m \rightarrow 0$ at the separatrix. First we consider the toroidally symmetric temperature perturbations ($m=0$). Fig. 2 shows the stability diagram for such perturbations at the magnetic surface position $\xi=0.6$, which corresponds roughly to ψ_{95} . The stability diagram has two regions, the region above the marginal value of $\gamma=p^2 f_z$ which is unstable to MARFE and the region below this value where the temperature perturbations become stable. The marginal γ increases as expected for higher temperatures. Fig. 3 and 4 show the corresponding eigenfunction and potential behaviour vs. poloidal angle for $T=100$ eV. Numbers on figures indicate: 1 for U_m terms, 2 for U_z , 3 for the terms in U_θ proportional to the equilibrium temperature gradient, 4 and 5 represent the first terms in U_θ . The dashed line shows the resulting potential. It is interesting to note, that at $\theta=0$ the potential has a maximum (the eigenfunction passes

through the minimum (see Fig. 3)) and the negative part of the well is shifted symmetrically away from the x-point. This indicates that the perturbations are more stable at the x-point, than expected. This result is attributed to the poloidal variation of the coefficient in U_θ , namely:

$$\frac{1}{2} \frac{\partial}{\partial \theta} \left(\frac{\partial \ln(Rb_\theta^2)}{\partial \theta} \right)$$

which overcomes the negative contribution from U_z at the x-point and creates two negative wells in neighbouring positions to the x-point. The closer to the separatrix the well is located the deeper it becomes, however, in reality its shape and deepness do not change much, because they are limited by a similar term as the one in U_θ :

$$\frac{1}{4} \left(\frac{\partial \ln(Rb_\theta^2)}{\partial \theta} \right)^2$$

which gives a positive contribution. This is the reason, why the perturbations become almost insensible to the radial position from the separatrix (see Fig.5), except in the very vicinity to x-point.

The stability of the toroidal perturbations ($m \neq 0$) is shown in the Fig. 6,7. The critical impurity concentration f_z triggering a MARFE onset can be estimated for each toroidal mode number m (for given plasma density or pressure). The perturbations of this type become more stable due to the stabilizing role of the perpendicular heat fluxes. They are strongly stabilized especially near the x-point, where the perturbations on each magnetic field line approach each other, resulting in strong gradients both across and along the surfaces. This increases the fluxes and brings about the stabilization. Far from the x-point position, the shape of the potential well becomes more shallow (see Fig. 8) due to the positive contribution of U_m . We also investigated how sensitive is stability against the poloidal variation of the temperature. We chose the equilibrium temperature profile along the field line as $T(\theta) = T_1 - T_2 \cos \theta$, where T_1 is some average temperature. By varying T_2 we find that the potential well (being mostly affected by U_z) becomes negative and centered at the x-point, whereas the contribution of the rest terms in U_θ is negligible. This effect of destabilization (the increasing of U_z) is mainly due to the lowering of $\chi_\theta(T, \theta)$ at low temperatures.

II.3 Topology of the 2nd order null point configuration in the SF divertor

The snowflake divertor (Ryutov 2007, Phys. Plasmas 14, 064502) uses a 2nd order null of the poloidal magnetic field instead of the 1st order null used in the standard divertor. This leads to a number of interesting geometric properties such as stronger fanning of the poloidal flux, stronger magnetic shear in the edge region, larger radiating volume, and larger connection length in the scrape-off layer. These can potentially lead to new ways for alleviating heat loads on the divertor target plates. For our purpose

important is that a strong flaring of the scrape-off layer near the null-point compare with the x-point configuration. The model the SF configuration employed here is created by three straight wires as it shown in the Fig.11. Although this configuration is unstable, we use it just for illustrative purposes. Because of a larger poloidal flux expansion the connection length between the equatorial plane and the vicinity of the null is higher for the SF configuration. The connection length between the equatorial plane and the vicinity of the null point for the standard divertor is $L = (qR)\ln(b/\Delta_0)$, where q , R and Δ_0 (the SOL thickness) are taken at the equatorial plane (see Fig.1and Fig.10).

For the SF case the SOL connection length, $L_{sf} = (qR) (a^2/b\Delta_0)^{1/3} = L \cdot (a/b)^{1/3} (a/\Delta_0)^{1/3} / \ln(b/\Delta_0)$ (see Fig.11). In this configuration the magnetic flux becomes strongly broadened well above the second-order null point, making the geometrical connectivity of the snowflake divertor with the main SOL easier than in the standard divertor (see Fig.12). This may lead to the increased impurities flow to the vicinity of the null point and increase the plasma radiation. The plasma radiation from the null point region could locally decrease the temperature in circumstances where the cooling itself leads to increase radiation and hence the further cooling. It was shown that the broadening of the null-point region facilitates the onset of thermal instability. The longer connection length the stronger plasma cooling by radiative losses is expected. We skip here all numerical details of stability analysis (which is similar to the previous consideration apart from the metric coefficients, which are different). In Fig. 2 in the main text the critical impurity concentration (Ar) required for MARFE onset is shown as a function of the plasma density for the cases of SF and normal x-point configurations.

II.4 Conclusions

The main results are the following. The 2D linear stability problem of a MARFE-like temperature perturbation on closed magnetic surfaces has been reduced to a 1D eigenvalue problem using the ballooning representation for the perturbation. This type of a perturbation has a long parallel wavelength and short perpendicular wavelength typical for ballooning modes. The toroidally inhomogeneous temperature perturbations with non-zero mode toroidal numbers, m , having a weak variation along the magnetic field lines have been analysed and compared with toroidally symmetric temperature perturbations ($m=0$). The trial functions for the temperature perturbations for both ($m=0$) and ($m >1$) cases are localized on the closed magnetic surfaces near the x-point. The toroidal mode numbers m of marginally stable perturbations were found as a function of impurity concentration (at given plasma density or pressure). The geometry effects (variation of the metric coefficients with poloidal angle) have a strong influence on stability, ensuring localization of the MARFE-type perturbation slightly above the x-point.

II.5 References

- [1] B. Kadomtzev " Tokamak plasma: A Complex Physical System", plasma physics series, Editor: Prof. E. Laing, Institute of Physics Publishing, Bristol & Philadelphia, 1992
- [2] V. Mertens et al.16th IAEA Fusion Energy Conference, IAEA-CN-64/A, Montreal, 1995.
- [3] J. Wesson, T. Hender, Nuclear Fusion 33, 1019 (1993)
- [4] A. De Ploey et al, MARFEs: A magnetohydrodynamic Stability Study of Two-dimensional Tokamak Equilibria, JET-P(96)49
- [5] J. Connor, R. Hastie and J. Taylor, Phys. Rev. Letts. 40, p.396, (1978)
- [6] G. Hobbs, J. Taylor, The properties of Linear Filamentary Multipole Magnetic Fields, UKAEA, CulhamLab., Rep. CLM-R-95 (1968);
- [7] D. Post et. al. Atomic Data and Nuclear Data Tables 20,397, (1977)

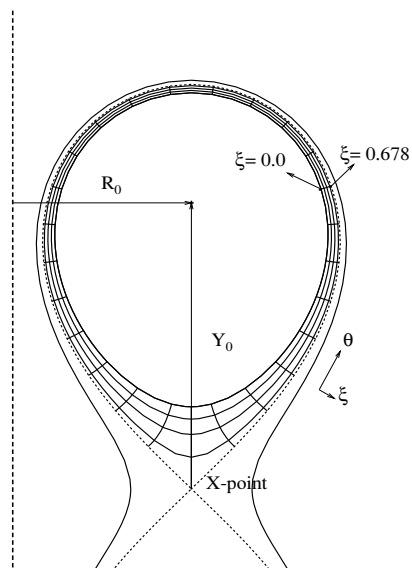


Fig. 1 Co-ordinate system allowing for the x-point.

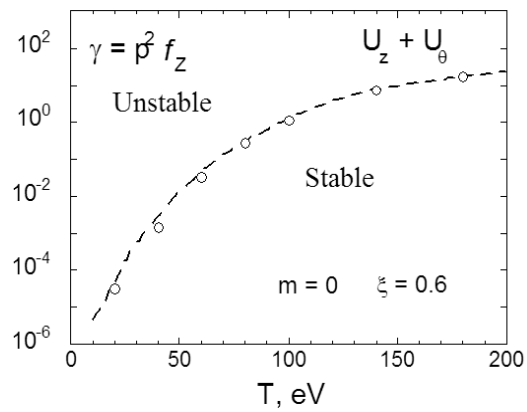


Fig. 2 Stability diagram for toroidally symmetric temperature perturbation on the magnetic surface at $\xi = 0.6$ (95%); toroidally mode number $m=0$; At high temperatures modes become more stable

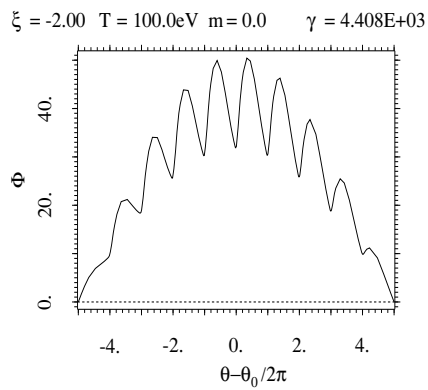


Fig. 3 The eigenfunction for $m=0$; $T=100\text{eV}$. It passes through the minimum at the x-point position.

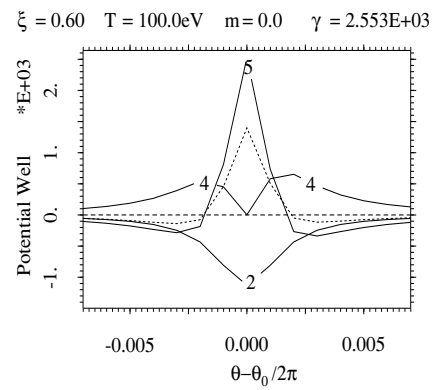


Fig.4 Potential U vs. poloidal angle; toroidally symmetric perturbation, $m=0$; $T=100\text{eV}$. Dashed line is a sum of all terms; $U_m = 0$. Potential has a maximum at the x-point.

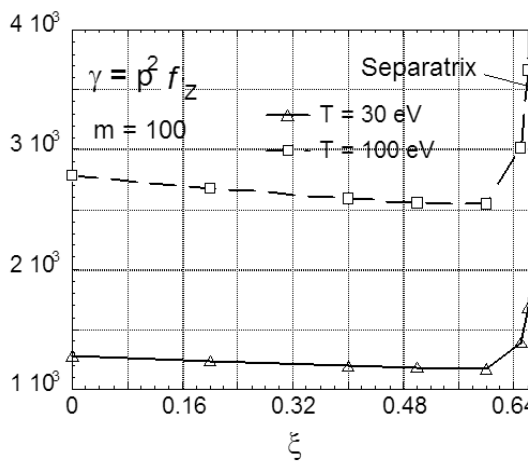


Fig. 5 Marginal value $p^2 f_z$ on the different magnetic surfaces, $m=100$; for $T=30\text{eV}$ and $T=100\text{eV}$. The perturbations are almost insensible to the radial position except to the very vicinity to the x-point.

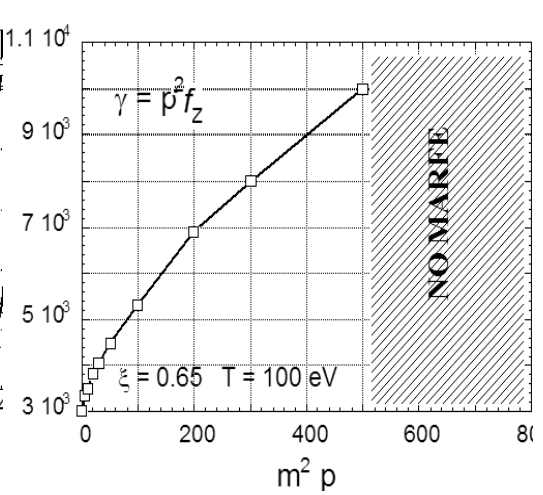


Fig. 6 Stability diagram for toroidal temperature perturbation on the magnetic surface, $m>1$; $\xi = 0.65$. Above some critical $m^2 p$ the perturbation does not exist anymore.

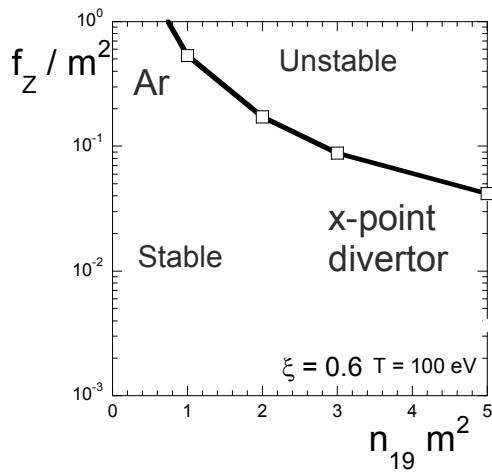


Fig. 7 Ar concentration f_z vs. plasma density for arbitrary toroidal mode number m and at the radial position $\xi=0.6$. The boundary temperature $T=100\text{eV}$.

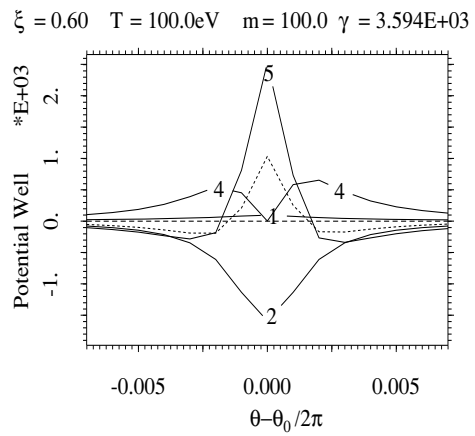


Fig. 8 Potential U vs. poloidal angle; toroidally non-symmetric perturbation, $m=100$; $T=100\text{eV}$

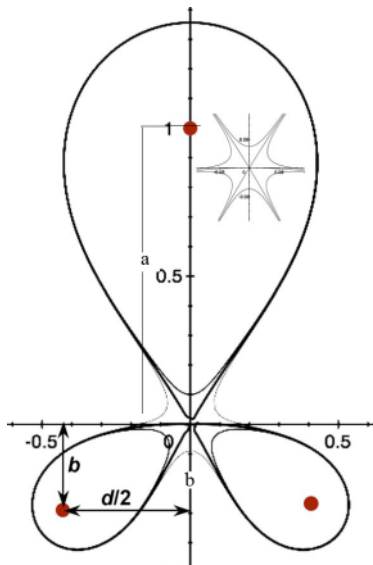


Fig. 9 The SF configuration created by three straight wires (D.Ryutov 2007, Phys. Plasmas 14, 064502).

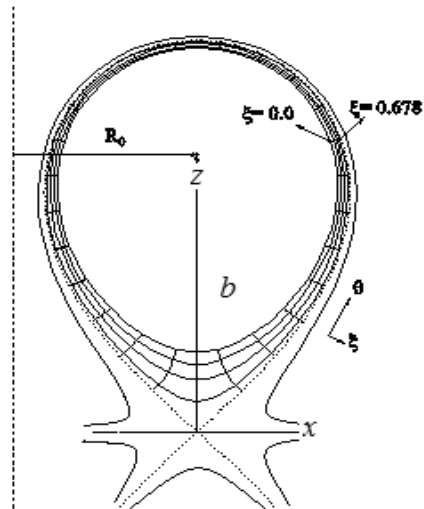


Fig. 10 The SF configuration in poloidal cross section. The region above the null-point is expanded.

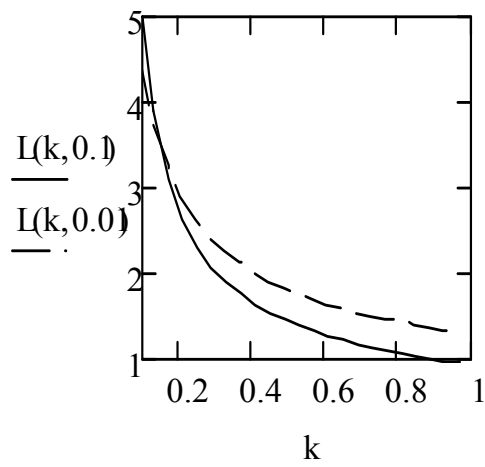


Fig. 11 The connection length in the SOL for the SF LSF (dashed line) and for the normal x-point configuration. $a=5\text{m}$, $k=b/a$, $\Delta_0 = 0.1\text{m}$ is the SOL width at the mid-plane. $LSF = (\frac{qR}{a}) \frac{(a^2/b\Delta_0)^{1/3}}{\ln(b/\Delta_0)} = L \cdot \frac{(a/b)^{1/3}}{\ln(b/\Delta_0)}$

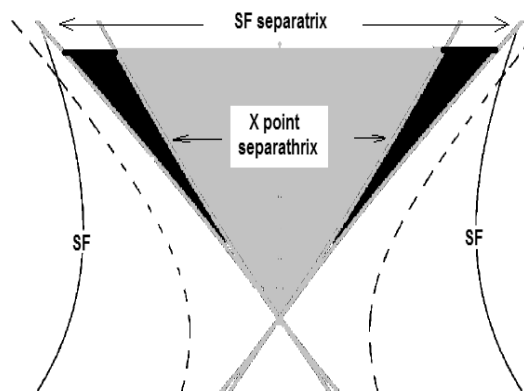


Fig. 12 The expansion of the region above the null-point in the case of the SF configuration. Because the null of the poloidal field is now of a higher order than in a standard X-point configuration, the magnetic flux threading the scrape-off layer SOL expands near the null point stronger than in a standard situation.

Appendix III

Sputtering erosion of PFC in a long pulse DEMO operation

III.1 Introduction

The important erosion process for the FW and baffles under steady-state DEMO operation is expected to be physical sputtering, since the W surface temperature remains below the melting point and ignition of arcing is insufficient for life-time limitation under normal operation^{5,6}. In our calculation we have emphasised two new important effects, which previously were ignored or approximately accounted for⁷. This is the dependence of sputtering yield on the angle of incidence and, particularly, the sheath potential effect on deviation of the distribution function of incident ions from Maxwellian one. The thickness, d of plasma facing elements (e.g. the FW blanket armour, limiter, etc.) sputtered away during Δt operation time by incident particle fluxes Γ_j of different species j , can be expressed as⁸

$$d(t) = \Delta t \cdot \frac{A_t \cdot m_p}{\rho_t} \cdot \sum_j \langle Y_j \Gamma_j \rangle \quad (1)$$

where A_t is the target atomic mass (in amu), ρ_t is the target material density, $Y_j(E, \theta)$ is the sputtering yield of particle j with energy E and angle of incidence θ and Γ_j is the flux of particles j . The brackets in (1) represent an average over the angular and energy distribution of incident particles. Thus, the precise determination of the erosion rate needs the correct form of the energy distribution function of the incident particles and the sputtering yield $Y_j(E, \theta)$.

III.2 Non-Maxwellian distribution function of incident ions

Here we present the results of erosion rate calculations taking into account deviation from Maxwellian the distribution function at the divertor plates due to the sheath acceleration and the angular dependence of the sputtering yield. Following ref. 8 the twice averaged sputtering yield, defined as the yield averaged over the distribution of energy and angle of incidence of the projectiles, is given by

$$\begin{aligned} \overline{Y_j} \left(\frac{atom}{ion} \right) = S_0 \int_0^1 \int_{\varepsilon^*}^{\infty} \exp \left(- \frac{\varepsilon}{\beta} (1 - t^2) \right) \times \\ \times \exp \left[- \left(\sqrt{\frac{\varepsilon}{\beta}} t^2 - \delta - M_0 \right)^2 \right] \cdot t S(\varepsilon, t) \cdot \varepsilon d\varepsilon \end{aligned} \quad (2)$$

where

$$S_0 = \frac{2E_{Th}^2}{T_i^2 F(M_0)}, \quad t \equiv \cos\theta, \quad \varepsilon = E/E_{Th}, \quad \varepsilon^* = \max(1, \delta); \quad \beta = T_i/E_{Th}, \quad \delta = Z_j e \varphi_0 / T_i$$

Here M_0 is a Mach number of incoming particle flux (which must be taken to one at the divertor plate according to Bohm condition and to zero at the FW), $S(\varepsilon, t)$ represents, the sputtering yield for a certain energy ε and angle of incidence of the particles, θ . This dependence can be described by the revised Bohdansky formula⁹ for the energy dependence and the Yamamura formula¹⁰ for the angular dependence. Figure 4 shows that the sputtering yield of tungsten for normal and shallow (70°) angles of Ar and Ne incidence varies in order of magnitude for high energies (≥ 1 keV).

The angular dependence becomes less pronounced after averaging over incident energy and in the case of cos-like of the angular distribution (see Fig. 1).

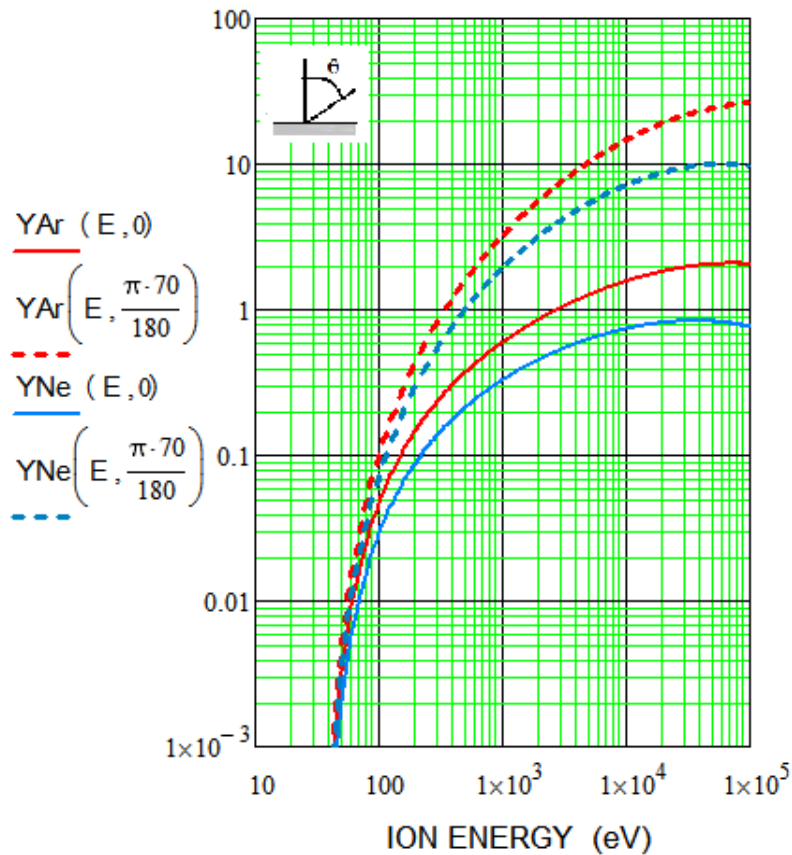


Fig. 1. $Y(E, \theta)$ for two angles $\theta = 0^\circ$ and 70° of incidence of Ar ($Z=18$) and Ne ($Z=10$) ions over tungsten surface vs. their energy; $Y(E, \theta)$ expression is used from.

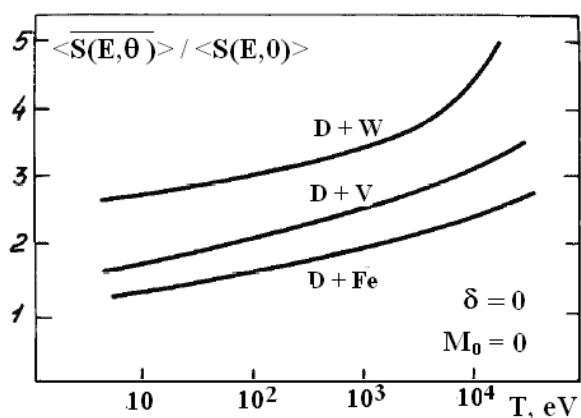


Fig. 2. Ratio of the sputtering yield of D ions over W, V and Fe, averaged over energy and angle of incidence to the yield averaged over energy only (i.e. for $\theta = 0$).

The importance of the incident particles acceleration in the sheath region is demonstrated in Fig. 2, where the twice averaged sputtering yields for Ar ions(in different charge states Z) on W for Mach numbers $M=0$ (without acceleration).

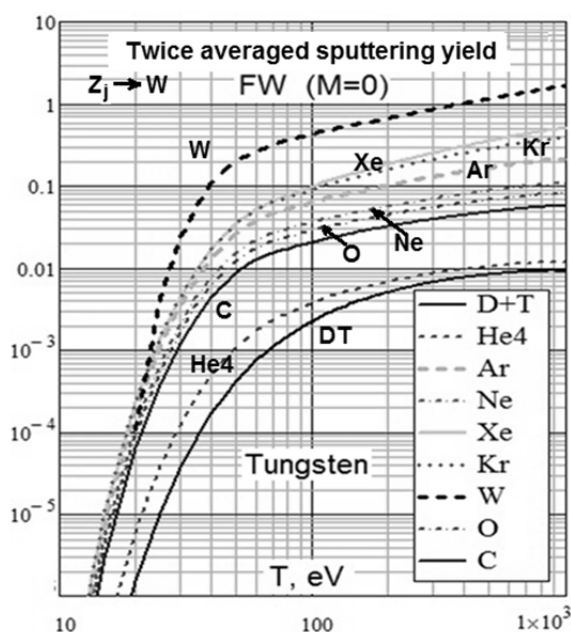


Fig. 3 W sputtering yield (twice averaged) vs. the ion temperature for various incident impurity ions in the most representative ionization charge states for corresponding temperatures.

The twice averaged values of W sputtering yields for various incident impurity ions taken at the most representative charge states at given temperature are evaluated based on Eq. (2) and data from ^{9,10,11}

(see Fig. 3). In these calculations the case of Maxwellian distribution of incident impurity ions on the FW is assumed ($M=0$).

Using formula (1) the erosion rate of W armour sputtered during one year of continues operation by various particle fluxes of $D+T+5\%He^{+2}$ incident ions is calculated (see Fig. 8a for the FW and in Fig. 8b for the divertor plates). Here we are taking into account that the 'fatal' concentration of He is about 5% from the average DT plasma density. For estimates of erosion rates a total wall ion flux of 10^{24} D+T at/s is taken, which corresponds to an average flux density of 10^{17} at/cm²s. Since this value remains uncertain for DEMO, we vary flux in the range of 10^{16} - 10^{18} 1/cm²/s. A seed impurity concentration of a few per cent, e.g. 2% N^{3+} (divertor seeded species) must be taken into account for the calculation of erosion rates, a spatial peaking factor (inhomogeneity of fluxes) of ~ 2 -3 has to be assumed as well (similar to ITER).

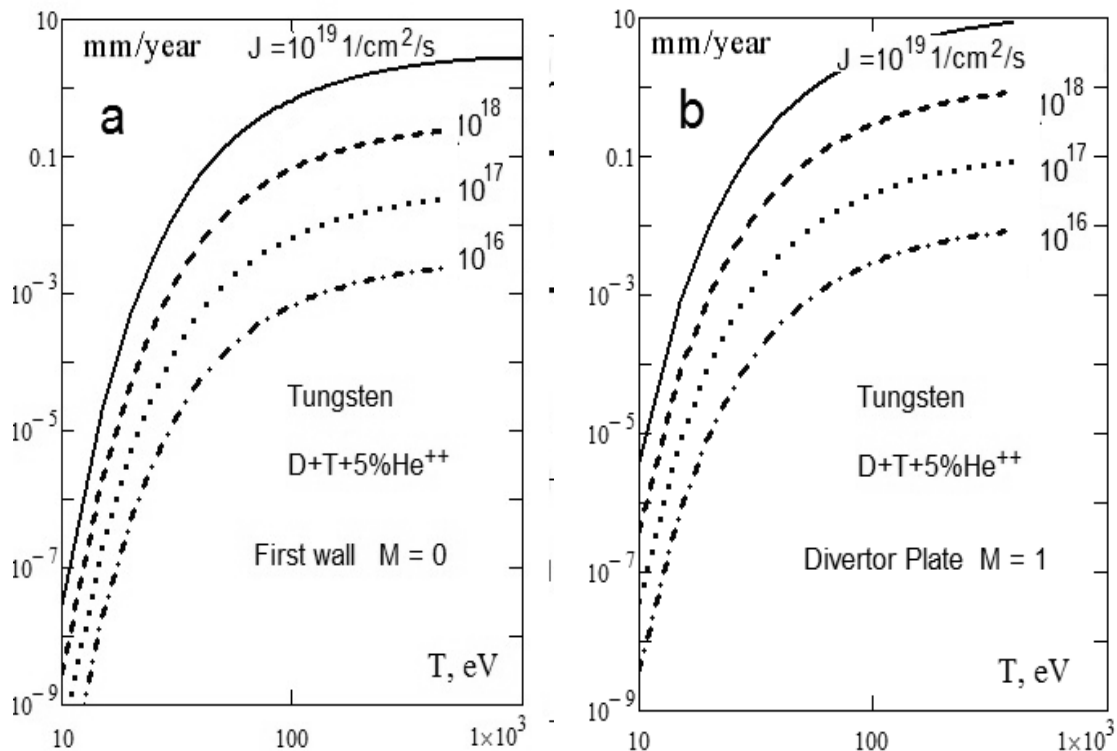


Fig.4 The thickness of the FW W armour (a) and divertor W plate (b) sputtered during one year of continues operation by various particle fluxes of D/T/5% He of incident ions $J(\text{cm}^{-1}\text{sec}^{-1})$

Calculations show that for envisaged in DEMO conditions the total sputtering erosion of the FW W armor by the charge-exchange DT neutrals and 5% Helium could reach $\sim 1\text{mm}$ during one year of steady-state operation (for particle flux of 10^{19} cm²/s and $T > 100\text{eV}$). Sputtering erosion from the

divertor plates is about 10 times high. Note that, this result was obtained without taken into account the re-deposition of sputtered ions.

III.3 Conclusion

Under steady-state operation condition the FW W/ EUROFER blanket module with helium coolant can tolerate the thermal loads expected in DEMO. The minimum W armor thickness is limited by the maximum allowable temperature of EUROFER (~ 550 °C). The W armor thickness $\Delta_w \sim 3$ mm and the EUROFER width $\Delta_{\text{EUROFER}} \sim 4$ mm are found optimal. The W surface temperature for $\Delta_w \sim 3$ mm remains below the melting point and the EUROFER temperature ≤ 550 °C. For the reference case ($\Delta_w \sim 3$ mm, $\Delta_{\text{EUROFER}} \sim 4$ mm) the maximum tolerable heat flux (which does not cause thermal destructions in structural material) is about ~ 13.5 MW/m².

Estimation of erosion of the FW by charge-exchange neutrals and the divertor plates by incoming ions shows the importance of angular dependence of sputtering yield and, particularly, the sheath potential effect. We have shown that the sputtering yield increases if the sheath potential is taken into account and that the usual estimation of the sputtering yields at energy $E=3.5ZT_e$ (to account for the sheath effect) underestimates the result. It is found important to account for the angular distribution of incident light ions at low and high temperatures in order to calculate correctly the sputtering yield averaged over the distribution function of the incident particles. Calculations show that under envisaged in DEMO conditions the total sputtering erosion of the FW W armor by the charge-exchange DT neutrals and 5% Helium could reach ~ 1 mm during one year of steady-state operation (for particle flux of 10^{19} cm²/s and $T > 100$ eV). Sputtering erosion from the divertor plates is about 10 times high (without redistribution effect).

Our results indicate that high pressure for Helium coolant in inlet is needed to achieve the required heat transfer to the coolant. This requires a big pumping power which could reduce the efficiency of the power conversions. In spite of this deficiency, helium adaptability to any operational temperature makes it very suitable for application in DEMO.

III.4 References

1. YU. IGITKHANOV , B. BAZULEV, I. LANDMAN and L. BOCCACCINI, paper P1-39 in conference of PSI, Aachen, 2012 (accepted for publication in Nuclear Materials).
2. D. WARD, Provisional Parameters for a Steady-State DEMO Device, TW6-TRP-002, Culham Science Centre, UK (2006); ITER Physics Basis, Chapter 9: ITER contributions for Demo plasma development, Nucl. Fusion 47, (2007) S404; ITER DDD, WBS1.9, Physics Section 6.3, 1983;
3. B. BAZYLEV et.al, J. Nucl. Mater. 307-311 (2002) 69
4. S.PESCHANYI et al., Fusion Engineering and Design 86 (2011) 1681–1684
5. YU. IGITKHANOV, B. BAZYLEV, Journal of Modern Physics, 2011, 2, 131-135; R. RAFFRAY, G. FEDERICI, Journal of Nuclear Materials 244 (1997) 85-100; G. FEDERICI et al., Journal of Nuclear Materials, 290-293 (2001) 260-265;
6. S. R. BERICH, G. FEDERICI, A. KUKUSHKIN et al., Journal of Nuclear Materials, 313–316 (2003) 388–392
7. G.F. MATTHEWS, Journal of Nuclear Materials, 337–339 (2005) 1–9
8. V.ABRAMOV, YU.IGITKHANOV et al., J. Nucl. Mater. 162-164 (1989) 462.
9. W. ECKSTEIN, C. GARCIA-ROSALES, J. ROTH et al; Max-Planck-Institut für Plasmaphysik Report, IPP 9/82 (1993).
10. Y. YAMAMURA, Y. ITIKAWA and N. ITOH, Nagoya University Report, 1PPJ-AM-26 (1983)
11. D. E. POST, R. V. JENSEN, C. B. TARTER, W. H. GRASBERGER, W. A. LOKKE, Atomic Data and Nuclear Data Tables 20, 397-439 (1977).

Appendix IV

Damage factor and characteristics of reactor materials

IV.1 Damage factor

To evaluate possible wall damage it is more convenient to characterize transitive heat loads in terms of the so called *damage parameter* $\phi_d = Q(J/m^2)/\sqrt{\tau}(\text{sec})$ representing in fact the surface temperature after heat pulse of duration τ . Indeed, consider the heat conduction problem for semi-infinite line with the heat influx $q(W/m^2)$ at $x = 0$ different from zero in the time interval $0 \leq t \leq \tau$:

$$\frac{\partial T}{\partial t} = \left(\frac{\chi_{\perp}}{\rho c_p} \right) \frac{\partial^2 T}{\partial x^2} + Q \quad x \geq 0, \quad 0 \leq t \leq \tau$$

$$T(0, t) = 0, \quad -\chi_{\perp} \left. \frac{\partial T}{\partial x} \right|_{x=0} = q_0$$

The analytical solution of the problem is easily found to give the surface temperature at the end of the square pulse [Landau L. D., Lifshitz E. M., Course of Theoretical Physics, Volume 6: Hydrodynamics, Moscow "Nauka" 1986, 289 pages (in Russian)]:

$$T(0, \tau) = 2 \sqrt{\frac{\chi_{\perp} \tau}{\pi \rho c_p}} \frac{q_0 (W/m^2)}{\chi_{\perp}} \approx 2 \sqrt{\frac{\chi_{\perp}}{\pi \rho c_p}} \frac{Q (J/m^2)}{\sqrt{\tau}},$$

In the case of finite thickness, ξ :

$$T(x, \tau) = \frac{2q_0 \sqrt{\tau}}{\sqrt{\pi \rho c_p \chi}} \cdot \left\{ e^{-(\xi/2)^2} - \frac{\xi}{2} \sqrt{\pi} \cdot \text{Erf}\left(\frac{\xi}{2}\right) \right\}$$

Extrapolation to ITER on basis of JET measurements gives $\phi_d = 24 \div 953$ with average $\sim 10^6 \text{ MJ}\cdot\text{m}^{-2}\cdot\text{s}^{-1/2}$ [Riccardo V., Loarte A. and the JET EFDA Contributors, Timescale and Magnitude of Plasma Thermal Energy Loss before and during Disruptions in JET, Nuclear Fusion, vol. 45 (2005), pp. 1427 - 1438]. Simple modeling considerations for hot VDE result in $\phi_d = 10 - 250 \text{ MJ}\cdot\text{m}^{-2}\cdot\text{s}^{-1/2}$ [Rosenbluth M. N., Putvinski S. V., Theory for Avalanche of Runaway Electrons in Tokamaks, Nuclear Fusion, vol. 37 (1997) pp. 1355 - 1362]. The given parameters are seen to exceed the critical erosion parameter $\phi_{cr} \sim 15 \div 60 \text{ MJ}\cdot\text{m}^{-2}\cdot\text{s}^{-1/2}$ for evaporation/melting for carbon, beryllium and tungsten to be used as wall materials. Solution of the two-dimensional heat conduction problem confirms that about 100 μm of the wall can be

eroded in one major disruption or hot VDE [Sugihara M., Shimada M., Disruption Scenarios, their Mitigation and Operation Window in ITER, Nuclear Fusion, vol. 47 (2007), pp. 337 - 352]. It is to be mentioned that the physics of ablation process is much more complex due to the formation of self shielding cloud of evaporated material, such calculations still indicate that layers about 30 – 70 μm can be lost in one event [ITER Physics Expert Groups on Divertor, Divertor Modeling and Database and ITER Physics Basis Editors, Chapter 4: Power and Particle Control, Nuclear Fusion, vol. 39 (1999), pp. 2391-2469].

To sum up, the uncertainties in scaling toward ITER are high. It is nevertheless clear that the heat loads are marginally at or above the critical level and will determine the lifetime of plasma facing components. For this reason softening of heat loads is required.

Edge-Localized-Modes (ELMs) have the potential to produce unacceptable levels of erosion of the DEMO divertor. Melting of the tungsten divertor target will occur if the surface temperature rises above about 3380.0 °C (3653K). Because a large number of ELMs, ≥ 10000 , are expected in each steady-state discharge (with 4-6h of operation) it is important that the surface temperature rise due to an individual ELM remain below this threshold and the interval between ELMs is higher than the heat diffusive time τ_χ of the tungsten armor and, consequently, the ELM frequency f_{ELM} much smaller than $1/\tau_\chi$. Here $\tau_\chi \sim \Delta^2/\chi$ and Δ is the tungsten armor thickness ($\sim 0.003\text{m}$ [1]) and χ is the tungsten thermal diffusivity ($\sim 3 \cdot 10^{-5} \text{m}^2/\text{sec}$ at 2000 K). The dependence of heat conductivity time on temperature for different tungsten armor thickness layer is shown on the Fig. 1. At 2000K τ_χ is about 0.3sec and the cumulative effect of ELM heating will take place if $f_{\text{ELM}} \ll 3\text{Hz}$.

Since $\Delta T \propto Q \Delta \tau^{-1/2}$, a melting threshold can be estimated at $Q \Delta \tau^{-1/2} \approx 45 \text{ MJm}^{-2} \text{ s}^{-1/2}$ where Q is the divertor ELM energy density in J/m^2 and $\Delta \tau$ is the time in seconds for that deposition. If a significant fraction of ELMs exceed this threshold then an unacceptable level of erosion may take place. Calculations that have been carried out for the ITER carbon divertor target indicate ablation will occur for ELM energy $\geq 0.5 \text{ MJ/m}^2$ if it is deposited in 0.1 ms, or 1.2 MJ/m^2 if the deposition time is 1.0 ms.

IV.2 The operating temperature windows for fusion reactor materials (not radiated by neutrons)

Several factors define the allowable operating temperature window for high temperature refractory W alloy, Cu alloys (CuOFHC) and reduced-activation ferritic /martensitic steel containing 8-12% of Cr (Eurofer) in a fusion reactor. The lower operating temperature limit in all alloys is mainly determined by radiation embrittlement (decrease in fracture toughness), which is generally most pronounced for irradiation temperatures below $\sim 0.3 T_m$, where T_m is the melting temperature. The upper operating temperature limit is determined by one of four factors, all of which become more pronounced with increasing exposure time:

- (1) thermal creep (grain boundary sliding or matrix diffusional creep);
- (2) high temperature He embrittlement of grain boundaries;
- (3) cavity swelling.(particularly important for Cu alloys, CuOFHC); or
- (4) coolant compatibility: corrosion issues.

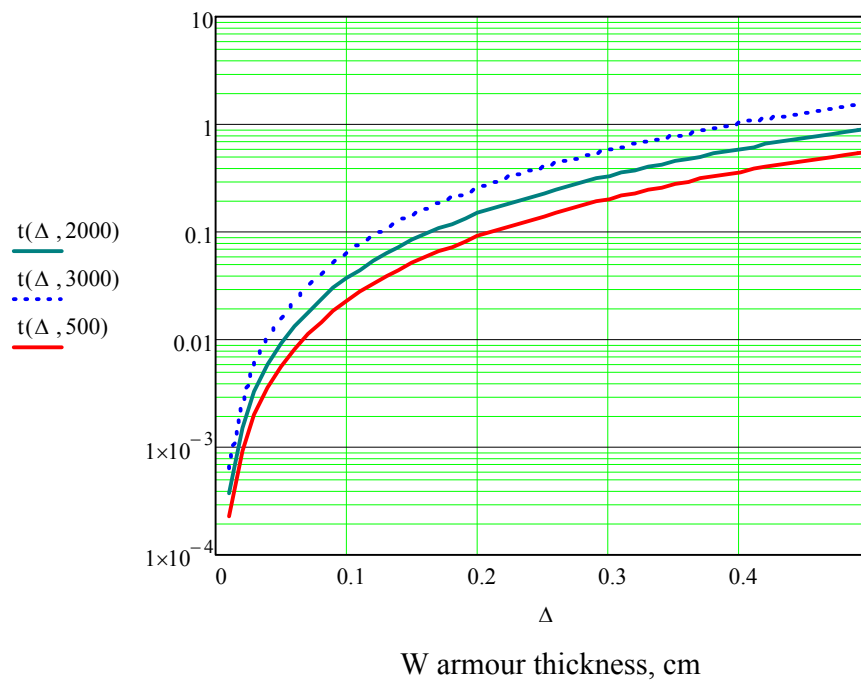


Fig. 1 Dependence of heat conductivity time on temperature for different thickness of tungsten armor.

In many cases, the upper temperature limit will be determined by coolant corrosion compatibility rather than by thermal creep or radiation effects.

IV.3 Range of the allowable temperatures

1. TUNGSTEN alloys [$773^{\circ}\text{K} \leq T \leq 1573^{\circ}\text{K}$], [$T_m \sim 2300^{\circ}\text{C}$, $0.3 \cdot T_m = 700^{\circ}\text{C} \sim 973^{\circ}\text{K}$]
2. EUROFER [$598^{\circ}\text{K} \leq T < 823^{\circ}\text{K}$]
3. Cu OFHC [$573^{\circ}\text{C} \leq T \leq 923^{\circ}\text{C}$]

The lower temperature of the divertor operating window is dictated by the ductile-brittle transition temperature and the upper temperature by the recrystallization temperature of WL10 material, assumed at 600°C and 1300°C , respectively, under irradiation.

Irradiation at 5 dpa causes thermal conductivity degradation in materials by the order of 20 % in CuOFHC and 10% in Eurofer and W-.

IV.4 Properties of un-irradiated TUNGSTEN

[$(773-1173)^{\circ}\text{K} \leq T \leq 1573^{\circ}\text{K}$] [$T_m = 3422^{\circ}\text{C} = 3695^{\circ}\text{K}$]

In this study it has been assumed that W temperature operating window is between $(500-1300)^{\circ}\text{C}$ or $(773-1573)^{\circ}\text{K}$

IV.5 Properties of irradiated TUNGSTEN

Irradiated W (up to 10dpa and higher [S.Zinkle et al., Fusion Engineering and Design, vol.86, p.1652, 2011]) [$(800-900)^{\circ}\text{C} \leq T \leq 900^{\circ}\text{C}$]

[$(773-1173)^{\circ}\text{K} \leq T \leq 1573^{\circ}\text{K}$]

800°C and 1300°C ,

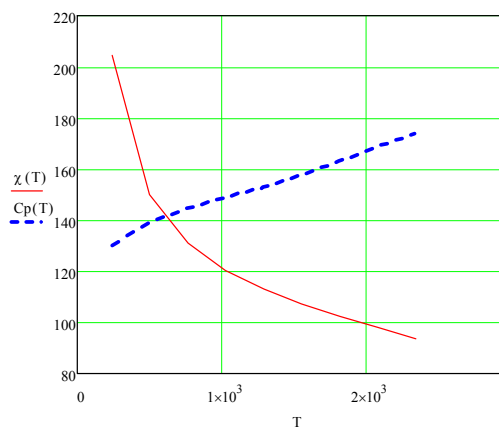
For W, of which the DBTT shifts due to neutron irradiation is unknown, the lower boundary of the operating temperature window is usually conservatively recommended as $0.3 \cdot T_m$ (K). That is the recovery stage of the annealing heat treatment process of bcc metals, at which some restoration of original properties (e.g. hardness, ductility, and resistivity) is achieved by the rearrangement of dislocations. For example, this corresponds to about 800°C for tungsten materials ($T_m = 3410^{\circ}\text{C}$), as also indicated in [3] as the estimated value. The limit temperature determined in this way is significantly higher than the assumed $DBTT_{irr}$ of 600°C for WL10. This makes the thimble apparently the most critical component, as a result of that inherent brittleness of tungsten materials.

IV.6 Characteristics of materials: W & diamond/copper composite DCC

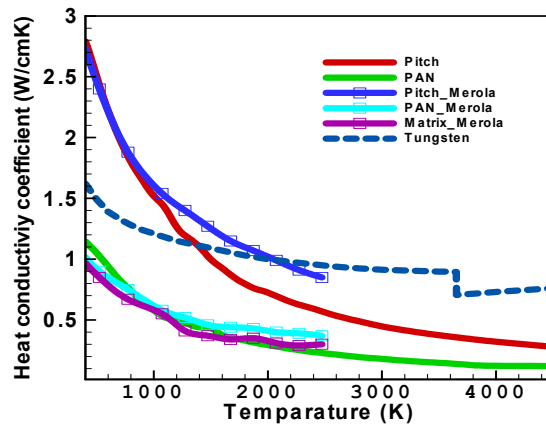
Tungsten thermal conductivity $\chi(T)$:

W / (m·°C), Density kg/m³

Temperature, C	unirradiated	irradiated	density
20	173	155.7	19300
100	165	148.5	19279
200	156	140.4	19253
300	147	132.3	19226
400	140	126	19198
500	133	119.7	19170
600	127	114.3	19141
700	122	109.8	19112
800	118	106.2	19112
900	114	102.6	19083
1000	110	99	19053
1200	105	94.5	19022
1400	102	91.8	18960
1500	101	90.9	18894
2000	99.1	89.19	18894
2500	98.7	88.83	18860



$$\chi(T) := 1.0834 \cdot 10^2 \cdot \left(1 - 0.971 \cdot 10^{-4} \cdot T + \frac{216.17}{T} \right), \text{ W/m K}$$

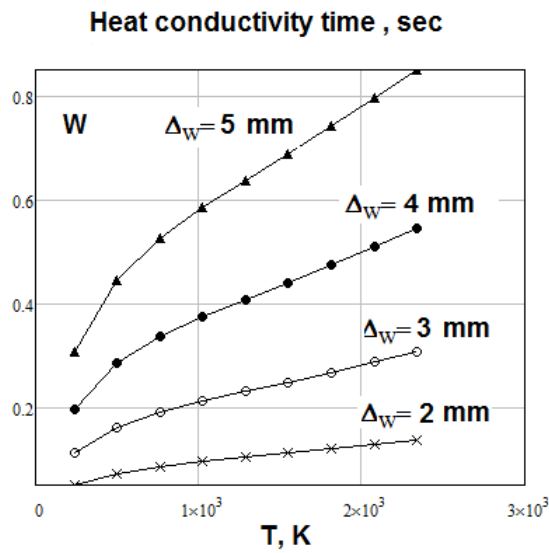


IV.7 Tungsten specific heat $C_p(T)$: J/kg K

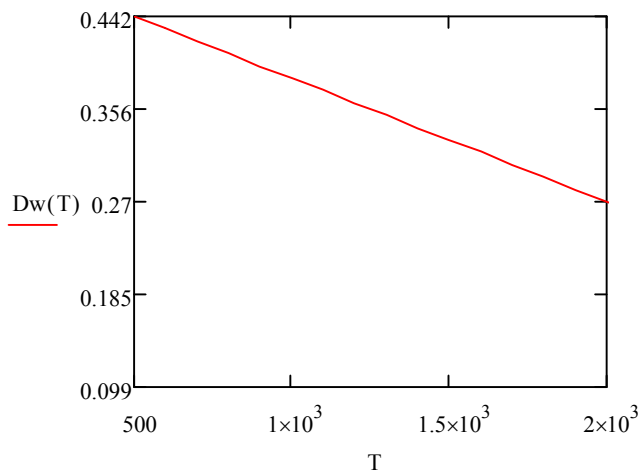
$$C_p(T) := 116.37 + 7.1119 \cdot 10^{-2} \cdot T - 6.5828 \cdot 10^{-5} \cdot T^2 + 3.2396 \cdot 10^{-8} \cdot T^3 - 5.4523 \cdot 10^{-12} \cdot T^4$$

Thermal conductivity time (sec) vs. temperature (K) for the different W thickness (cm)

$$t(a, T) := \frac{a^2}{\chi(T)} \cdot C_p(T) \cdot \rho(T)$$



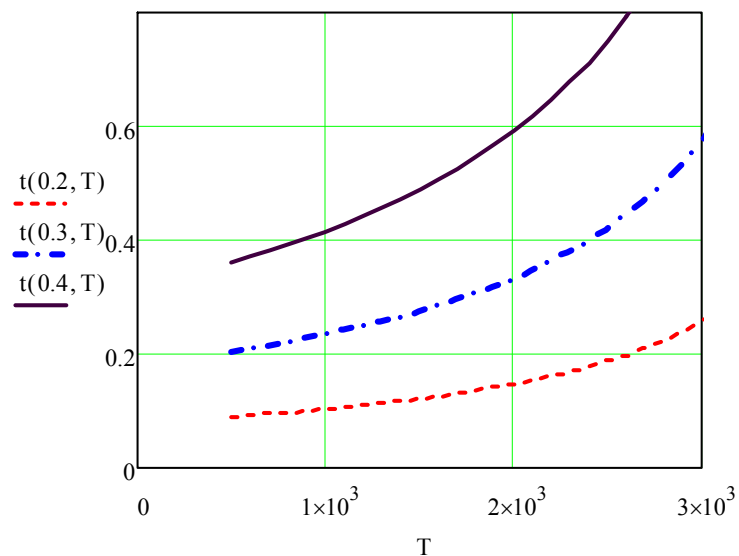
IV.8 Tungsten diffusivity Dw(T):



$$D_w(T) := 0.49886 - 0.0001142T + 1.23810^{-8} \text{ cm}^2/\text{s}$$

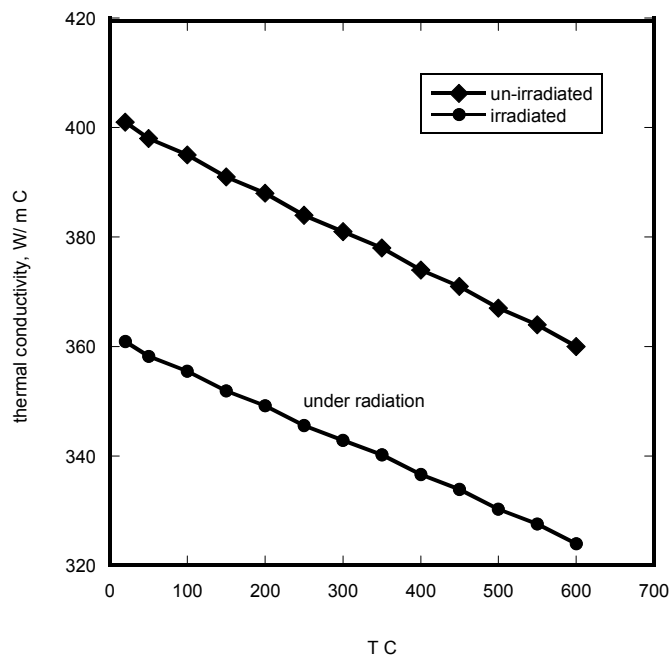
IV.9 Thermal diffusivity time (sec) vs. temperature (K) for different W thickness (cm)

$$t(\Delta, T) := \frac{\Delta^2}{D_w(T)}$$



IV.10 Oxygen-free high thermal conductivity (OFHC) copper CuOFHC/Cu-c1/C10200

Melting Point	1083 C
Density	8.94 gm/cm ³ @ 20 C
Specific Gravity	8.94
Electrical Resistivity	1.71 microhm-cm \cong 20 C
Electrical Conductivity	0.591 MegaSiemens/cm \cong 20 C
Thermal Conductivity	391.1 W/m ² K at 20 C
Coefficient of Thermal Expansion	16.9 •10 ⁻⁶ per °C (20-100 C)
Coefficient of Thermal Expansion	17.3 10 ⁻⁶ per °C (20-200 C)
Coefficient of Thermal Expansion	17.6 10 ⁻⁶ per °C (20-300 C)
Specific Heat Capacity	393.5 J/kg°C at 293 K
Modulus of Elasticity in Tension	117000 MPa
Modulus of Rigidity	44130 MPa



IV.11 Thermal conductivity of Cu OFHC , W/(m·°C)

Thermal conductivity, W/(m·°C)

Temperature, C	Un irradiated	irradiated	Density kg/m ³
20	401	360.9	8940
50	398	358.2	8926
100	395	355.5	8903
150	391	351.9	8879
200	388	349.2	8854
250	384	345.6	8829
300	381	342.9	8802
350	378	340.2	8774
400	374	336.6	8744
450	371	333.9	8713
500	367	330.3	8681
550	364	327.6	8647
600	360	324	8612

IV.12 Reinforced Diamond/Copper Composite (DCC)

Water pipes imbedded into tungsten mono-blocks (used as heat diffuser). Water is considered to be at higher operating temperatures up to 374°C and pressures < 22.1 MPa (like at PWR conditions) to keep the possible irradiation damage (embrittlement) on a tolerable level and the RCC pipes as a suitable structural material.

IV.13 Thermal properties of diamond/copper composite material DCC

An effective thermal conductivity of the DCC composite has been assessed in [K. Yoshida, H. Morigami / Microelectronics Reliability 44 (2004) 303–308]. The thermal conductivity is a function of the thermal conductivities of the diamond particles and the cuprum matrix and the volume fraction of each component and also of the diamond particle sizes. The thermal conductivities of composites is about 600 W/mK for 90-110µm diamond particle size and for ~65% of volume fraction of diamonds in the composite. We assume this value for our calculations. Notice, that the thermal conductivity of unirradiated diamond and copper are 1300 and 395 W/mK respectively.

Density: 5420 kg/m³, Specific heat: 439 J/kgK, Thermal conductivity: 600 W/mK

	TC unirrad./ irradiated	CTE unirrad./ irradiated[300-573]K	
DCC	600 W/mK / 540 W/mK	~8x10 ⁻⁶ /K	
Tungsten	/90% less		

IV.14 Water coolant parameters

Tube (EUROFER) temperature $T_c = T_{\text{water}} + q/h$, $h = (0.5-10) \text{ kW/m}^2\text{K}$

Water temperature $T_{\text{water}} \leq 325^\circ\text{C} = 598\text{K}$

Water pressure in inlet $\leq 15.5\text{Mpa}$

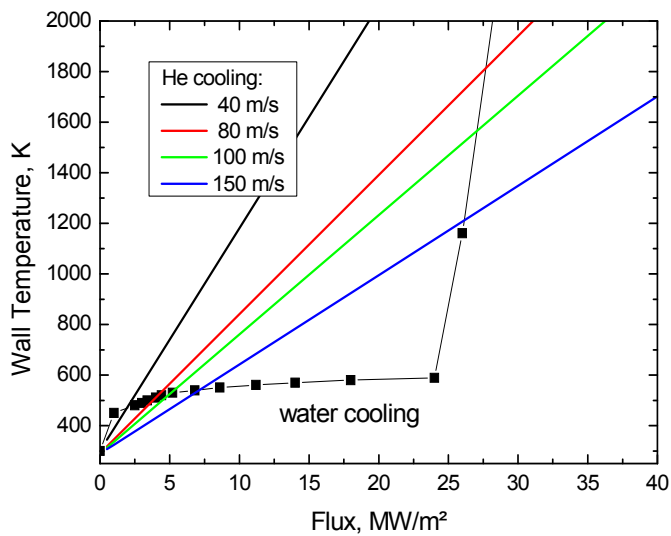
Water velocity 12m/sec

Water thermal conductivity: χ [W/m²K]

in the range $274 \text{ K} \leq T \leq 370\text{K}$

$$\chi = \chi_0 \{-1.48445 + 4,1229 (T/ T_0) - 1.63866 (T/ T_0)^2\}$$

$$\chi_0 = 0.6065 \text{ W/m}^2\text{K}, T_0 = 298.15 \text{ K}$$



IV.15 Parameters of discharges for disruption mitigation experiments in different tokamaks (S. Bozhenkov, Preprint, Juell-4288)

Tokamak	a_{pi}/R_0 , m/m	B_t , T	I_{pb} , MA	n_e , 10^{19} m^{-3}	L/D	P_{aux} , MW	E_{th}/E_{mag} , MJ/MJ	Type	N_i , 10^{21} atoms
T-10 [85]	0.39/1.5	2.5	0.08 – 0.2	2.5 – 4.5	L	0	??	P - KCl, Ti	0.005
TEXTOR present	0.46/1.75	2.25	0.35	2	L	0	0.05/0.3	MGP - D ₂ , He, Ar, Ar%	0.8 – 20
TORE SUPRA [91]	0.72/2.40	< 4.2	< 1.2	4	L	0	??	MGP - He	200
ASDEX-U [86]	0.5/1.6	< 3.9	0.6; 1	?	D	0; 9	(0.06; 0.5)/(0.6; 1.5)	P - Ne	0.17
ASDEX-U [92]	0.5/1.6	< 3.9	0.4 – 0.8; ?	?	L/D	?	(0.05 – 0.2)/?	MGP - He, Ne, Ar	0.7 – 3
DIID [87, 88]	0.6/1.7	1.8 – 2.1	1 – 1.5	?	D	?	~ 1/ ~ 2	P - Ne, Ar, Ne%	0.28 – 0.68
DIID [95, 96, 97, 98]	0.6/1.7	2.1	1.5	3; 8	D	5 – 7	(0.6 – 0.9)/1.6	MGP - D ₂ , He, Ne, Ar	40
ALCATOR C-Mod [99]	0.21/0.66	5.4	1	15 – 30	D	?	0.1/0.65	MGP - He, Ne, Ar, Kr	50 – 100
JT-60U [89]	1/3.4	2.2; 3.3	1.6 – 1.7	?	D	0; 12	(0.25; 1.8)/3.7	P - Ne	0.5 – 2.1*
JT-60U [101, 102]	1/3.4	3.5	0.85	1 – 1.5	D	?	~ 0.3/ ~ 0.93	SGP - H ₂ , Ar, Kr, Xe, %	0.2 – 10
JET [103]	1.25/2.96	3	2	?	D	?	??	SGP - He, Ne, Ar	< 9

Table 2.1: Parameters of discharges used for disruption mitigation experiments in different tokamaks. "L" - limiter, "D" - divertor, "P_{aux}" - auxiliary heating, mainly NBI. "E_{th}" - thermal energy content, "E_{mag}" - magnetic energy, "P" - pellet injection, "MGP" - massive gas puff by ferromagnetic or eddy currents valve, stated amount of particles is introduced in 1 – 10 ms, "SGP" - slow gas puff by standard fueling valves, the stated amount of atoms is introduced in 50 – 100 ms, "N" - number of injected atoms, "?" stands for unknown value. In TEXTOR case "Ar%" denotes the argon mixture experiments, while in JT-60U row "%" marks experiments with mixtures of hydrogen with one of Ar, Kr, Xe. It worth noting that the shown limit of injected particles in the gas puff experiments is imposed by requirements of the tokamak vacuum system, while for "killer" pellets it is limited by the achievable size of the pellet itself. * - achieved by train of three pellets.

